1987

Theoretical And Experimental Studies On The Instability Of Charged Liquid Drops

Hany Mohamed Elghazaly

Recommended Citation

Elghazaly, Hany Mohamed, "Theoretical And Experimental Studies On The Instability Of Charged Liquid Drops" (1987). *Digitized Theses*. 1641.
https://ir.lib.uwo.ca/digitizedtheses/1641

National Library
of Canada

Bibliothèque nationale
du Canada

Canadian Theses Service

Services des thèses canadiennes

Ottawa, Canada
K1A 0N4

CANADIAN THESES

THÈSES CANADIENNES

NOTICE

The quality of this microfiche is heavily dependent upon the quality of the original thesis submitted for microfilming. Every effort has been made to ensure the highest quality of reproduction possible.

If pages are missing, contact the university which granted the degree.

Some pages may have indistinct print especially if the original pages were typed with a poor typewriter ribbon or if the university sent us an inferior photocopy

Previously copyrighted materials (journal articles, published tests, etc.) are not filmed.

Reproduction in full or in part of this film is governed by the Canadian Copyright Act, R S.C. 1970, c C-30.

AVIS

La qualité de cette microfiche dépend grandement de la qualité de la thèse soumise au microfilmage Nous avons tout fait pour assurer une qualité supérieure de reproduction

S'il manque des pages, veuillez communiquer avec l'université qui a conféré le grade

La qualité d'impression de certaines pages peut laisser à désirer, surtout si les pages originales ont été dactylographiées à l'aide d'un ruban usé ou si l'université nous a fait parvenir une photocopie de qualité inférieure

Les documents qui font déjà l'objet d'un droit d'auteur (articles de revue, examens publiés, etc) ne sont pas microfilmés

La reproduction, même partielle, de ce microfilm est soumise à la Loi canadienne sur le droit d'auteur, SRC 1970, c C-30

THIS DISSERTATION
HAS BEEN MICROFILMED
EXACTLY AS RECEIVED

LA THÈSE A ÉTÉ
MICROFILMÉE TELLE QUE
NOUS L'AVONS REÇUE

NL-339 (r 86/06)

Canadä

THEORETICAL AND EXPERIMENTAL STUDIES ON THE INSTABILITY OF CHARGED LIQUID DROPS

by

Hany Mohamed Amin Elghazaly

Faculty of Engineering Science

Submitted in partial fulfillment
of the requirements for the degree of
Doctor of Philosophy

Faculty of Graduate Studies
The University of Western Ontario
London, Ontario
October, 1986

ISBN 0-315-36069-0

ABSTRACT

To be able to properly predict the breakup of highly charged liquid droplets, a complete understanding of their behaviour at the Rayleigh limit is necessary. An analytical model has been developed for a conductive spherical drop charged to its Rayleigh limit which predicts the final state just after the breakup for both single and multi-sibling disintegrations. The numerical analysis of this model involves scanning all the possible radii of the sibling droplets and ensuring that the solutions satisfy the conservation of energy and Rayleigh limit criteria. For a drop unaffected by any external force, the results of this model show that the most probable disintegration satisfies the single sibling breakup. The sibling, under such conditions, carries about 25% of the initial mass and 40% of the initial charge. The results also show that the difference between the final energy, calculated at different sibling mass ratios, and the minimum final energy is very small for a very wide range of sibling mass ratios (0.1 to 0.9) and thus can be easily affected by any external force to produce a multi-sibling disintegration. For the multi-sibling case, the model assumes tree-like secondary breakups which lead to a residual drop and n siblings of different sizes and charges. The role of the external forces on the breakup process and on the disintegration of

the liquid drop below its Rayleigh limit is also discussed. The results of this model show good agreement with the experimental observations of many other investigators. In addition the results clarify the demarcation between the modes of single and multi-sibling breakup. The numerical results also show that the single sibling exists for all the values of sibling mass ratios greater than 11.1%. For all the values less than this, the multi-sibling disintegration is favoured. This has been verified experimentally by collecting water droplets after their breakup on water sensitive paper and then examining their traces with a microscope.

Since the Rayleigh limit is only valid for spherical droplets unaffected by any external force, general equations describing the drop stability have been derived for both prolate and oblate spheroidal shapes. Various types of forces such as electrical, gravitational and aerodynamic forces were considered. From the analytical evaluation of these equations, it was concluded that the Rayleigh limit is only valid for small droplet sizes ($R < 50$ µm) and for very low levels of external forces. For certain combinations of external forces, the predicted stability limit may be higher than the Rayleigh limit.

An analytical study was performed to predict the maximum charge that a liquid drop can retain without losing its charge by electron avalanches or by redistributing the charge among smaller droplets through surface disruption. The liquid surface tension, air pressure, temperature and relative humidity were considered through their effects on corona onset field and the stability limit. The results of this analysis indicated that for water drops at NTP and standard humidity, the surface instability prevails and restricts the maximum charge limit. For lower air pressures, higher air temperature or high relative humidity, the possibility of electron avalanches is enhanced.

ACKNOWLEDGEMENTS

The author wishes to express his deep gratitude to Professor G.S. Peter Castle for his supervision and guidance which he generously offered throughout the course of this study.

The author also wishes to express his sincerest gratitude to Professor I.I. Inculet and Dr. W.D. Greason for their advice, encouragement and unfailing discussions throughout the period of preparation of this thesis.

The financial support from the Natural Sciences and Engineering Research Council of Canada is also gratefully acknowledged.

Finally, the author wishes to thank all the graduate students and the staff of the Applied Electrostatics Laboratory for their sincere cooperation.

TABLE OF CONTENTS

LIST OF TABLES

LIST OF PHOTOGRAPHIC PLATES

LIST OF FIGURES

NOMENCLATURE

a, b	The semi-major and the semi-minor axes of a spheroid respectively (m)
a_e	Equatorial radius of a spheroid (m)
A, B	Points at the end of the pole and the equator of a spheroid
A_o, B_o	Constants (Eq. 7.1)
b_i	Ion Mobility (m^2/V.s)
C_{11}, C_{22}	Coefficients of self capacitance for the residual and the sibling drops respectively (F)
C_{12}, C_{21}	Coefficients of induction for the residual and the sibling drops (F)
CA	Catenary parameter (m)
C_D	Drag coefficient
d	Spacing between the sibling and the residual drop at breakup (m)
d_{max}	The maximum stable equivalent drop diameter (m)
D	Drop deformation = a/b
D_f	Drag force (N)
D_s	Stokes drag on a rigid sphere (N)
e	Spheroid ellipticity
E	Electric field (V/m)
E_1	Electric field component in the direction of the onset field (V/m)
E_c	Corona onset field (V/m)
E_{cQ}	Electric field due to the electric charge at the spheroid tip (Eq. 7.5), (V/m)

E_i	Initial energy (J)
E_f	Final energy (J)
E_{max}	Maximum electric field (V/m)
F	External force (N)
g	Gravitational acceleration (m/s^2)
h	Hydrostatic head (m)
H	Air Humidity (g/m^3)
I_1	Mathematical factor (Eq. 4.6)
I_2	Mathematical factor (Eq. 5.13)
K	Mathematical factor (Eq. 5.18)
K_1	Dimensionless stagnation pressure
K_2	Dimensionless stagnation pressure at the drop equator
L	Deformation factor (Eq. 5.18)
$M(\alpha)$	Dimensionless mathematical factor (Eq. 4.6)
M_0	Initial drop mass (kg)
M_1	Residual drop mass (kg)
M_2	Sibling mass (kg)
n	Number of siblings
N	The perpendicular from the center of the spheroid to the tangent plane at any point on its surface
P	Air pressure (mm.Hg)
P_f	Permittivity factor (Eq. 1.3)
P_0	Dimensionless frontal stagnation pressure
P_{elec}	The normal electric stress (N/m^2)
P_{ext}	The contribution of the external forces on the drop pressure at the point under consideration (N/m^2)

P_h	The hydrostatic pressure (N/m^2)
P_s	The surface tension pressure (N/m^2)
P_∞	The ambient pressure (N/m^2)
Q_0	Initial charge (C)
Q_1, Q_2	Actual charges of the residual and the sibling drops respectively (C)
Q_{E1}, Q_{E2}	Effective charges of the residual and the sibling drops respectively (C)
Q'_{1n}, Q'_{2n}	Actual charges of the nth. group of the secondary residual and sibling drops respectively (C)
Q_c	Corona charge (C)
Q (cond.)	The maximum charge that a drop can carry due to the conduction or induction charging (C)
Q_d	Charge of a deformed drop (C)
Q (Pauth.)	The Pauthenier charge limit (C)
$Q_{R.L}$	Rayleigh limit charge (C)
$Q_{S.L}$	Stability limit charge (C)
R_0	Initial drop radius (m)
R_1	Residual drop radius (m)
R_2	Sibling drop radius (m)
R'_{1n}	The radius of the secondary residual droplet of the nth. group (m)
R'_{2n}	The radius of the secondary sibling droplet of the nth. group (m)
Re	Reynolds number
R_{c1} and R_{c2}	The principal radii of surface curvature (m).
S	Deformation factor (Eq. 5.13)

t	time (s)
T_p	Pauthenier time constant (s)
T	Air temperature (°C)
U	Deformation factor (Eq. 5.18)
V	Electrical potential of the droplets (volt)
Ve	Drop velocity (m/s)
V_T	Terminal velocity (m/s)
W	Deformation factor for an oblate spheroid
We	Weber number (Eq. 4.9)
X_1, X_2	Variables in the catenary equations (m)
y	Numerical parameter ≤ 1
Z	Ohnesorge number (Eq. 4.11)
α	Deformation factor for a prolate spheroid
$\Delta\rho$	The absolute value of a two fluid density difference (kg/m^3)
δ	Air density factor
ϵ_o	Permittivity of free space (F/m)
ϵ_c	Critical permittivity (F/m)
ϵ_r	Relative Permittivity
λ	Disturbance wave length (m)
λ_c	Critical disturbance wave length (m)
μ	Viscosity of a fluid (kg/m.s)
μ_a	Air viscosity (kg/m.s)
μ_{ex}	Viscosity of the exterior fluid (kg/m.s)
μ_i	Viscosity of the interior fluid (kg/m.s)
μ_ℓ	Liquid viscosity (kg/m.s)

γ	Liquid surface tension (N/m)
γ_{eff}	Effective surface tension (N/m)
ρ	Drop density (kg/m^3)
ρ_i	Ion density (kg/m^3)
ρ_a	Air density (kg/m^3)
ρ_ℓ	Liquid density (kg/m^3)
σ	Surface charge density (C/m^2)

CHAPTER ONE

INTRODUCTION

1.1 Applications of Charged Liquid-Drops

Charged liquid drops in the form of aerosols or sprays are of importance in a considerable number of applications such as paint and agricultural pesticide spraying, ink jet printing, electrostatic dispersal of liquids and air cleaners. In paint and crop spraying, droplets are deliberately charged because they may be guided by electrostatic fields and because they are attracted to conducting surfaces by virtue of their image.

Individual droplets or streams of droplets are used for ink jet printing. These droplets are charged and then deflected by an electric field to an appropriate point on the paper. In order to obtain maximum deflection, the charge should be as high as possible, but it cannot be so high that gaseous discharge or drop disruption occurs, since any of these would decrease the original charge and change the drop trajectory from its desired value. Liquids may also be dispersed by electrostatic forces to form a spray having a narrow size distribution centered upon a desired mean value. When dispersal is solely by electrostatic forces, the process invariably depends upon the liquid being deformed into one or more liquid jets which then break up into droplets.

In some types of air cleaners, charged droplets, normally water, are used to attract the opposite charged dust to the water droplets thus enhancing the settling rate of the fume and clearing the air. In addition to the previous applications, many recent studies have been carried out using charged liquid droplets in electric propulsion of space vehicles, administration of certain drugs in medicine, and as an ionic space charge generator for particle charging. They are also of central importance to cloud physics and to the understanding of atmospheric effects in general.

1.2 Drop Instability

A number of causes for breakup of liquid drops have been identified and studied. These include rapid accelerations, turbulent fluctuations and strong electric fields or pressures. Even when none of these disturbances are present, there is a limit to the size at which drops can be produced due to the existence of the gravitational field.

In 1882 Lord Rayleigh [1] showed that an electrically charged spherical liquid drop, unaffected by any external force, becomes unstable when the outward electrostatic pressure of repulsion exerted by the charges exceeds the surface tension pressure. He derived the instability condition for an electrically charged liquid drop of radius (R) and surface tension (ν) in air of permittivity (ε_0) as:

$$Q_{R.L} = 8\pi(\nu\varepsilon_0 R^3)^{1/2} \qquad 1.1$$

where $Q_{R.L}$ is the maximum charge that can reside on the surface of a liquid drop. For charge higher than $Q_{R.L}$, disruption into smaller droplets occurs. Therefore, the limiting charge to mass ratio of a drop due to the Rayleigh instability is found to be:

$$\frac{Q_{R.L}}{M} = \left(\frac{36\varepsilon_0\nu}{\rho_l^2 R^3}\right)^{1/2} \qquad 1.2$$

The validity of this relationship is supported by a large number of charge to mass ratio measurements by Hendricks [2]. In his study, almost no droplets of higher charge to mass ratio than that predicted by Equation 1.2 were detected (i.e. ≈ .3%). More recent work by Schweizer and Hanson [3] on a single charged droplet (15 -40 μm. diameter) balanced against gravity by a combination of electric fields showed that droplet disruption occurred at the theoretical Rayleigh limit within a standard deviation of ±4%. In order to substitute the old notation and to fill the omitted steps in Lord Rayleigh's original reference, Hendricks and Schneider [4] introduced a complete derivation of the Rayleigh instability theory.

It is important to note here that experiments attempting to define the end state of a drop after its breakup have yielded conflicting results regarding the charge to mass ratios and the number of emitted droplets (siblings) [3,5-6]. Despite the obvious importance of charged drop disruption in the electrostatic applications and in the atmospheric physics, very little work on modelling the general features of the process has been reported in the literature.

For relatively large droplets (R>100 um.), Rayleigh's assumption of sphericity may not be valid. More accurate values for their charge limits are required. The assumption of no external force affecting the drop instability also seems unrealistic. In the normal condition, the gravitational force, the aerodynamic forces on the moving drop and the external electric force exerted by the space charge and other electrified objects may not be neglected and a modification of the Rayleigh limit may then be required.

1.3 Evaporation of a Charged Liquid Drop

Total droplet charge is usually assumed to be constant and evaporation is assumed to follow the well established theory pertaining to uncharged droplets [7]. Robertson [8] reported that, in his experiments, the evaporation rate decreased by less than 7% for highly charged water drops as evaporating droplets approached the Rayleigh limit.

Abbas and Latham [5] showed experimentally that the evaporation of charged droplets of water, aniline and toluene was accompanied by no discernible loss of charge and a consequent increase in electrical pressure in the drop surface owing to the decrease in radius. When the relationship between the drop charge (Q) and the radius (R) became almost consistent with the Rayleigh criterion, they illustrated that the drop disintegrated to eject about 25% of its mass in the form of highly charged droplets carrying about 30% of the initial charge.

One must conclude that the above process occurs repeatedly, i.e. the evaporating drop reaches Rayleigh instability and splits into smaller droplets, etc. This breakup which is a consequence of the evaporation of charged droplets has to be accounted for when working with highly charged drops.

1.4 Charging Processes

The methods by which particles or liquid droplets can be charged for particular applications have been reviewed by Castle [9]. The traditional methods of droplet charging include the corona discharge as well as conduction and induction charging. In the corona discharge, the droplets are normally charged by unipolar ions. The maximum possible charge on a drop using this method is predicted by the well known Pauthenier relationship [10]. His formula can be written in the form:

$$Q(\mathrm{Pauth.}) = 4\pi\varepsilon_0 P_f R^2 E \qquad 1.3$$

and

$$P_f = \frac{3\varepsilon_r}{\varepsilon_r + 2}$$

where E is the external electric field, R is the drop radius and ε_r is the relative permittivity of the drop.

The actual charge on a drop is also a function of the exposure time to corona. For a limited exposure time (t), the charge is given as:

$$Q(t) = Q(\mathrm{Pauth.}) \frac{t}{t + T_p} \qquad 1.4$$

and

$$T_p = \frac{4\,\varepsilon_0}{\rho_i \; b_i}$$

where ρ_i is the ion density and b_i is the ion mobility.

For conductive liquids, the permittivity factor (P_f) is 3 while the electric field strength is limited by the breakdown strength of air. In the non-uniform field of a corona this field is usually taken as an average of 5 kV/cm [9]. For highly insulating liquids, the Pauthenier relationship does not always apply. This is because the surface charges cannot redistribute themselves around the surface in a short period of time. For the case of a conductive liquid, the corona discharge seems to be a simple and very effective charging process. However, its charging efficiency is very low since only a small percentage of the ions generated in the corona region are usually used in the charging process.

The principle involved in both conduction and induction charging is similar. In both processes, charges are produced on the surface of a conducting liquid drop due to its contact with an equipotential conductor. When the electrical contact is broken, the liberated drop will carry a net surface charge. For these charging methods, the liquid is usually considered conductive if its relaxation time is much less than the contact time with the equipotential conductor [11]. Experimental studies have shown that for most water based liquids, this condition is effectively satisfied [9]. For a more complete explanation of both conduction and induction charging, refer to [11].

In conduction charging, a power supply capable of supplying the charging potential and in turn the total charge is required. This often leads to practical difficulties with insulation and dangerous situations for the operator. This problem can be overcome by the use of induction charging. The power supply in such a process is used only to raise the potential of an electrode which induces opposite charges on the liquid surface. In this process, the work required to supply the electrical charges is due to the mechanical energy used to atomize the liquid. The main limitation in induction charging comes from the fact that the charged drops are normally attracted to the inducing electrode.

The theoretical maximum charge that can be placed on a drop, for either conduction or induction charging, under idealized conditions and assuming that the field is uniform at the breakdown strength of air (30 kV/cm.) is directly proportional to the product of the electric field strength and the surface area of the drop. This formula can be reduced to [11]:

$$Q\ (\text{cond.}) = 3.3 \times 10^{-4} R^2 \qquad 1.5$$

However, in practice, this maximum charge can vary significantly due to the relativly high non-uniform electric field around the drop or due to the effect of the space charge produced by the previously liberated droplets.

1.5 General Objectives

Considering the points raised in Section 1.2, the present work was undertaken to conduct a theoretical and experimental study to investigate the instability of charged liquid drops. There were four main objectives of this study:

1- to predict the end state of a disrupted drop on the basis of the conditions of the initial drop just before the breakup, i.e. to predict the number of siblings, the sibling mass ratio and the charge distribution among the residual drop and the siblings.

2- to determine the demarcation between the modes of single sibling and the multi-sibling breakup,

3- to investigate the effect of external forces on the Rayleigh instability and modify the Rayleigh limit equation (Equation 1.1) to take into account such effects,

4- to examine the maximum charge limit of the drop and predict whether the Rayleigh instability or gaseous discharge is responsible for that limit under different practical and industrial conditions.

Following these main objectives, this thesis is divided into three parts. The first, consisting of Chapters 2 and 3, deals theoretically and experimentally with modelling the breakup phenomenon for both the single sibling and the multi-sibling cases. In the second part, Chapters 4 to 6, a modified equation for the stability limit of liquid drops subjected to external forces is derived followed by a numerical analysis of the effect of these forces. The third part presented in Chapter 7, deals with an examination of the maximum charge limit of the drop. It also predicts analytically whether the Rayleigh instability or gaseous discharge is responsible for that limit and compares this prediction with some previously published data.

In Chapter 2, a review of the major theoretical and experimental studies of the breakup phenomenon is presented. Following this review, a numerical model was developed to simulate the breakup phenomenon. A numerical technique, based on scanning all the possible radii of the sibling droplets is introduced to predict the final state for a given drop charged to its Rayleigh limit with known surface tension and initial size. For a single sibling disintegration, the solutions have been required to satisfy the conservation of energy as well as the Rayleigh limit criteria for both the residual drop and the sibling. A further condition of minimum final energy was also examined.

This case was then extended to model the multi-sibling instability on the basis of tree-like secondary breakups which leads to a residual drop and n siblings of different sizes and charges. This extended model also predicts the role of the external forces on the breakup process.

In Chapter 3, the validity of the analytical models of the single sibling and the multi-sibling breakups described in Chapter 2 is examined experimentally. Charged droplets of water were formed at the tip of a capillary tube raised to high potential and subjected to external electric fields. The nozzle characteristics were tested to identify the different ejection modes. Under some conditions of electric field at the nozzle tip, breakup of the ejected droplets resulted. These droplets were collected on water sensitive paper and then examined under a microscope. Counting the number of siblings and measuring their mass provided data which was necessary to evaluate the analytical models and as a result verify the validity of the concept of tree-like secondary breakups, introduced in the multi-sibling model.

In the second part starting with Chapter 4, the most common forces acting on a drop and their effects on the drop instability are discussed through a literature review. An analytical equation is then derived, in Chapter 5, to modify the Rayleigh limit equation to take into account the effect of the external forces and the drop deformation on the stability limit. This equation is numerically evaluated for some preset external forces and the results are described and compared with the Rayleigh instability limit in Chapter 6.

The third part of this thesis considers the gas breakdown (corona discharge or a series of avalanches around a charged drop due to the high electric field in this region) as another phenomenon competing with the Rayleigh instability to release the drop charge. A numerical study, reported in Chapter 7, was conducted to establish the thresholds separating these two phenomena for different drop radii, liquid surface tension, air pressure, temperature and humidity.

Throughout this study, particular consideration was given to comparing the results with those introduced by many previous investigators. Due to the diversity of the three different parts of this study and for the convenience of the reader, the literature review is presented and discussed separately in each part of the thesis. An overview of the literature review can be summarized as follows. For the first part, a review of the drop disruption is discussed in Section 2.1. It presents some of the previous theoretical and experimental studies on the breakup of both single sibling and multi-sibling cases. In the second part, previously published work on the effect of the external forces on the drop instability is reviewed in Chapter 4. For part three, the literature review for different charge loss mechanisms as well as corona from liquid drops is presented and discussed in Sections 7.2 and 7.3.

CHAPTER TWO

ANALYSIS OF THE DISINTEGRATION OF CONDUCTING CHARGED LIQUID DROPS

2.1 Previous Work on Drop Disruption

It is well known that if a drop is charged and then left to evaporate, the charge density on its surface increases as evaporation proceeds. The surface charge density eventually reaches a limit at which the electrical force of repulsion, tending to break the drop apart, exceeds the surface tension force which holds the drop together. The drop then emits one or more highly charged droplets and thereby loses both mass and charge. The resultant residual drop and siblings are no longer at their stability limit. As evaporation proceeds, this process continues.

This phenomenon was observed experimentally by Doyle, Moffett and Vonnegut [6]. They suspended charged drops of either aniline or water with a diameter of 60 to 200 µm in a uniform electric field. The drop was left to evaporate until it became unstable. They noted that as the drop decreased in size, the electrical charge density on its surface increased until finally one or more small highly charged droplets were ejected and the initial drop lost about 30% of its charge. The number and size of these droplets were not measured but were estimated to be from one to ten in number and less than 15 µm. in diameter. The residual drop was then collected on a piece of filter paper and its diameter was determined from the size of the spot produced. Because the ejected droplets were much smaller than the original drop size, they considered the size of the initial drop to be equal to the residual drop thus neglecting the reduction in the initial drop size by disintegration.

Abbas and Latham [5] carried out an experimental and theoretical study on water and aniline drops of 30 to 200 µm. radii. The charge and the radius of a suspended drop were recorded at frequent intervals by alternately recording the magnitude of the field required to maintain the drop at a constant horizontal level and the time taken for the drop to fall in a weaker field of known strength between two horizontal lines with a vertical separation of 6 cm. This method was also used to estimate the sibling charge just after the breakup. Their observations indicated that at about the Rayleigh limit, the drop disintegrated. Although the size and number of siblings were not examined, their curves illustrated that their disintegrations were accompanied by a loss of about 25% of the initial drop mass and 30% of its charge. They also attempted to model the disruption process by assuming that a minimum amount of energy was removed during the disintegration so that the residual droplet was left at the Rayleigh limit. However, their experimental results indicated that the evaporation process was proceeding between two consecutive disruptions.

In a different experimental technique, Schweizer and Hanson [3] suspended 15 to 40 um diameter drops of n-octanol in a balancing d.c. field. An additional a.c. electrode was utilized to capture and centre the charged droplets, and to provide a parameter, the "spring point voltage", which allowed calculation of the charge and the mass of a captured drop. Their results showed that the initial drop lost about 23% of its original charge and approximately 5% of its mass at breakup.

It is believed that the effect of the a.c. field, in vibrating the drop and hence forcing it to disintegrate, led to these results which are not in agreement with other experimental data [5,6]. This belief is supported by the theoretical and experimental results of the effect of external electric field on the disintegration of charged [12,13] and uncharged [14,15] liquid drops. Since there is no reason to believe that the sibling would be more highly charged than the Rayleigh limit, analysis of their data gives an indication that at least two siblings must have been emitted.

In another theoretical and experimental study, Ryce and Wyman [16] adopted an energy minimization approach. In their mathematical model, the electrical interaction between the residual drop and the sibling is neglected. They assumed that the drop might be unstable below the Rayleigh instability condition due to drop deformation or charge polarization. They modified the Rayleigh limit to be:

$$Q_{R.L} = 8\pi\ y(\gamma \varepsilon_0 R_0^3)^{\frac{1}{2}} \qquad 2.1$$

where y is a numerical parameter ≤ 1. They also assumed that the original drop was divided into two drops of radii R and xR where $x \leq 1$. For y equal to one, the second derivative of the final energy equation with respect to x gives zero (point of inflection) at x equals I, i.e. symmetric breakup. However, they only relied on the first derivative and concluded that symmetrical splitting would occur at the Rayleigh limit. Asymmetrical splitting was then concluded to be favoured for all lesser charges. Results of the photographic observations of the division of charged water drops in paraffin oil were introduced. These demonstrated a characteristic saddle shape in the single sibling division as well as the asymmetrical splitting to two droplets.

In the last two decades, the multi-sibling disintegration has been investigated as a separate phenomenon for the breakup process. Ryce and Patriarch [17] in their energy minimization model considered the symmetric dispersion of the drop into n identical droplets of equal radius as well as the asymmetric division into two drops of different radii. They followed Ryce and Wyman [16] in assuming that a drop might be unstable below the Rayleigh limit because of the charge polarization (Equation 2.1). They concluded that below $y = 0.65$, the binary asymmetric division is favoured over the symmetric mode of disruption. According to their model, at $y = 1$, the formation of four symmetrical droplets led to a minimum energy, while the maximum number of allowed droplets to maintain the conservation of energy was 20. It is believed that their assumptions of n identical droplets and of negligible electrical interaction between these droplets are the reasons for not preserving the conservation of energy above 20 droplets. In their experimental study, the results showed only binary asymmetric division. They showed with photographic evidence that the smaller droplet (sibling) might be unstable and divide again if its radius was less than one half of the other drop radius (residual). By simple calculation of the sibling mass ratio (M_s/M_0) of the divided drops, one can see that it is $\leq 11.1\%$.

Pfeifer and Hendricks [18] calculated the minimum specific charge limit of an individual droplet after the disruption by following the same energy minimization approach. However, their assumption of symmetric dispersion of the drop to n identical droplets was far from the experimental data, indicating asymmetric division, reported by Doyle et al [6], Schweizer et al [3] and by Ryce et al [17].

Roth and Kelly [19] in more recent work modelled the multi-sibling disintegration on the basis of a system energy balance. Their results showed that a limited number of siblings, about seven, could be produced. In their model, the effect of the external forces on the charged droplet disruption was not discussed. The following assumptions were also made:

1- The single sibling was not considered as a probable splitting case.

2- The model neglected the energy losses by assuming the total energy before the breakup was equal to that just after the disintegration.

3- All the siblings were assumed to be identical and to be emitted simultaneously in geometrically regular patterns.

4- The effect of the image charges of both the residual drop and the siblings was neglected.

5- The original charge was assumed to be distributed among the siblings and the residual drop so that the average surface charge density was constant.

2.2 Single Sibling Disruption Model

In this part of the study, a mathematical model has been developed to predict the final state just after the breakup for a single sibling disintegration. This model is based on examining the final energy equation and performing a numerical search for all the values of the sibling mass ratios satisfying a single sibling breakup. In this model it is assumed that

1- The initial drop is conductive so that the droplets just before the breakup are at the same electrical potential.

2- The final state consists of a residual droplet and a single sibling modeled as two spherical drops separated by a distance (d).

The assumption of conducting liquid is necessary for the purpose of comparison with the previous experimental data which employed liquids such as n-octanol, water and aniline. High volume conductivity usually implies a high surface charge mobility. However, liquid surfaces often become contaminated with foreign atoms and adsorbed gases or both which usually result in even higher surface conductivity. In this study, the assumption of conductive liquid implies that both volume and surface conductivities are high enough so that during the breakup, the charge redistributes itself over the newly created surface in a time much shorter than the time required for the drop disruption. This assumption is justified on the basis of experimental studies which have shown that in most water based liquids, effective induction and conduction charging can be accomplished. This implies that the ion mobility is sufficiently high to allow charge redistribution on a time scale less than that required to mechanically form droplets.

Clearly, with some liquids, the time of disruption may be much shorter than the time required for the charge to redistribute itself over the newly created surface. In such a case, the two droplets will carry charges proportional to the original surface transmitted to each of the two droplets. This condition represents the case of the charge distribution introduced by Roth and Kelly [19] i.e. the average surface charge density is constant. However, in different attempts to modify this model to take into account the energy conversion and losses during the breakup, the results predicted a total energy after the breakup higher than the initial energy. Details of this analysis can be seen in Appendix I.

In the present study, following the assumption of conductive liquid, an infinite set of image charges is utilized to account for the influence of each of the droplets on the other and to simulate the equipotential surfaces. In this model no constraints have been applied on the energy equation. However, the conservation of energy is used only to check the validity of the solution.

2.2.1 Analysis

The initial drop (denoted by subscript 0) is considered to be at the Rayleigh limit. The charge and the initial energy of the system at a certain initial drop radius (R_0) are fully specified for a certain liquid with surface tension (ν).

$$\text{Initial energy } (E_i) = 4\pi\nu R_0^2 + \frac{Q_0^2}{8\pi\epsilon_0 R_0} \qquad 2.2$$

where Q_0 is the charge on the drop just before the disintegration as calculated using Equation 1.1.

The initial drop is then assumed to disintegrate to a sibling and a residual drop of radii R_2 and R_1 respectively. Ignoring any mass loss by evaporation and any charge loss by Townsend electron avalanches in the high non-linear field surrounding the droplets [8] during the disruption, then;

$$R_0^3 = R_1^3 + R_2^3 \qquad 2.3$$

and

$$Q_0 = Q_1 + Q_2 \qquad 2.4$$

The distance (d) between the sibling and the residual drop can be calculated by assuming that the sibling is joined to the residual drop by a catenary surface which approximates the interconnecting saddle shapes that are observed during the droplet development process [16,20].

Roth and Kelly [19] have chosen the catenary cross section of the form [CA cosh (X/CA)] to minimize the surface area of the interconnecting structure. The catenary parameter (CA) has been chosen to maximize the distance (d) when the surface reaches zero thickness at its minimum. The catenary assumption yields to;

$$d = CA \sinh(X_1/CA)\,[\cosh(X_1/CA)-1] + X_1 + CA \sinh(X_2/CA)\,[\cosh(X_2/CA)-1] + X_2 \qquad 2.5$$

where

$$X_k = CA \cosh^{-1}\left[\frac{1 + (1 + 4R_k/CA)^{1/2}}{2}\right], \quad k=1,2$$

and the maximum distance at the breakup occurs when $CA = R_2$.

Figure 2.1 illustrates the assumed disruption process. Following the assumption of conductive liquid and assuming instantaneous redistribution of charge during division, then the initial charge will redistribute itself on the new surface so that areas with smaller radius of curvature carry more charge. The two droplets will in turn be at the same potential just before the breakup. This common potential is lower than the potential of the initial drop. As soon as the breakup occurs, the mutual effects of the electric field of the two droplets will change the potentials of the residual drop and of the sibling by different amounts. This effect can be expressed by the use of a mutual capacitance between the two droplets.

As the distance between the two droplets increases, the effect of each of the two droplets on the other becomes smaller and in turn the mutual capacitance decreases. (At the same time, the potentials of the residual drop and the sibling decrease). This reduction in the mutual capacitance results in a decrease of the stored potential energy of the

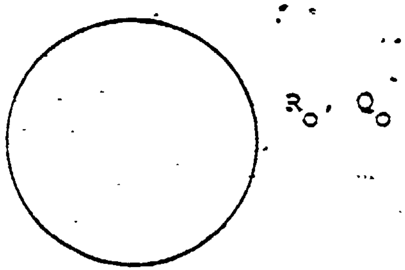

(a) Initial drop

(b) During disruption

(c) Final system

Figure 2.1 The Disruption Process

system. This component of the potential energy is thus converted into the kinetic energy that results from the repulsion forces between the two droplets moving apart.

To identify [illegible] problem at hand, one can see that although we have two equations from the conservation of charge and the conservation of mass, there are three unknowns for this system just after the breakup. These unknowns are namely the values of the charge of both the residual drop and the sibling and the initial common potential of the droplets at the breakup. Before attempting a numerical solution of the problem, the upper and the lower boundaries of the solution for the sibling charge were determined as follows. The potentials of both the residual drop and the sibling are assumed to be equal.

Following this assumption, the upper boundary for the sibling charge represents the case at which the distance separating the two droplets is very large. The residual drop charge and the sibling charge have been designated as Q_1 and Q_2 respectively. Hereafter, these values will be referred to as actual charges. Under such conditions, the potential (V) can be calculated as a function of the drop charge and its radius, i.e.

$$V = \frac{Q_1}{4\pi\varepsilon_o R_1} = \frac{Q_2}{4\pi\varepsilon_o R_2} \qquad 2.6$$

It is important to clarify here that this potential (V) is physically less than the value of the initial potential of the droplets at the breakup. Russell [21] showed that this upper boundary of the sibling charge (calculated with Eq. 2.6) gives an error between 11 and 23% in the range of droplets sizes and the distance (d) used in the present study.

The lower boundary of the sibling charge can be estimated (using the lower value of the potential V) when the distance separating the two droplets is calculated from the catenary assumption (Eq. 2.5). In this process both the self and mutual capacitances of the drops are considered through the image charges to account for the interaction effect of the droplets. However, the effect of the electric field from each of the droplets in distorting the spherical shape of the other and in changing its stability limit is neglected. This leads to Q_{E1} (the effective residual drop charge) and Q_{E2} (the effective sibling drop charge) which can be expressed in the form [21]

$$\begin{aligned} Q_{E1} &= (C_{11} + C_{21})\, V \\ Q_{E2} &= (C_{12} + C_{22})\, V \qquad 2.7 \end{aligned}$$

where C_{rr} is the coefficient of self capacitance and is defined as the charge to potential ratio on the r^{th} conductor when the other conductors are present but earthed.

The negative coefficient C_{sr} is the coefficient of induction and is defined as the ratio of the induced charge (by the principle of induction charging) on the r^{th} conductor to the potential of s^{th} conductor when all conductors except the s^{th} are grounded. The coefficients C_{11}, C_{12}, C_{21} and C_{22} are calculated as a function of the sibling and the residual drop radii, and the distance (d) [21,22].

Since the potential (V) is less than the real potential of the droplets at the breakup, which is unknown, and since the coefficient C_{12} is negative, the sibling effective charge Q_{E2} is in fact less than the real physical charge. The error in using the lower boundary of the sibling charge at the minimum energy condition (as will be seen in the following sections) is about 5%. Also as will be seen in the results of this model, the sibling charge is the principal element which controls the breakup behaviour. Because the lower boundary is closer to the real value than the upper boundary, it was decided to use this effective value in the iteration calculations of this study.

The final energy E_f (the total potential energy of the system at the breakup) can then be calculated from;

$$E_f = 4\pi\nu(R_1^2 + R_2^2) + V^2 (C_{11} + 2|C_{12}| + C_{22})/2 \qquad 2.8$$

where the first term is the surface tension energy while the second term is the electrical potential energy stored in the system at the breakup. It is important to note here that the difference between this electrical potential energy and the final potential electrical potential energy $(1/2\ VQ_0)$ represents the part of the potential energy which converts to kinetic energy as the distance between the two droplets increases. The difference between the initial energy (E_1) and the total potential energy at the breakup (E_f) represents the energy used during the breakup. This difference is believed to be converted to both kinetic energy of the droplets during the breakup and energy dissipation by a combination of viscous resistance to the drop motion and acoustic wave generation. This means that at the time of the breakup, the two droplets will have a certain kinetic energy so that

$$K.E. = 1/2\ [\ M_1\ Ve_1^2 + M_2\ Ve_2^2\ ] \qquad 2.9$$

Assuming the initial drop at rest, the momentum of the droplets when added together at any time must also be zero. Then from the momentum balance equation;

$$M_1 Ve_1 = - M_2 Ve_2 \qquad 2.10$$

From the previous discussion, one can see that at the breakup, the residual drop and the sibling will be moving apart with velocities Ve_1 and Ve_2 respectively. The values of these velocities at the breakup can be calculated if the kinetic energy of the droplets at the breakup is known.

It is obvious that R_1 and R_2 are less than R_0. Then by picking a value for R_2 (sibling radius) both the sibling and the residual radii and charges, and the final energy of the system can be calculated. A numerical technique is adapted to calculate the final state of the system for a predetermined initial drop radius (R_0) and surface tension (γ). In this process, the sibling radius is then chosen and changed in steps of 1/1000 of the initial radius to scan all the possibilities of the radii of the sibling. Figure 2.2 shows the flow chart of the calculations.

The results at each value of R_2 are then examined to satisfy the following two conditions:

1- To ensure the conservation of energy, the total potential energy at the breakup must be less than the initial energy. This condition accounts for the kinetic energy associated with the disruption plus any

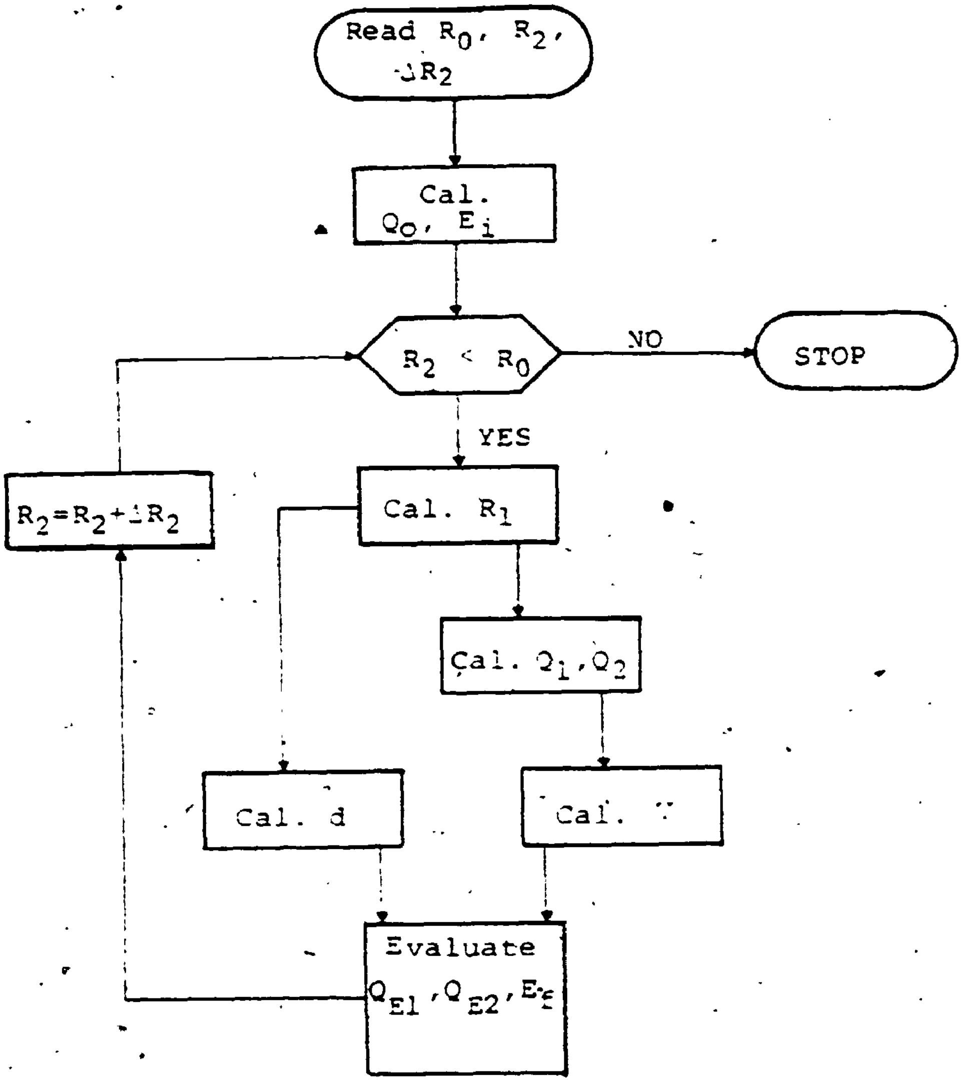

Figure 2.2 Flow Chart of the Program

energy losses.

2- Both the sibling and the residual charges must be less than their Rayleigh charge limit. This condition is necessary to insure a stable solution.

It is clear that the previous mathematical model consists of 5 unknowns ($R_1, R_2, Q_{E1}, Q_{E2}, E_f$) and 4 equations. Therefore, the condition of Rayleigh limit stability of the droplets (condition 2) is used to identify the range of solutions satisfying the single sibling breakup. Although one has to consider the validity of all the solutions satisfying the previous two conditions, another condition is required to check the validity of the single sibling breakup and to identify the most probable solution out of those satisfying the single sibling breakup.

According to the observations in many disciplines, nature dictates that any system tends to gain its equilibrium by minimizing its potential energy. This led to the total potential energy minimization theory [23], i.e. "The total potential energy of a structure has a stationary value when the structure is in equilibrium. If the equilibrium is stable, the stationary value is minimum. If the stationary value is not minimum, the equilibrium is not stable."

The energy minimization technique has been used in simulating the drop breakup by many previous investigators [16-18,24]. This technique is mathematically preferable because it enables the determination of the final state of any system without any prior knowledge of how the system reaches this final state.

The other widely used principle in solving thermodynamic and chemical reaction problems is the maximization of entropy. The statistical definition of entropy is [25];

" Entropy is the measure of the randomness degree of a system. The approach to equilibrium in a spontaneous process may be considered as a change from a less probable to a more probable state, in sense of the laws of chance. In the cases at which the different probable configurations are of different energy levels, the probability of each individual configuration is not unity, but must be in effect weighted by a factor dependent upon the energy difference between the particular configuration and the configuration of lowest energy."

From this definition, one can see that, statistically, the most probable configuration of the system is the one of minimum energy. Collen [26] discussed the relationship between the two principles and showed that the principle of maximum entropy is equivalent to, and replaced by, the principle of minimum energy. Kelly [27,28] used the entropy maximization technique in his electrostatic-spray theory. His results showed that for liquid droplets larger than about 1 um, the actual sprays conform to the minimization of energy.

In this study, the energy minimization of the total potential energy at the breakup (E_f) is used as a further condition to identify the most probable breakup configuration.

2.2.2 Results and Discussion

Numerical evaluation of the previous equations for water droplets having an initial radius of 100 μm and surface tension of 72.5 mN/m leads to the results indicated in Figures (2.3 - 2.5).

Figure 2.3 tests the stability condition of the final state to insure a single sibling solution. It displays the ratio of both the sibling charge (Q_2) and the sibling effective charge (Q_{E2}) to its Rayleigh limit charge as a function of the sibling mass ratio. It illustrates that for all the values of sibling mass ratio greater than 11.1%, both the sibling charge and the effective sibling charge are less than the Rayleigh limit. In this range of sibling mass

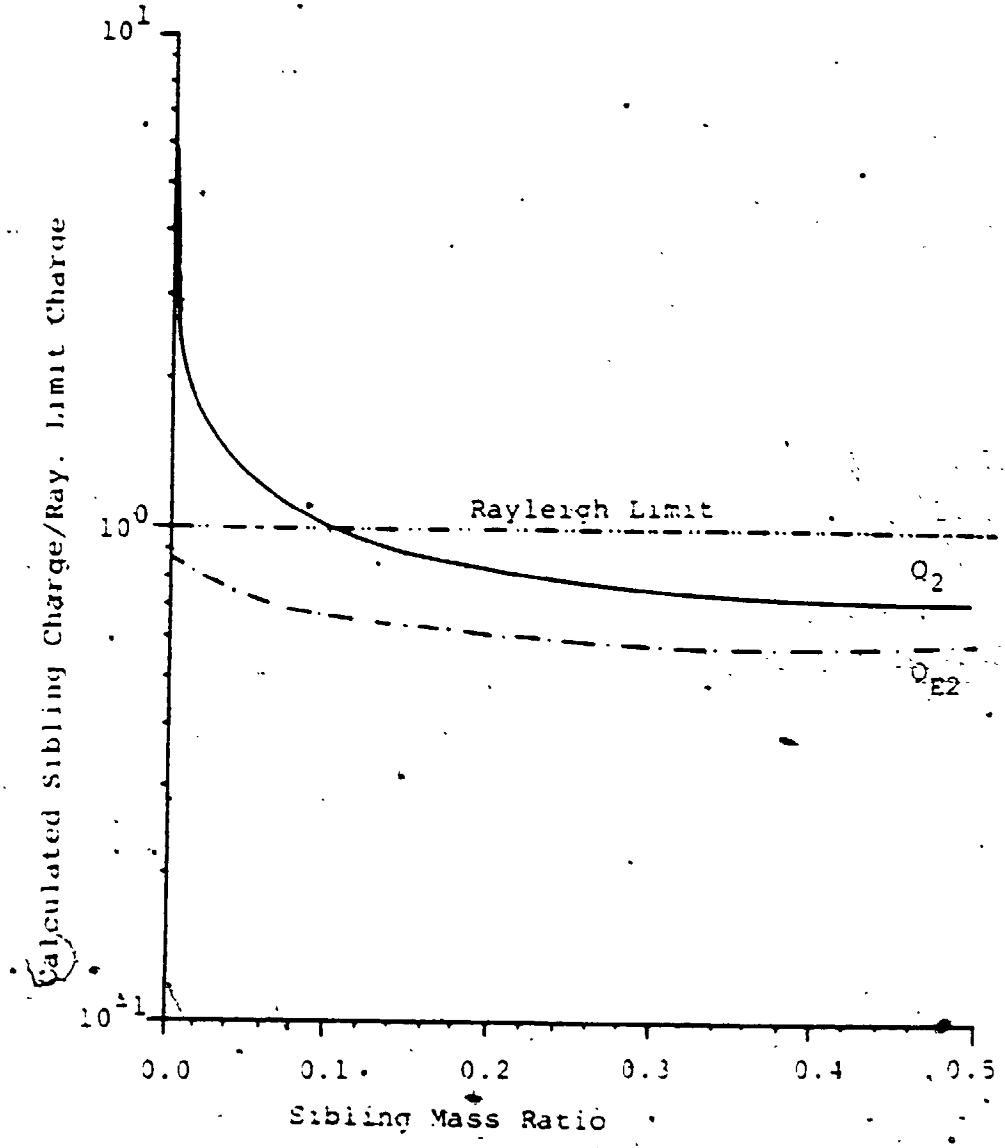

Figure 2.3 The Ratio of Both Q_2 and Q_{E2} to the Sibling Rayleigh Limit as a Function of the Sibling Mass Ratio.

ratios, stable single sibling solutions exist. It is interesting to notice here that this range coincides with the experimental observations of Ryce and Patriarche [17]. For the values of sibling mass ratio less than 11.1%, although the effective charge (Q_{E2}) is less than the Rayleigh limit, the sibling charge (Q_2) is higher than this limit. As the distance between the residual drop and the sibling increases, Q_{E2} tends to Q_2. This will cause other disintegrations to produce the final stable condition. This corresponds to a multi-sibling breakup. This case will be discussed in detail in Section 2.3. The numerical results indicate that both the residual drop charge (Q_1) and its effective charge (Q_{E1}) are always less than the residual drop Rayleigh limit. Thus the residual drop remains stable until the drop reaches its limit again as evaporation proceeds.

Figure 2.4 represents the ratio of the final energy to the initial energy of the system as a function of the sibling mass ratio. It illustrates that the final minimum energy exists at a final energy of about 75% of the initial energy. The sibling under this condition carries about 25% of the initial mass and an actual charge of about 40% of the initial charge. The numerical results at the final minimum energy indicate that both the sibling and the residual drop carry charges far below the Rayleigh stability limit. These

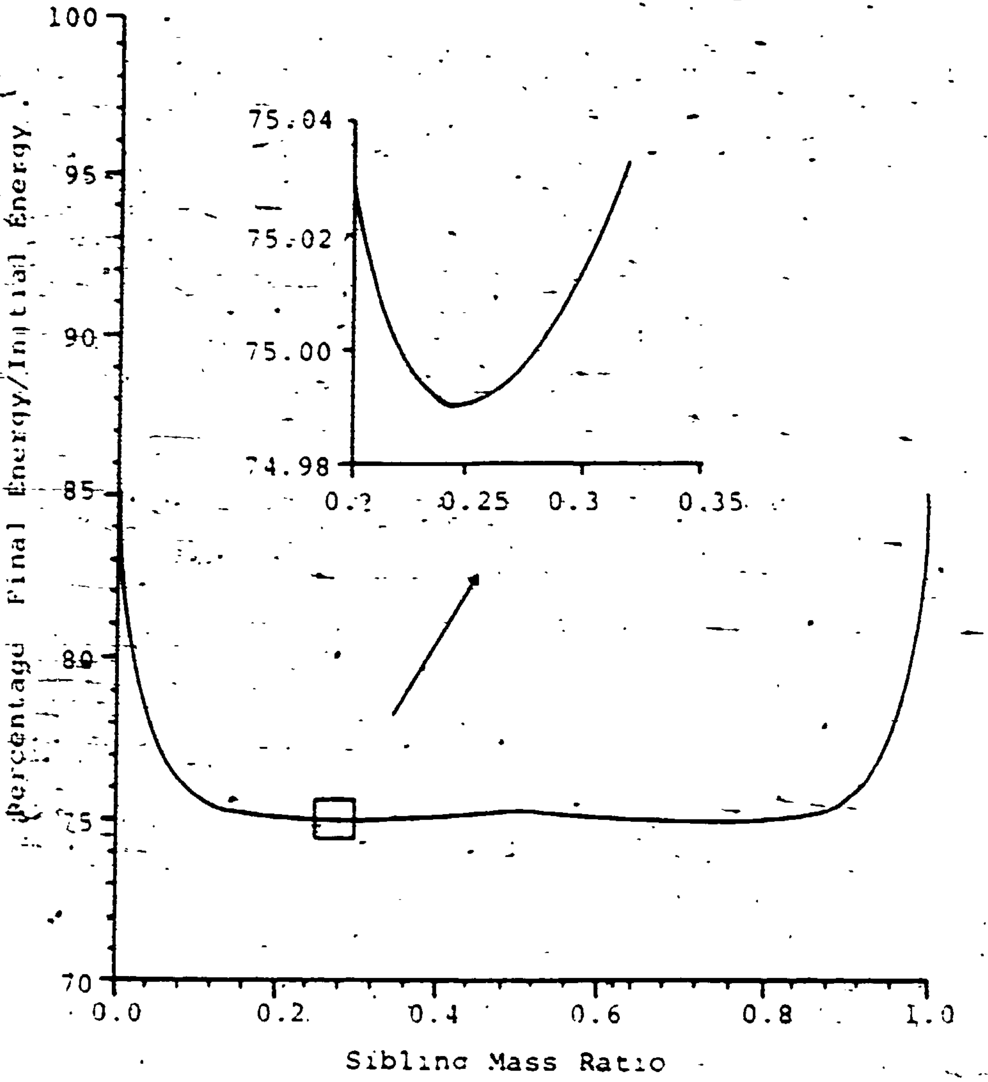

Figure 2.4 Percentage Ratio of the Final Energy to the Initial Energy as a Function of the Sibling Mass Ratio.

results predict that under these conditions, the single sibling breakup is the most probable splitting. Figure 2.4 also shows that the difference between the final energy and the minimum final energy is very small for a very wide range of sibling mass ratios (from about 0.1 to 0.9) and thus can be easily affected by any external force. This explains clearly why the drop disruption is so dependent upon the experimental circumstances. Notice that a mirror image exists around the sibling mass ratio of 0.5 at which a point of inflection exists. As indicated earlier, the value of energy at this point was mistakenly considered by Ryce and Wyman [16] to be the minimum energy. Figure 2.4 also illustrates that the total potential energy at the breakup is always less than the initial energy for all the values of the sibling mass ratio. Assuming the difference between the initial and the final minimum energy (about 25% of the initial energy) all changes to kinetic energy, i.e. lossless case. Equations 2.9 and 2.10 lead to the maximum estimated values of the droplets' velocities at the breakup, i.e.

$Ve_1 = 1.04$ m/s

and

$Ve_2 = -3.17$ m/s

It is interesting to note here that by calculating the distance between the two droplets at the breakup using the catenary assumption (Eq. 2.5), one can estimate the minimum time of the breakup by applying Newton's law. This leads to an estimated breakup time of ~ 0.13 ms which is more than two orders of magnitude greater than the relaxation time of normal tap water. Since a liquid of high volume conductivity was previously assumed to have a high surface ion mobility, the above result supports the validity of using the assumption of a conductive liquid in modelling the breakup phenomenon.

Figure 2.5 displays the ratio of both the effective and the actual sibling charges to the initial charge as a function of the sibling mass ratio. It also includes some previous experimental observations. Physically, the sibling does not carry its effective charge after the breakup. However, some of the previous investigators underestimated the sibling charge by neglecting the interaction effect between the droplets and hence, their results could in fact be considered to be closer to the effective charge rather than the actual charge. Abbas and Latham used the measured time taken by the residual drop to fall a vertical distance of 6 cm to calculate the drop drag force. From the force balance equation, they calculated the residual drop charge. Because they neglected the repulsion force between the two droplets at the breakup, their results probably led to an overestimation of the residual charge. This in turn led to

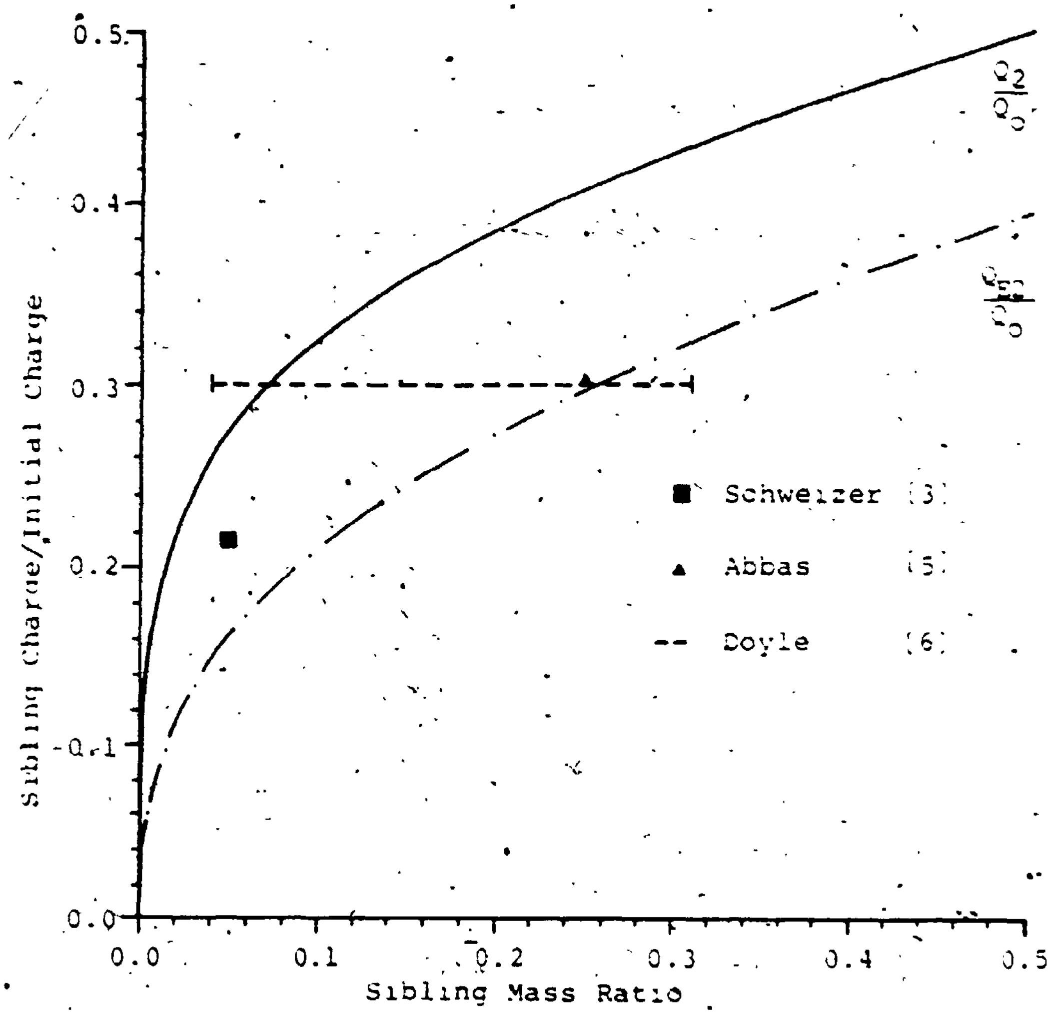

Figure 2.5 The Ratio of the Sibling Charge to the Initial Charge as a Function of the Sibling Mass Ratio

an underestimation of the sibling charge. Similarly, Schweizer and Hanson used the sudden change of the oscillation of the drop at its breakup to calculate the residual drop charge without considering the interaction effect between the droplets. As a consequence their results would also lead to underestimation of the sibling charge. As Figure 2.5 shows the two extremes of the sibling charges that could be measured experimentally, it is clear that the experimental data reported by the previous investigators are in good agreement with the values obtained by this analysis. It can also be observed that the results reported by Abbas and Latham are very close to the theoretical values of the effective sibling charge.

Table 2.1 summarizes the calculated results at the margin of stability and the minimum energy condition. It also includes some previous experimental observations. It is seen that excellent agreement exists with Abbas and Latham's data for the minimum energy condition. Although the calculated charge losses during the disruption are also in good agreement with the data introduced by other investigators [3,6], the calculated mass losses are not comparable to their results that involve multi-sibling conditions. However, the data introduced by Doyle and his colleagues [6], fall within the predicted results for all the initial drop diameters less than 70 um.

Table 2.1

Comparison Between the Calculated Values and the Experimental Observations

Ratio	Satisfying the Condition of Stability	Satisfying the Minimum Energy Condition	Experimental Observations		
			Abbas et al [5]	Doyle et al [6]	Schweizer et al [3]
M_2/M_0	11.1%	25.0%	25%	1-10 siblings of 15 μm diameter	5%
Q_{E2}/Q_0	22.0%	29.8%	30%	30%	23%
$Q_2/Q_{2(R.L)}$	100.0%	81.7%			
$Q_1/Q_{1(R.L)}$	70.7%	68.1%			
E_f/E_i	79.5%	75.0%			

The previous discussion indicates that although the single sibling breakup exists for all the values of [illegible]ing mass ratio greater than 11.1%, the most probable particle splitting exists when the total final energy is minimized. It also enhances the belief that any external forces would cause the disintegration to vary from the minimum energy state. Table 2.2 summarizes the calculated data at the minimum energy for a drop unaffected by any external force.

It is important to note here that the value of the initial drop size or the type of liquid does not change the results significantly. The same analysis was carried out for assumed spherical drops of aniline and water covering the range up to 200 µm diameter in NTP air (Normal Temperature and Pressure). The results showed that the sibling mass ratio and its charge ratio were constant within a standard deviation of 2%. This result is implied in the experimental data introduced by many of the previous investigators [3,5,6]. For drop diameters greater than 200 µm [5], or for high relative humidity [8,29], the assumption of ignoring the charge loss by electron avalanches might not be satisfied. The drop size under such conditions might have a significant effect on the results.

Table 2.2

Calculated Data at the Minimum Energy for the Droplets Unaffected by Any External Force

$\frac{R_1}{R_0}$	$\frac{R_2}{R_0}$	$\frac{Q_1}{Q_0}$	$\frac{Q_2}{Q_0}$	$\frac{Q_{E1}}{Q_1}$	$\frac{Q_{E2}}{Q_2}$	$\frac{Q_{E1}}{Q_0}$	$\frac{Q_{E2}}{Q_0}$
91%	62.6%	59.2%	40.8%	83%	72%	49.5%	29.8%

2.3 Multi-Sibling Disruption Model

In this section, the mathematical model of the single sibling case has been extended to predict the final state after the breakup for a multi-sibling disintegration. Following the assumptions and the results of the single sibling model, Section 2.2, it is assumed that

1- The initial drop is conductive so that the droplets just before disintegration are at the same electrical potential.

2- The final state consists of a residual drop and some siblings modelled as spherical droplets.

3- The most probable particle splitting exists when the final energy is minimized.

2.3.1 Theory

It is suggested that a liquid drop might disintegrate below the Rayleigh limit if the difference between the surface tension force and the electrical force of repulsion is overcome by any other external force (F). The major external forces acting on a drop in an electrostatic spraying or painting system are the aerodynamic force, gravitational force and the electrical force exerted by any external field. The effect of each of these forces on the breakup of charged and non-charged drops is discussed in Chapter 4.

2.3.2 The Initial State

It is expected that the external forces will change the limit at which a drop becomes unstable as well as the behaviour of the breakup. In the present part of the study, the effect of the external forces in changing the charge limit of the drop is only considered through a primary modification of the Rayleigh limit. The initial charge limit of a drop of radius (R_0) is assumed to be;

$$Q_0 = 8\pi\,(\nu_{eff}\,\epsilon_o R_0^3)^{1/2} \qquad 2.11$$

where ν_{eff} is the effective surface tension of the liquid. This can be expressed as;

$$\nu_{eff} = \nu - f(F,R_0) \qquad 2.12$$

This parameter accounts for the effect of the external forces on reducing the initial charge limit. This reduction is due to the external forces opposing the surface tension force. At this stage the effect of the external forces in distorting the spherical shape and hence redistributing the surface charge is neglected due to the small size of the droplets. Although Equation 2.11 looks very close to Equation 2.1, introduced by Ryce and Wyman [16], the parameter ν_{eff} is different than the numerical parameter ν in its physical significance.

The initial energy (E_1) can also be calculated as:

$$E_1 = 4\pi\nu R_0^2 + \frac{Q_0^2}{8\pi\varepsilon_0 R_0} - \Sigma\int F.dx$$

$$= 4\pi\nu_{eff} R_0^2 + \frac{Q_0^2}{8\pi\varepsilon_0 R_0} \qquad 2.13$$

where x is a distance parameter representing the path on which the force F acts on the drop. Then

$$\nu_{eff} = \nu - \frac{1}{4\pi R_0^2}\Sigma\int F.dx \qquad 2.14$$

It is clear from Equation 2.14 that the effective surface tension is a function of the drop size and the external forces. The final minimum energy would exist at a sibling mass ratio different than that calculated for an isolated drop which yields to a single sibling condition, Table 2.1. This deviation is also a function of both the drop size and the external forces.

From the previous set of equations the drop charge at the breakup point and the initial energy of the system, for a certain drop of radius R and surface tension γ, can be calculated with known external forces acting on the drop. However, it is not an easy task to define $\int$F.dx for many of the external force types. In the present study, although Equation 2.14 is not solved for a predetermined external force, the behaviour of the breakup of the drop due to the external force effects is determined by assuming a certain effective surface tension and considering all the possibilities of the minimum energy deviations through a numerical scan.

2.3.3 The Intermediate State

Following the analysis of the single sibling breakup, Section 2.2, the initial drop is assumed to disintegrate to a single sibling and a residual drop of radii R_2 and R_1 respectively. From the previous analysis, the results of Figure 2.3 show that for all the values of sibling mass ratio less than 11.1%, the sibling carries charge (Q_2) higher than the Rayleigh limit, while the effective charge of the sibling (Q_{E2}) is less than this limit. As the distance between the residual and the sibling drop increases, the charge Q_{E2} tends to Q_2. This causes some other disintegrations to produce a final stable condition as shown in Figure 2.6.a. In this stage it is assumed that the effect of the external force is dominant only on the initial drop in changing the sibling mass ratio at which the minimum energy occurs. For any further sibling disintegrations, due to the small size of the droplet, the external force effect is neglected and the new disintegration satisfies the single sibling condition at the minimum energy, i.e:

$$\frac{Q_1'}{Q_2} = 0.592 \qquad \frac{Q_2'}{Q_2} = 0.408$$
$$\frac{R_1'}{R_2} = 0.91 \qquad \frac{R_2'}{R_2} = 0.626 \qquad 2.15$$

where Q_1' is the actual charge of the secondary residual drop of radius R_1' after the first sibling disintegration, and Q_2' is the actual charge of the secondary sibling of radius R_2' after the first sibling disintegration. This process of sibling disintegration is assumed to be repeatable in a tree like form until all the droplets carry charges less than their Rayleigh limit charge. This assumption satisfies the experimental observations of Ryce and Patriarch [17].

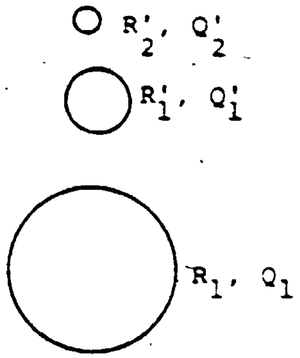

(a) The Intermediate State

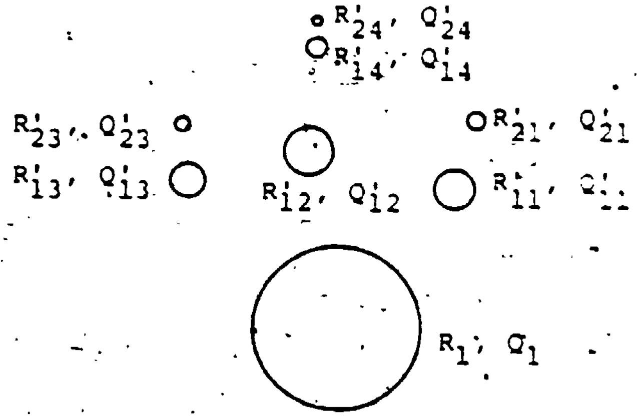

(b) The Final State

Figure 2.6 The Multi-Sibling Breakup Process

2.3.4 The Final State

The system in this state consists of an initial residual drop and a cloud of siblings divided into groups of droplets as shown in Figure 2.6.b. Each group consists of one or two droplets and each of these droplets can be described by either a secondary residual or a secondary sibling according to the last breakup just before the stability. The interaction effect between the droplets of each group is considered. All the other interactions are neglected due to the relatively long distances between the different groups and between each group and the initial residual. Therefore, the initial residual drop will carry charge equal to the actual charge Q_1, while all the siblings will carry effective charges less than their actual charges. The effective charge of these siblings can be expressed in the form of either an effective charge of a secondary residual drop or an effective charge of a secondary sibling. These definitions are only related to the last breakup before the stability. From the analysis of the single sibling breakup, the following ratios can be obtained at the minimum energy state:

$$\frac{\text{Effective charge of the secondary residual drop}}{\text{Actual charge of the secondary residual drop}} = 0.83$$

$$\frac{\text{Effective charge of the secondary sibling}}{\text{Actual charge of the secondary sibling}} = 0.72 \qquad 2.16$$

Therefore,

$$\begin{aligned} &\text{the total effective sibling charge} \\ &= 0.83\ [\Sigma \text{ actual charge of the secondary residual drops}] \\ &+ 0.72\ [\Sigma \text{ actual charge of the secondary siblings}] \end{aligned} \qquad 2.17$$

2.4 Analysis and Results

A numerical evaluation of the previous equations for water droplets having initial radius of 100 μm with an assumed effective surface tension (γ_{eff}) of 70 mN/m was performed. This value of the effective surface tension was chosen only 3.5% less than the actual surface tension to insure that the effect of the electrical charge on the drop instability was dominant. However, the numerical evaluation of the results at different effective surface tensions showed that the value of the effective surface tension was not crucial to the results of this model due to the normalization used in presenting the behaviour of the breakup. Figure 2.7 illustrates the flowchart of the calculations at which the sibling radius is chosen and changed in steps of 1/1000 of the initial radius to scan all

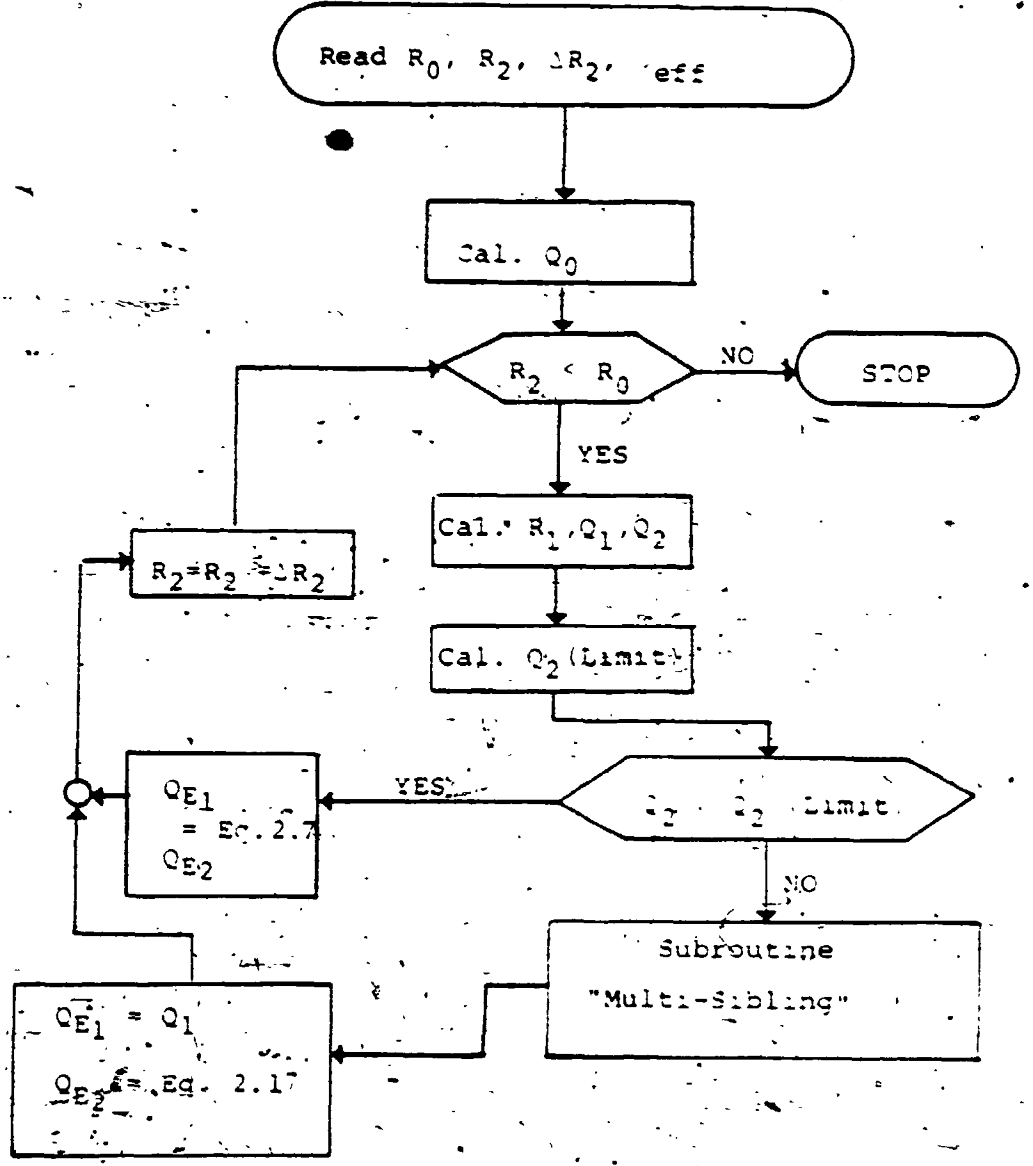

Figure 2.7 Flowchart of the Program

the possibilities of the sibling radii. For all the values of actual sibling charge (Q_2) greater than its Rayleigh limit, the sibling disintegrates to a secondary residual and a secondary sibling droplet [17]. This secondary breakup is assumed to satisfy the minimum energy conditions for a single sibling breakup, Table 2.2. The secondary droplets are then examined to insure a stable solution. If any of their charges are higher than the Rayleigh limit, further disintegrations will take place. Finally, the total effective charge of the siblings is calculated using Equation 2.17. In the numerical evaluation of this model, the number of the secondary droplets are limited to a maximum of 32 to simplify the model and to reduce the calculation time.

Figure 2.8 displays the ratios of both the effective and actual sibling charges to the initial charge as a function of the sibling mass ratio. It also includes some experimental observations reported by Abbas et al [5], Doyle et al [6] and Schweizer et al [3]. It is clear that the experimental data reported by those investigators are in good agreement with the results obtained by this analysis. The discontinuity in the effective charge curve at 11.1% of the sibling mass ratio separates the two different modes of breakup (single sibling and multi-sibling disintegrations). It exists because in the multi-sibling case, the interaction

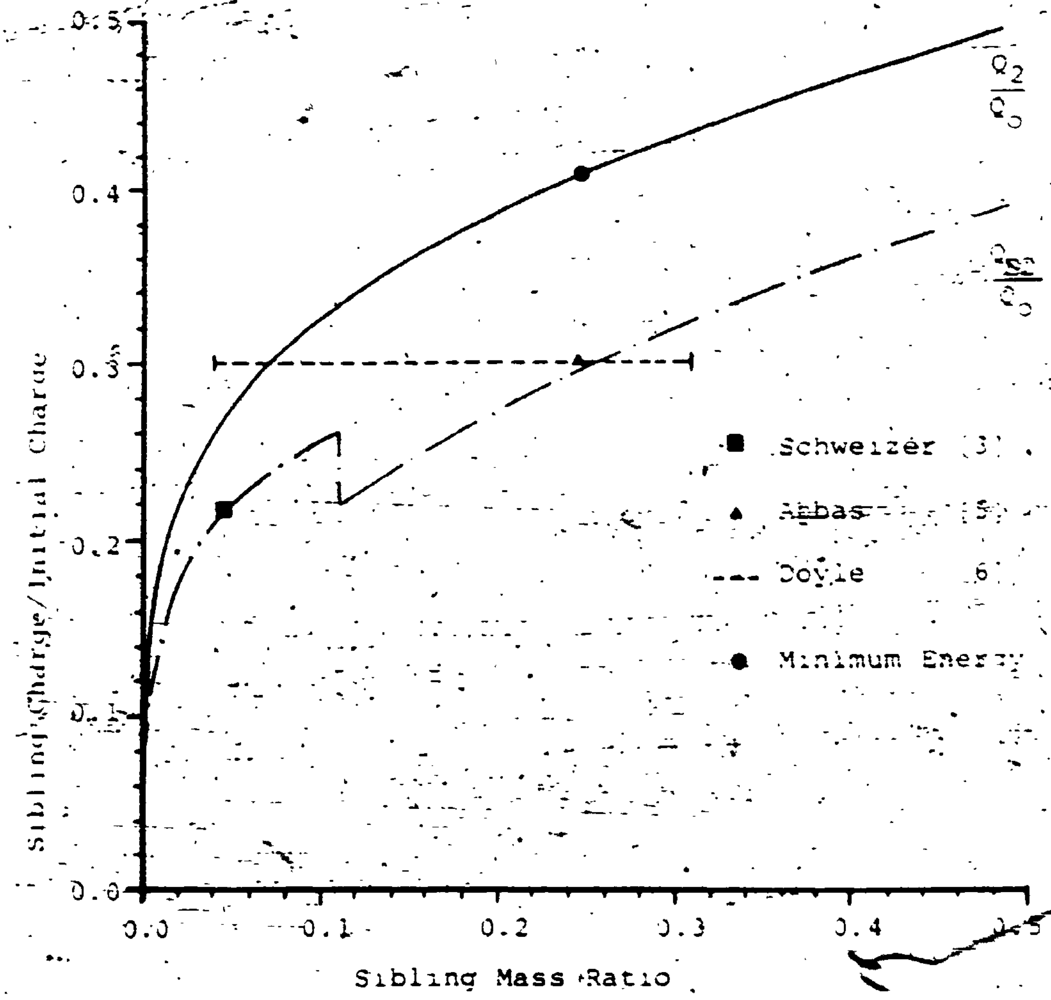

Figure 2.8 The Sibling Charge/Initial Charge as a Function of Sibling Mass Ratio

effect between the residual drop and the siblings is much less than that in the single sibling case due to the relatively longer distance separating them at the final state. This increases the effective charge of the residual drop and the siblings as well. As far as the actual charge on the sibling is concerned, Figure 2.8 also shows that at the minimum final energy of a drop unaffected by any external force, the sibling carries about 40% of the original charge. For lower sibling mass ratios, the sibling charge decreases.

Figure 2.9 shows the number of secondary droplets which may be emitted from the initial drop at each value of the sibling mass ratio. It indicates that the multi-sibling breakup exists for all the values of sibling mass ratio less than 11.1%. The maximum number of siblings appears to be 20 which is less than the maximum limit (32 siblings) utilized in the program. It also shows that the number of siblings increases as the sibling mass ratio decreases. It is interesting to note here that, this model does not predict the formation of certain numbers of siblings (i.e. 4,5,7,8...etc.). However, the estimated number of siblings at any sibling mass ratio represents the minimum number of siblings which can be ejected under the assumption of negligible external force effect on the secondary disintegrations. This assumption is quite reasonable when

Mass Ratio at Transition

Number of Siblings	Percentage Mass Ratio
1 - 2	11.1%
2 - 3	5%
3 - 6	2.2%
6 - 9	1%
9 - 13	0.4%
13 - 20	0.15%

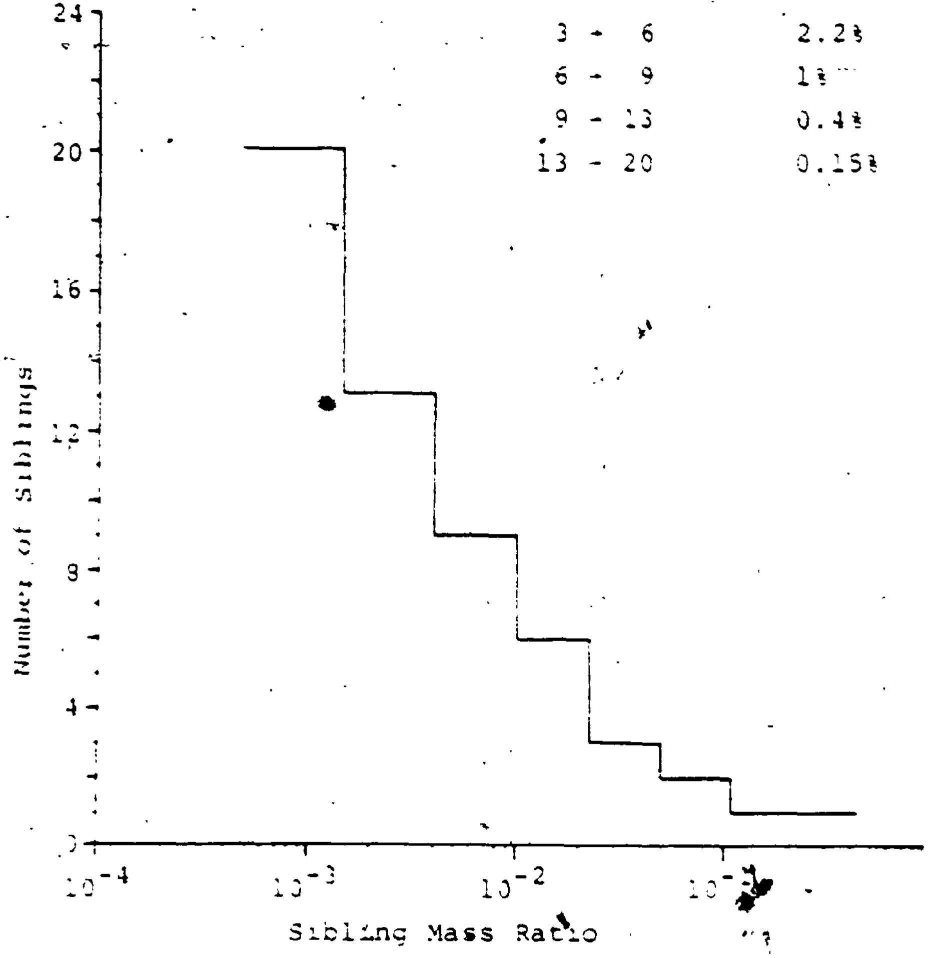

Figure 2.9 The Number of Siblings as a Function of the Sibling Mass Ratio

the external forces represent only a few percent of the total forces opposing the surface tension force. For higher percentage of the external forces, more siblings should be expected at each range of the sibling mass ratio.

As this model is a continuation to the previous single sibling case and due to the assumption of constant effective surface tension, its results are independent of the initial drop size. However, for drop diameter greater than 200 µm. [5], high relative humidity [8,29] or for low pressure [30], the assumption of spherical drop as well as the assumption of ignoring the charge loss by electron avalanches might not be satisfied. The drop size under such conditions will have an important role on changing the results. The effect of the external forces on the effective surface tension is a function of the initial drop size as well. This might change the mode of breakup as the initial size changes. For very large initial drop size, the assumption of negligible external force effect on the secondary disintegrations might not be valid. A more careful treatment of these disintegrations will then be required.

2.5 General Discussion

The results of the previous analysis show that both the single sibling and the multi-sibling breakup models can be used to describe the drop disintegration and to estimate the final state of a drop approaching its Rayleigh limit.

Although the maximum number of siblings (20 siblings) coincidentally appears to be the same as that reported by Ryce et al [17] and by Pfeifer et al [18], no significance should be concluded from this due to the differences between their models and the present one. These differences and the advantages of the present model can be summarized as follows:

1- Their models are based on a disruption of the drop into (n) identical drops while the present model is based on tree like secondary breakups which lead to a residual drop and (n) siblings of different sizes and charges. The present model is supported by the photographic results introduced by Ryce et al [17].
2- The present model always preserves the conservation of energy.
3- It clarifies the limits separating the two modes of breakup (single sibling and multi-sibling) and gives a more physical explanation to the effect of the external forces on the disintegration of a liquid drop below its Rayleigh limit.
4- The present model is supported by the experimental data reported by other investigators [3,5,6].

From the results of the present analysis, the following conclusions are derived:

1- The most probable particle splitting exists when the total final energy is minimized. Any external force causes the disintegration to vary from the minimum energy state. This variation is a function of the external force.

2- The single sibling breakup exists for all the values of sibling mass ratios greater than 11.1%. For all the values less than this, multi-sibling disintegration is favoured.

For non-conducting liquid drops, the previous model is not valid. A further model for such liquids is required to take into account the effect of the ion mobility on the charge distribution over the drop surface. A further study is also required to define the time required for the drop disruption for different liquids. Comparing this time with the time required to distribute the charge over the drop surface, one can determine the liquids which can be considered conductive. In practical situations, any liquid which can be effectively charged by induction will have a conductivity which may be assumed high enough to satisfy this model.

CHAPTER THREE

EXPERIMENTAL RESULTS

3.1 General Description of the Apparatus

The purpose of this part of the study was to observe the breakup phenomena of charged liquid drops and to examine the validity of the analytical model given in Chapter 2. The experimental set-up used is given schematically in Figure 3.1. It consisted of a stainless steel hypodermic capillary tube of 150 μm inside diameter and 450 μm outside diameter. Tap water coloured with dye was fed from the reservoir to the capillary tube. The height of the reservoir was varied in order to control the hydrostatic pressure, which in this experiment was established to be very close to zero, i.e. no dripping. A high voltage power supply was connected to the liquid reservoir to charge the water by conduction. Two identical copper rings, 3.8 cm inner diameter and 1.3 cm height, were mounted separated by a vertical distance of 1.5 cm. The upper edge of the first ring (detection ring) was aligned with the capillary tube tip. This ring was grounded through an electrometer (Keithley Instruments model 602), set to its current mode. The electrometer measurement was amplified and traced on an oscilloscope (Tektronix 5223 Digitizing Oscilloscope) to

1- Reservoir.
2- Capillary tube.
3- Detection ring.
4- Field ring.
5- Faraday cage.
6- Power supply (± 1200 V).
7- H.V. power supply (32 KV).
8- Control of the reservoir height (50 mm in steps of 0.01 mm).
9- Band reject filter.
10- Oscilloscope.
11- Electrometer.
12- Coaxial cable.
13- Flexible tube.
14- H.V. cable.

Figure 3.1 Schematic Diagram [illegible] the Experimental Set-up.

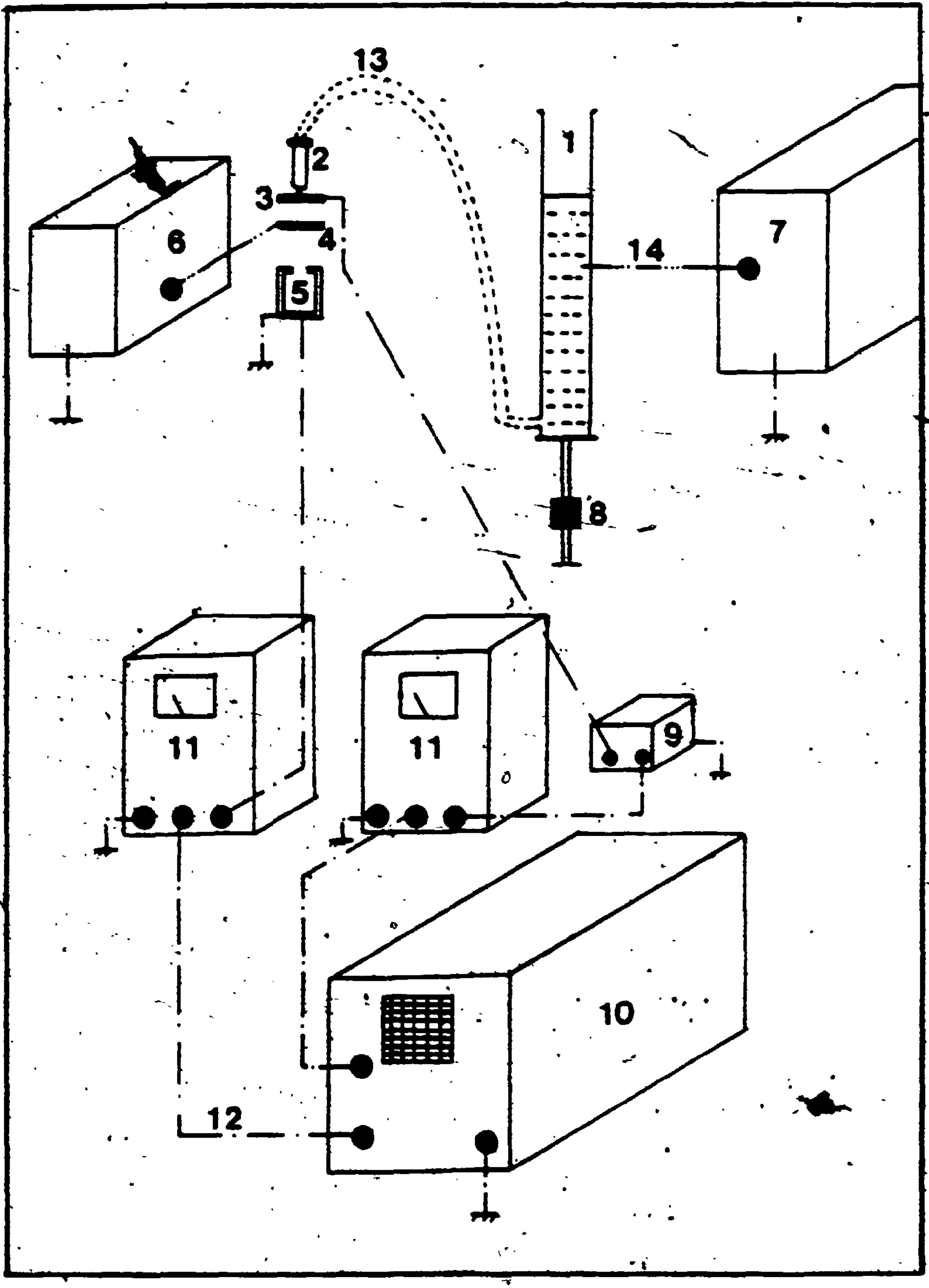
13
1
2
3
4
6
5
14
7
8
11
11
9
10
12

sense any dripping and breakup of the water drops. Another D.C. power supply was connected to the second ring (field ring). This ring allowed the fine adjustment of the electric field around the capillary tube. It also served the purpose of centering the droplets which were captured in a double shielded Faraday cage, 6.1 cm below the capillary tip. The Faraday cage was also grounded through a similar electrometer and its signals were traced on the second channel of the oscilloscope to count the number of droplets entering the cage.

To reduce the external electrical noise, mainly from the 60 Hz pick-up, the capillary tube, the two rings and the Faraday cage were mounted in an electrically shielded chamber. A band reject filter (40 -100 Hz) was connected in the detection circuit between the electrometer and the oscilloscope to eliminate the 60 Hz noise.

3.2 Power Supplies

Two power supplies were used in this experiment. The first was a Universal Voltronics high voltage D.C. power supp~~ly, m~~odel BAL32-25. The output voltage was continuously adjustable from zero to 32 kV with a maximum output current limited to 25 mA. Its output voltage which was used to charge the water was measured using a digital multi-meter

(Fluke model 8050A) with potential divider (1/1000 probe). The second power supply was a Keithley Instruments D.C. power supply model 240A. It was used to change the local electric field around the capillary tube. Its output voltage was calibrated and adjustable in steps of 1 volt from zero to 1200 V with maximum current limited to 10 mA.

3.3 Determination of Nozzle Characteristics

Some preliminary experiments were carried out to determine the characteristics of the drops ejected from the nozzle under different charging voltages or ring voltages (i.e. different fields around the nozzle tip). In each of these experiments either the charging voltage or the ring voltage was kept constant and the other was changed in steps to cover all the possible ranges of drop size.

During the experiments, drops which formed at the nozzle tip became charged then fell through the ring system into the Faraday cage. The second channel of the oscilloscope was used to sense the arrival of a drop in the cage and to estimate the time between two consecutive drips. Droplet size was measured by collecting 60 samples of the ejected droplets at each combination of charging and ring voltages. Fifteen samples were collected on water sensitive paper, placed on the top of the Faraday cage, and 45 samples were collected in oil (non- drying immersion oil for microscopy type B). The oscilloscope was used simultaneously with the collecting process to check that the collected number of droplets for either single sibling or multi-sibling breakups, for each sample, was equal to that given by the oscilloscope signal detected by the upper ring. If any difference in droplet number occurred, the faulty sample was rejected. A total of 60 acceptable samples were obtained for each of the 30 separate experiments carried out. Since the Tektronix 5223 oscilloscope has the capability of expanding a certain part of the trace, all the measurments were stored originally at 2 sec/division and then the required part was then enlarged to determine the number of siblings (see Plate 4).

The collected droplets were then examined under a microscope (Wild M3 Stereo Microscope 6.4X to 80X magnifications) to measure the drop size and the spreading factor of the water sensitive paper (w.s.p.). The breakup mode of the original drop, if any, was also determined from the number of collected droplets. These experiments also served to check the reproducibility of the results and the measurement of the time between two consecutive drips. In the case of a drop disintegration, the initial drop size was determined by measuring the diameter of each individual drop. Calculating the total mass of these droplets allowed the calculation of the initial drop diameter.

The results of the nozzle characteristic experiments given in Figure 3.2 showed that, for zero ring voltage, the drop size reduced with increasing the charging potential. As the charging voltage was further increased, the drop started to disintegrate after its formation. In this range, labeled as the break-up region in Figures 3.2-3.6, the number of collected droplets increased rapidly with increasing charging voltage. As the charging voltage approached a certain value, slightly higher than that required for drop disintegration, the breakup mode changed to a spraying mode. Figure 3.2 also shows that the time between two consecutive drips decreased with increasing the charging voltage.

In order to obtain better control in the breakup mode, the charging voltage was raised to a value close to that needed for breakup. The ring voltage was then varied in steps, with either positive or negative polarity, until breakup started. This fine adjustment of the ring voltage allowed a fairly wide range of control. Figures (3.3-3.5) show how the ring voltage changed the behaviour of the breakup. They also show that the more positive the ring voltage (the less the electric field concentration at the tip), the larger the drop size and the longer the time

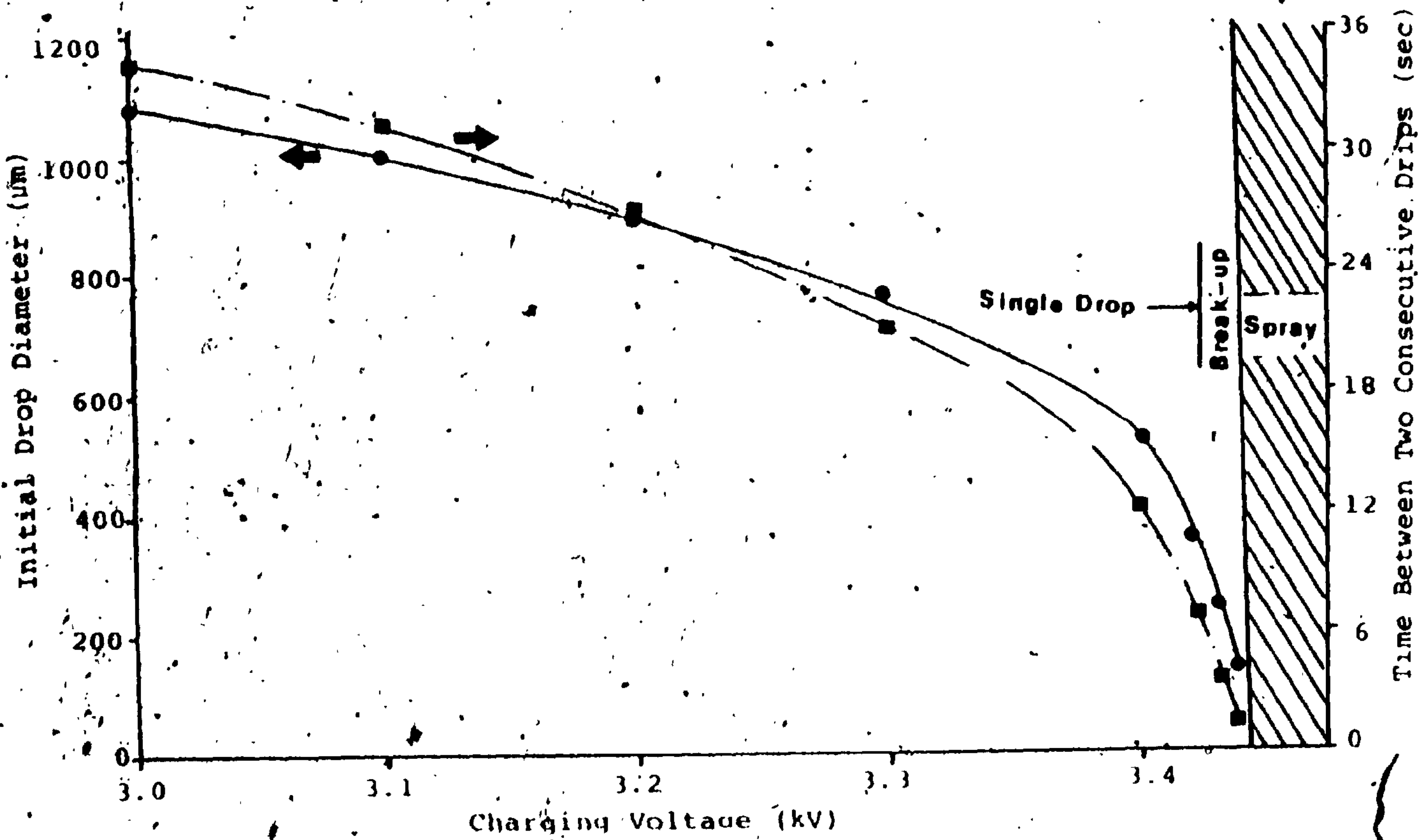

Figure 3.2 Nozzle Characteristics at Zero Ring Voltage

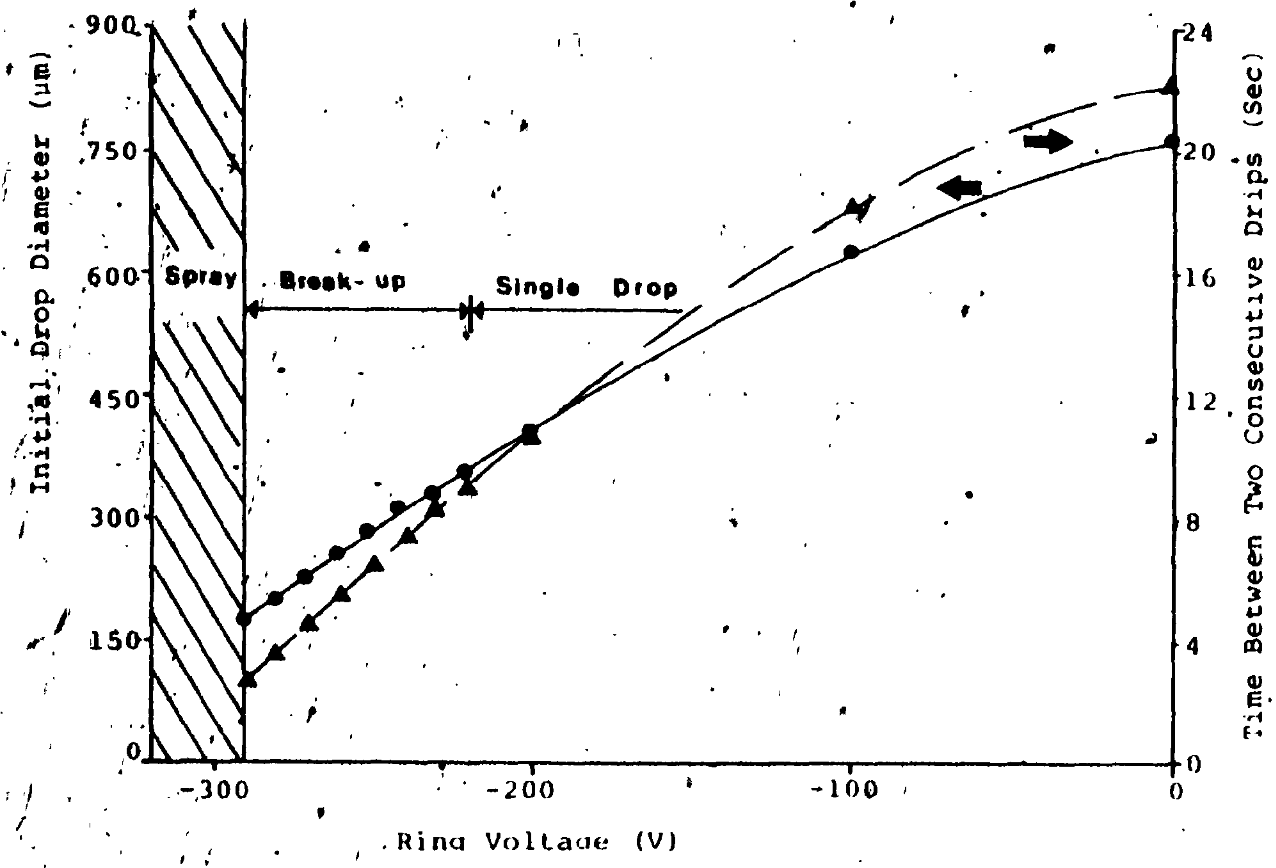

Figure 3.3 Nozzle Characteristics at a Charging Voltage of 3.3 kV.

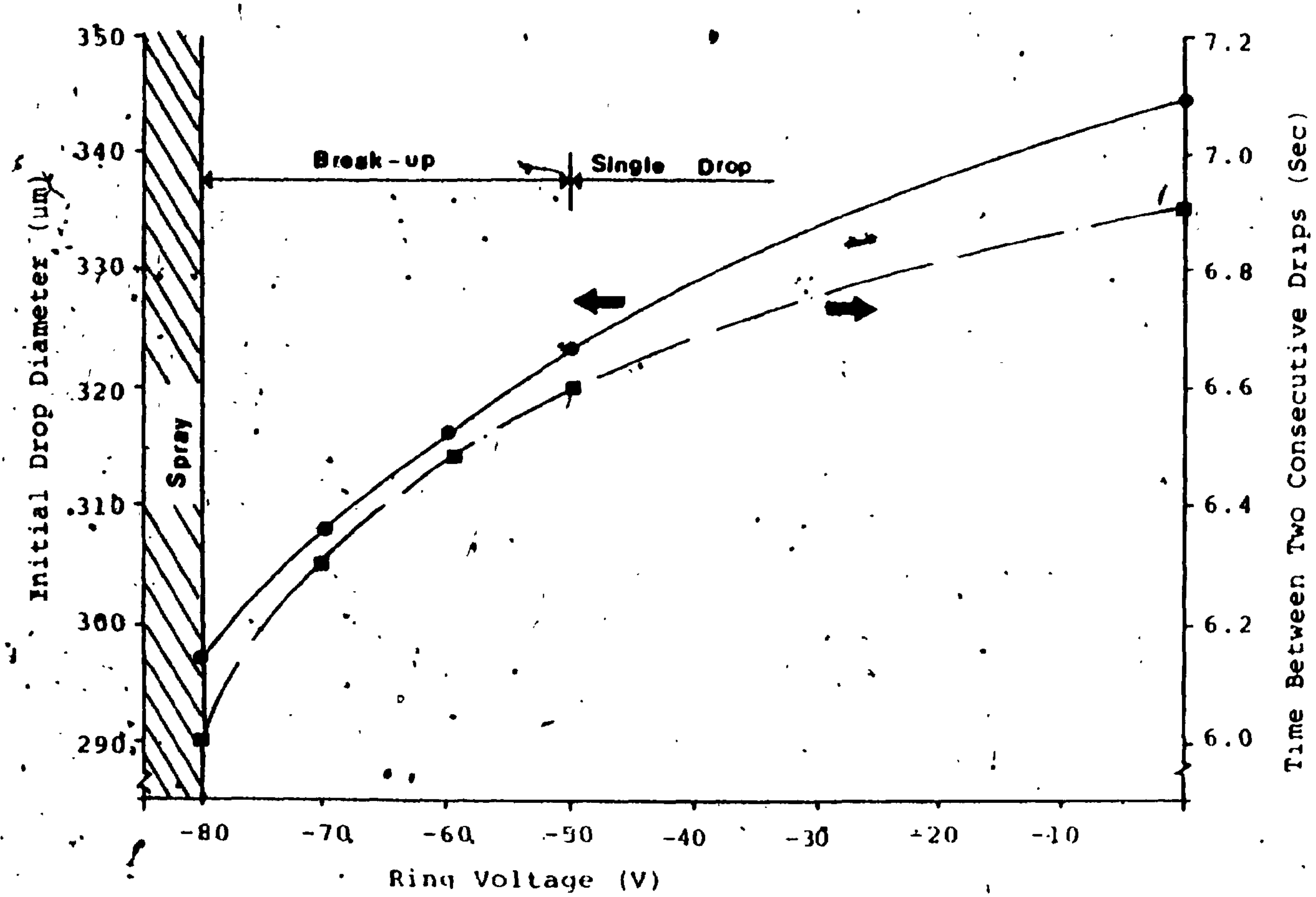

Figure 3.4 Nozzle Characteristics at a Charging Voltage of 3.42 kV.

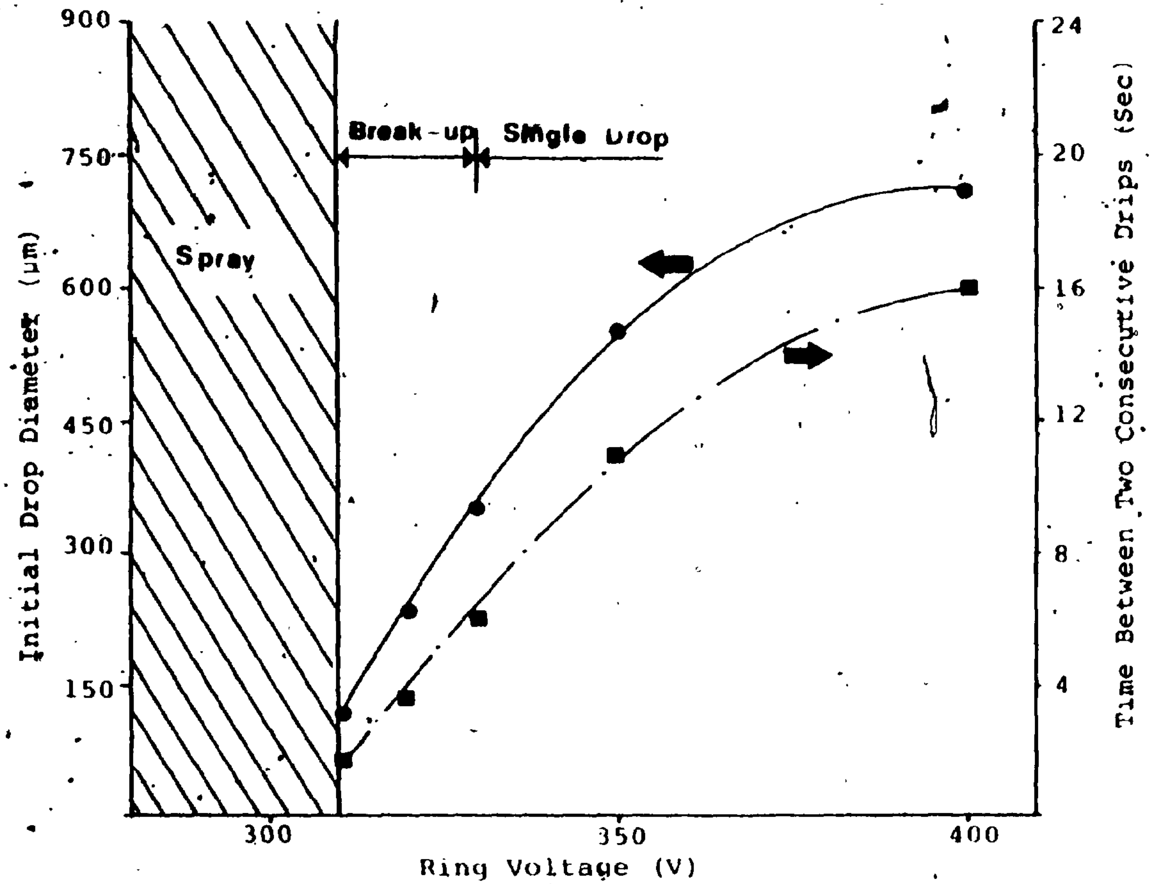

Figure 3.5 Nozzle Characteristics at a Charging Voltage of 3.46 kV

between two drops. The contours of equal size droplets for different charging and ring potentials are given in Figure 3.6 which shows the voltage combinations at which the breakup occurred.

The spreading factor of w.s.p. was also measured at each step by comparing the average drop diameter of those collected on w.s.p. with those collected in oil. For the drop sizes used in performing the breakup tests described in Section 3.4, the spreading factor was found to vary between 2.19 and 2.31 with an average of 2.25. Although the spreading factor showed a trend to increase with the increase of the drop size, for the narrow range of drop sizes used in the breakup tests it was decided to use the average spreading factor in measuring the drop sizes. This is because the use of w.s.p. was much more convenient than the use of an oil dish in capturing the droplets. It also offered an extra magnification of about 2.25 which made the measurement of the very fine droplets easier and more precise. The effect of using the average spreading factor on the measurement accuracy will be discussed in Section 3.6.

Plate 1 presents photographs of 3 separate pairs of magnified collected droplets on w.s.p. and oil where each pair represents samples of the droplets that were collected

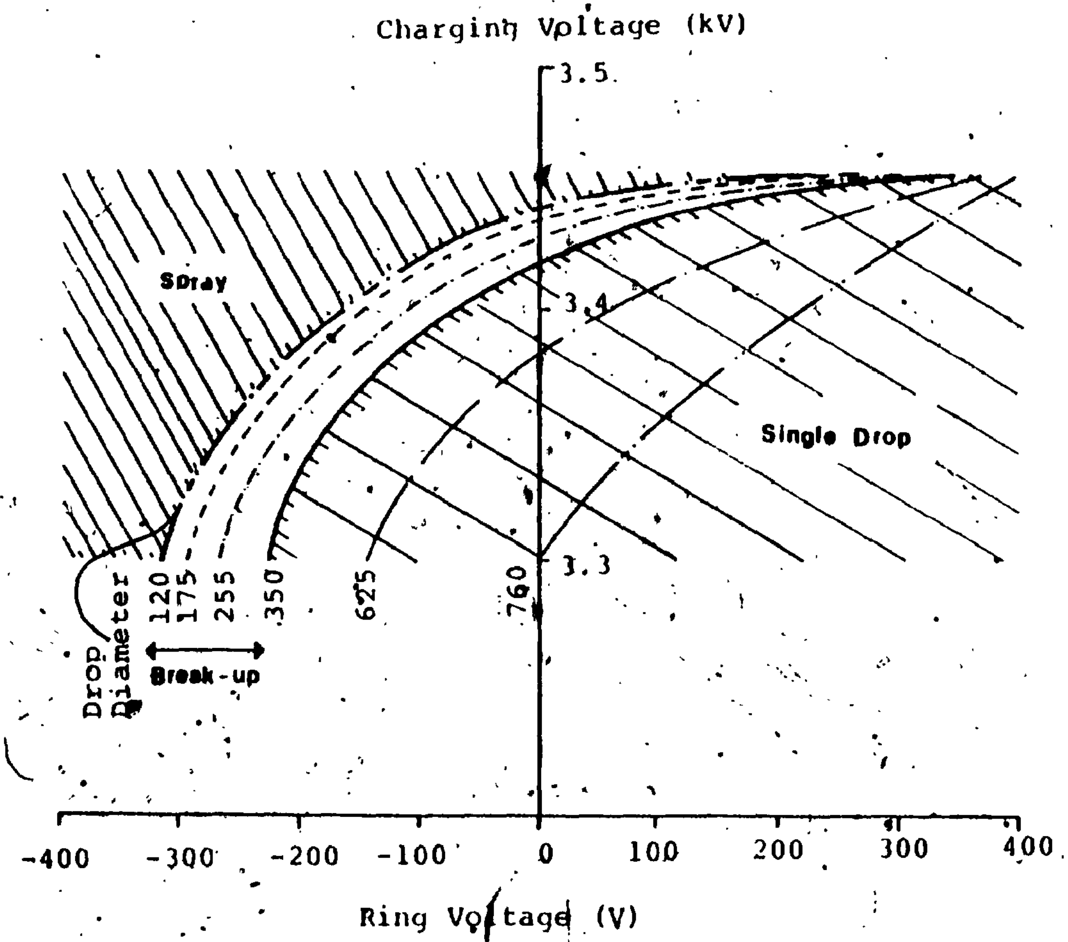

Figure 3.6 Contours of Equal Size Droplets

2

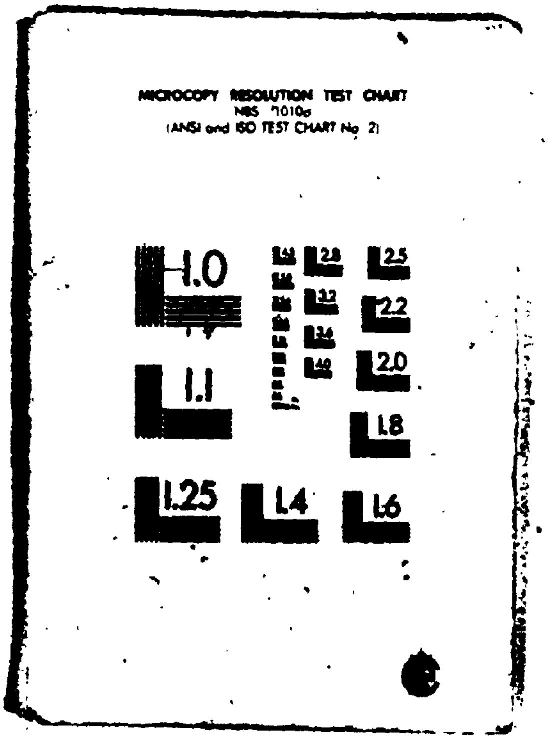
MICROCOPY RESOLUTION TEST CHART
NBS 1010a
(ANSI and ISO TEST CHART No. 2)
1.0
2.8
2.5
3.2
2.2
3.6
2.0
4.0
1.1
1.8
1.25
1.4
1.6

Average Drop Diameter (µm)	Average Spreading Factor	Actual Diameter (mm) On Contact Print	
		In Oil	W.S.P.
570	2.26	7.3	16.5
475	2.29	6.1	14.0
380	2.26	4.9	11.1

Plate 1 Samples of Collected Droplets on Water Sensitive Paper and Oil.

(Microscope Magnification = 12.8)

In Oil

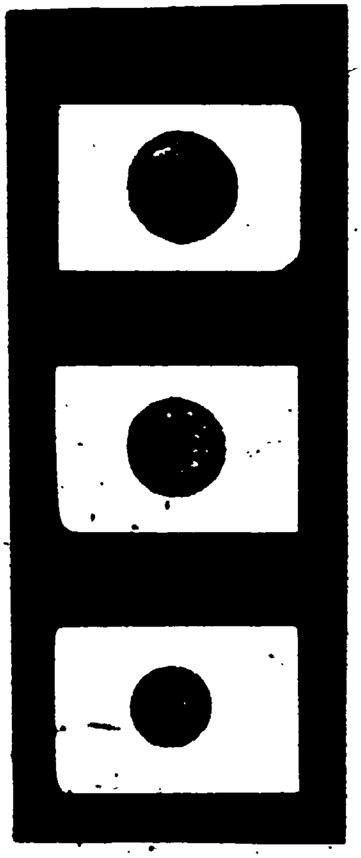

On W.S.P.

under the same condition of charging and ring voltages. In all these photographs, the microscope magnification was 12.8X. Plate 1 also presents the average drop diameter and the average spreading factor which were calculated from the total of 60 samples for each pair as well as the actual diameter of each of the magnified droplets shown in these photographs.

3.4 Breakup Tests

The objective of this experiment was to determine the number of siblings for different sibling mass ratio intervals and compare the results with the theoretical predictions. Both the charging voltage and the ring voltage were changed within the range of values required to produce break-up, as shown in Figure 3.6, to allow different disintegration conditions. Eleven different combinations of the charging voltage and the ring voltage were selected for performing the tests to cover different number of siblings and a wide range of initial drop sizes between 100 μm to 350 μm diameter. In choosing those conditions, the time between two consecutive drips was restricted to be longer than 3 sec. This restriction was the practical limit required to ensure individual collection of drops.

The samples at each voltage combination were collected on w.s.p. The oscilloscope trace was simultaneously stored and examined to count the number of siblings ejected from the initial drop and to verify the collected sample. If any difference in droplet number showed up, the faulty sample was rejected. After the collection process, the individual sibling diameters and the residual diameter, for each sample, were measured using a microscope of 80X magnification and then the sibling mass ratio was calculated.

3.5 Rejection of Samples

Of a total of 144 experimental samples collected, 34 samples were rejected for the following reasons:

A- No Breakup (9 Samples)

In this case the drop was below its stability limit or the sample was collected before the breakup. Those samples were rejected because no measurements of sibling mass ratio existed.

B- Error in Collection (8 Samples)

In this case the number of collected siblings was different from (less than) the observed number given by the oscilloscope which gave an indication that some siblings were lost during the collection process or two droplets were collected on top of each other.

C- Rejection of Outliers (7 samples)

The samples which exhibited very large deviation from the main stream results were considered outliers. These outliers were rejected because they did not provide representative samples. This discarding is based on the assumption that the rejected samples came from another population different to what was being tested due to the unpredictable variation in the experimental conditions [31]. It is important to note here that at least 95% of the population samples were considered representative ones. The rejected samples were determined from the results of the nozzle characteristic tests at different conditions. The detailed tables of the results of the preliminary tests and outlier cases are listed in Appendix II.

D- Misleading Samples (10 Samples)

In some cases the nozzle emitted an aerosol of a limited number of droplets and then stopped. This phenomenon has also been observed by other investigators [32,33]. Although in such conditions the Faraday cage, uncovered by any w.s.p. or oil dish, showed the same signals as that of the breakup case, the ring signal shows a completely different shape. The oscilloscope photographs,

Plate 2 Samples of the Oscilloscope Output for Breakup and Aerosol Conditions.

(A) Breakup. (B) Aerosol.

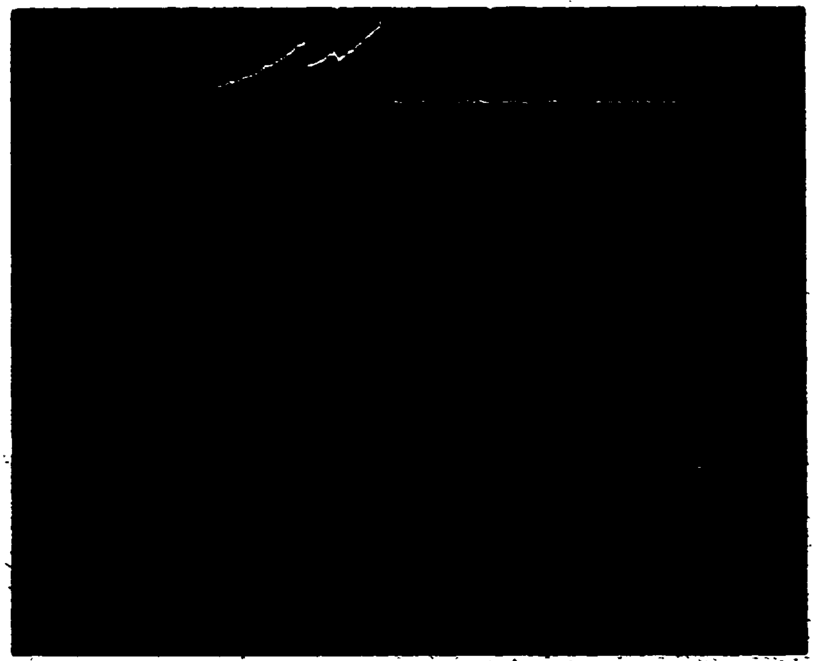

Plate 2, show the difference between the two cases.

3.6 Existing Errors

Although many attempts were made to eliminate the errors in this experiment, some sources of error could not be removed such as:

A- The time dependent variation in the charging voltage due to ripples was measured as ±5V on the Fluke meter reading. Theoretically this variation does not change the number of siblings at each of the sibling mass ratio intervals but it may cause some vibrations on the drop while it is attached to the nozzle. This might force the drop toward further disintegrations.

B- Unpredictable space charge and external acoustic noise near the nozzle which may change the level of the external forces.

C- The error in measuring the normal droplet diameters, of about 50 um, using the graticule of the microscope with 80X magnification (±5 µm resolution based on half a division) was in the range of ±10% while the error in measuring the large drops, 200 µm or larger, was less than ±2.5%. This error can be translated to an error of about ±30% in calculating the mass of the normal droplets and about ±7.5% for the large drops. For droplets smaller than 50 um (small siblings), the error in measuring their mass may be considerably higher (±100% for 16 um droplets). This error may dramatically affect the sibling mass ratios especially at the transition between their intervals .

Although using the average spreading factor of the w.s.p. was another source of error in calculating the drop mass (± 8%), it offered an extra magnification of 2.25. This magnification in turn reduced the total measuring error of the drop mass for a normal drop (50 um) from ±30% to about ±21%, while for 16 um drop, the total measuring error reduced from ±100% to ±53%. For sample error calculation, see Appendix III.

D- Capturing the drop before its final stable condition could be one of the existing errors although the preliminary tests showed that no further breakups were detected inside the Faraday cage. For such a sample in which an oval shape of a drop appeared, the average diameter was calculated and the drop was counted as a single drop.

3.7 Results

Plate 3 shows some typical magnified collected samples. In each of these photographs a relatively large drop, the residual drop, can be observed. One or more smaller droplets, siblings, are in most cases distributed to one side of the residual drop. These photographs also show that all the breakups were asymmetric as none of the samples showed a disruption of the initial drop to n identical drops. This phenomenon supports the assumption of a tree like disintegration used in the theoretical study.

Although in a few photographs the distance between the residual drop and some of the siblings was very small in comparison with the drop size, this does not contradict the catenary assumption which was used in calculating the breakup distance. This is because the distance on the w.s.p. represents only the horizontal component of the real distance there could in fact have been considerably more vertical displacement.

Plate 4 shows two oscilloscope photographs representing some of the signals detected which were used to count the number of siblings and to verify their number collected on w.s.p. It also shows how these signals were interpreted. In these photographs (as $I = dQ/dt = dQ/ds * ds/dt$), the

Microscope Magnification
For Indivadual Samples

16.0	12.8	6.4	6.4
12.8	6.4	16.0	12.8
12.8	12.8	12.8	12.8
6.4	6.4	6.4	12.8

Note: A spreading factor of 2.25 should be used for estimating the drop size.

Plate 3 Samples of Magnified Collected Droplets.
(Contact Prints)

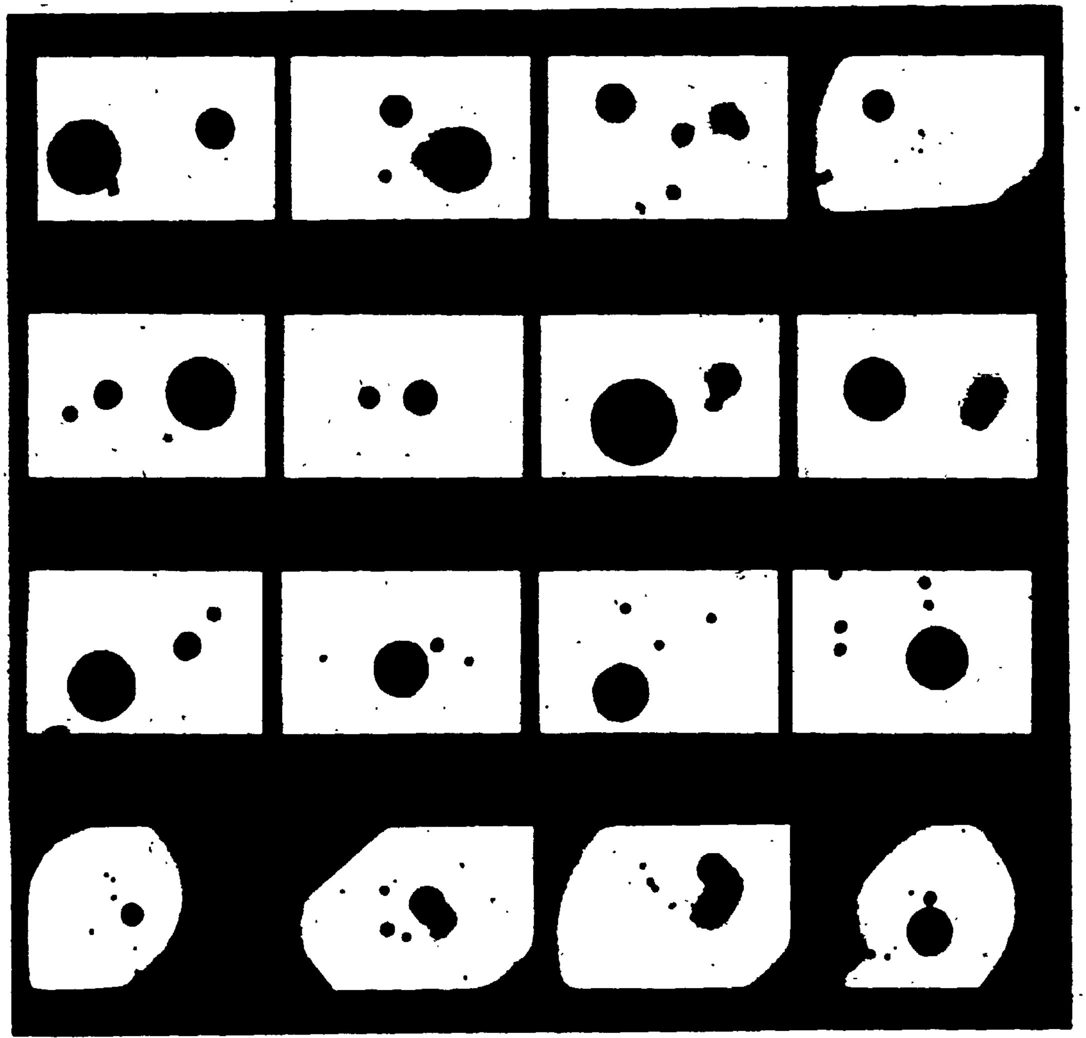

Plate 4 Samples of the Oscilloscope Outputs Used in Counting the Number of Siblings.

(1) 3 Siblings. (2) 5 Siblings.

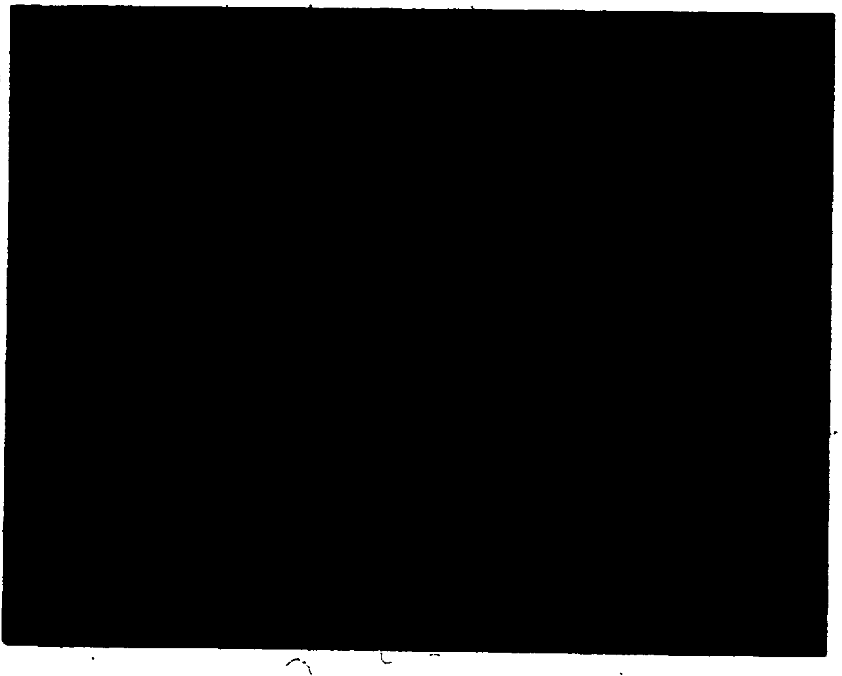

rise in the first section of the trace, denoted by A, represents the increase in the drop velocity. With increasing distance between the drop and the ring, the number of flux lines that terminate at the ring decrease as the drop reaches its terminal velocity so that the detected current decreases (section B). If any disintegration occurs (denoted by numbers), the repulsion force between the droplets tends to increase the velocity and in turn a sudden rise in the current is detected superimposed on the current decay.

Figure 3.7 presents four histograms showing the distributions of experimental results of the number of siblings for different sibling mass ratios. The results of the analysis of these distributions are summarised in Table 3.1. It is clear that the mode of each distribution always satisfies the theoretical prediction of number of siblings. Table 3.1 also shows that more than 80% of the collected samples verify the theoretical estimate of the number of siblings for the sibling mass ratios covering the range between 5% to 50%. For the sibling mass ratios between 1% and 5%, this percentage agreement with the theory dropped to approximately 60%. Such a drop in the agreement with the theory is not unexpected due to the theoretical assumption that the external forces affect the minimum energy condition only for the primary and not the secondary breakup. It can

Figure 3.7 The Distributions of the Number of Siblings for Different Sibling Mass Ratios.

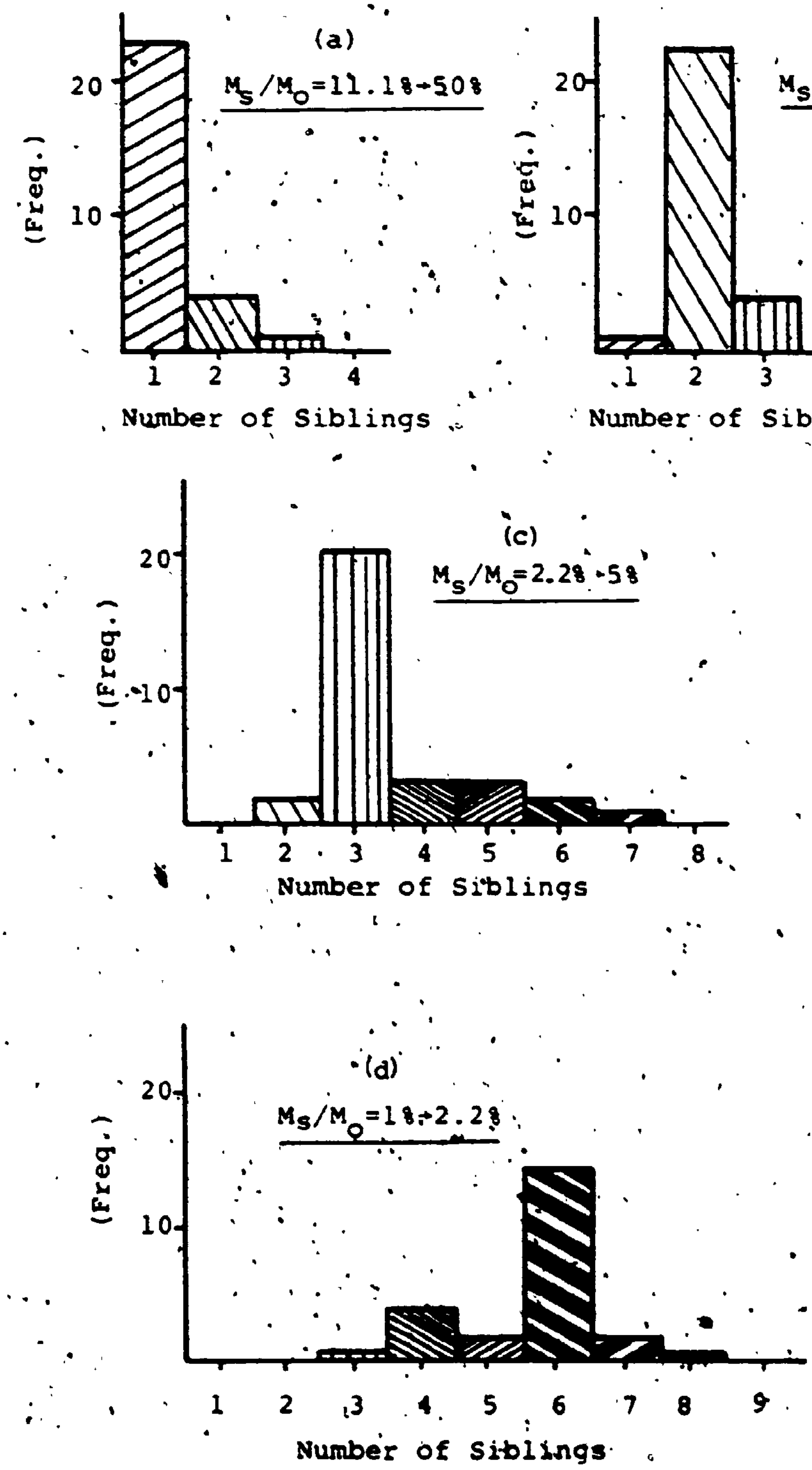
(a)
M_s/M_o=11.1%÷50%
(Freq.)
20
10
1
2
3
4
Number of Siblings
(b)
M_s/M_o=5%÷11.1%
(Freq.)
20
10
1
2
3
4
Number of Siblings
(c)
M_s/M_o=2.2%÷5%
(Freq.)
20
10
1
2
3
4
5
6
7
8
Number of Siblings
(d)
M_s/M_o=1%÷2.2%
(Freq.)
20
10
1
2
3
4
5
6
7
8
9
Number of Siblings

Table 3.1

Summary of the Experimental Results

Sibling Mass Ratio	Number of Samples	Theoretical Prediction for Number of Siblings (See Fig. 2.9)	Distribution of the Number of Siblings								Percentage Agreement with Theory
			1	2	3	4	5	6	7	8	
11.1-50.0 %	28	1	23	4	1	--	--	--	--	-	82%
5.0-11.1 %	27	2	1	22	4	--	-	--	--	-	81%
2.0- 5.0 %	31	3	-	2	20	3	3	2	1	--	65%
1.0- 2.0 %	24	6	--	--	1	4	2	14	2	1	58%

also be related to the error in measuring the droplet mass due to the small sibling sizes in the lower ranges of the sibling mass ratio (Section 3.6.C).

Figure 3.8 presents the experimental results of the number of siblings collected in the breakup test as a function of the sibling mass ratio as well as the results of the theoretical prediction given in Chapter 2. It is clear that the experimental results show good agreement with the theoretical prediction specially in the high ranges of the sibling mass ratios. This figure also presents the calculated maximum error in measuring the sibling mass ratios for some of the collected samples (a sample calculation is given in Appendix III). It shows that as the sibling mass ratio decreases, the maximum error increases. This is because for low sibling mass ratios, the siblings become very small and in turn the error in measuring their masses increases. For some of the samples, which did not satisfy the theoretical predictions, the calculated maximum error was higher than the error for those samples that match the predictions. Although the theoretical analysis predicts no breakup which yields 4, 5, 7 or 8 siblings, in some samples these numbers were observed. This may be due to capturing the drops before their final stability or due to the effect of the external forces on the secondary breakup which may lead to more disintegrations.

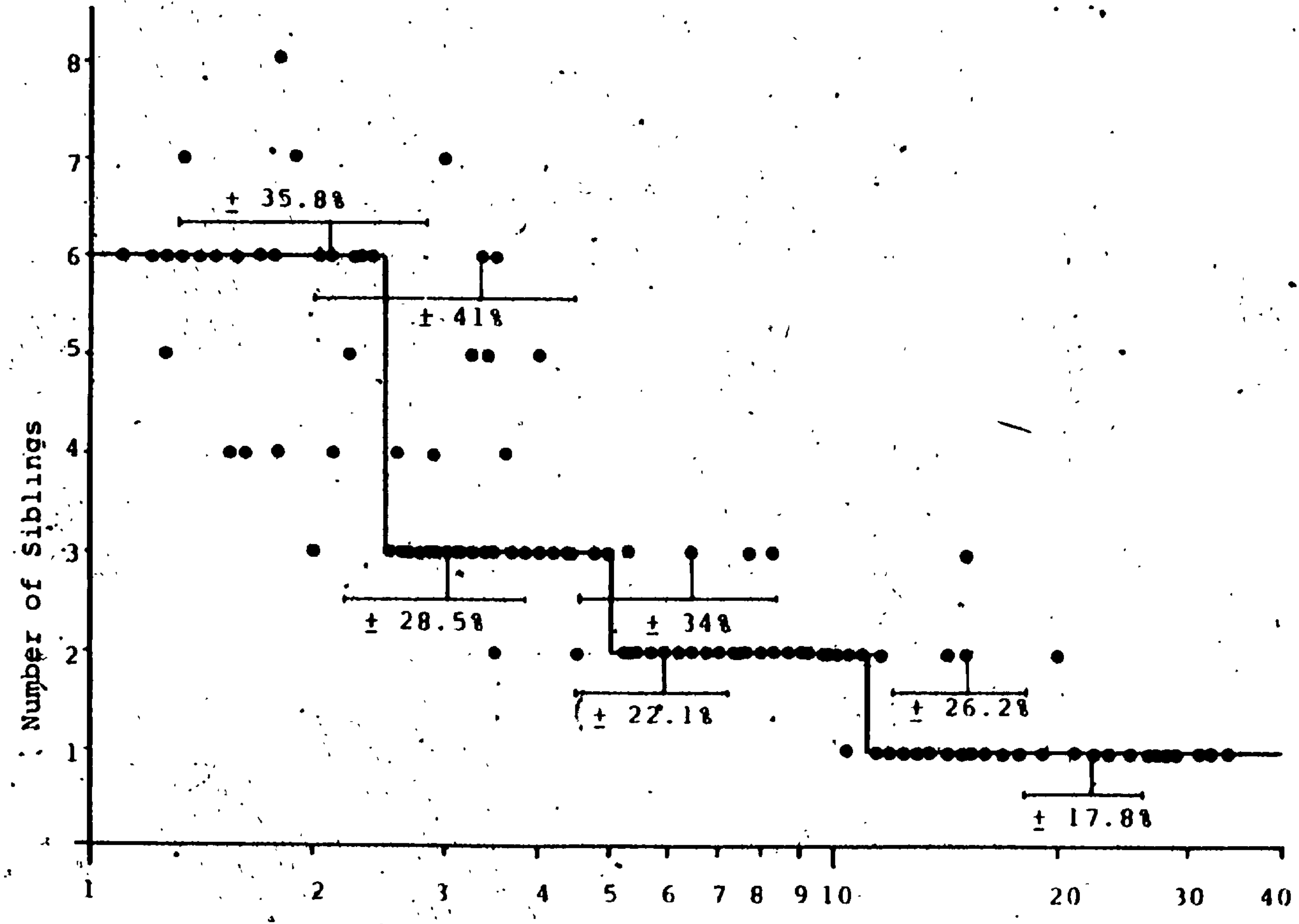

Figure 3.8 The Experimental Results of the Number of Siblings at Different Sibling Mass Ratios.

Figure 3.9 presents the calculated percentage difference between the final energy and the minimum energy of the single sibling case as a function of the sibling mass ratio. When the initial drop disintegrates at a sibling mass ratio different than that at which the minimum energy occurs, the energy difference dissipates as an effect of the external forces. For the sibling mass ratios larger than 5%, that energy difference is less than 2% of the initial energy, while it is about 6% of the initial energy at the sibling mass ratio of 1%. For the sibling mass ratios less than that, the energy difference increases sharply.

Due to the extremely small sibling sizes to be measured, there are no experimental observations for the sibling mass ratios less than 1%. However, it is expected that the error in matching the theory would be much higher. This limits the use of the theoretical prediction of the number of sibling to cover the range of sibling mass ratios between 1% and 50%. This range is quite wide for most of the electrostatic applications where the charge of the drop can be considered the main force driving the breakup process. For any application in which any other force is dominant, clearly the Rayleigh limit equation must be modified before being used in the analysis of Chapter 2.

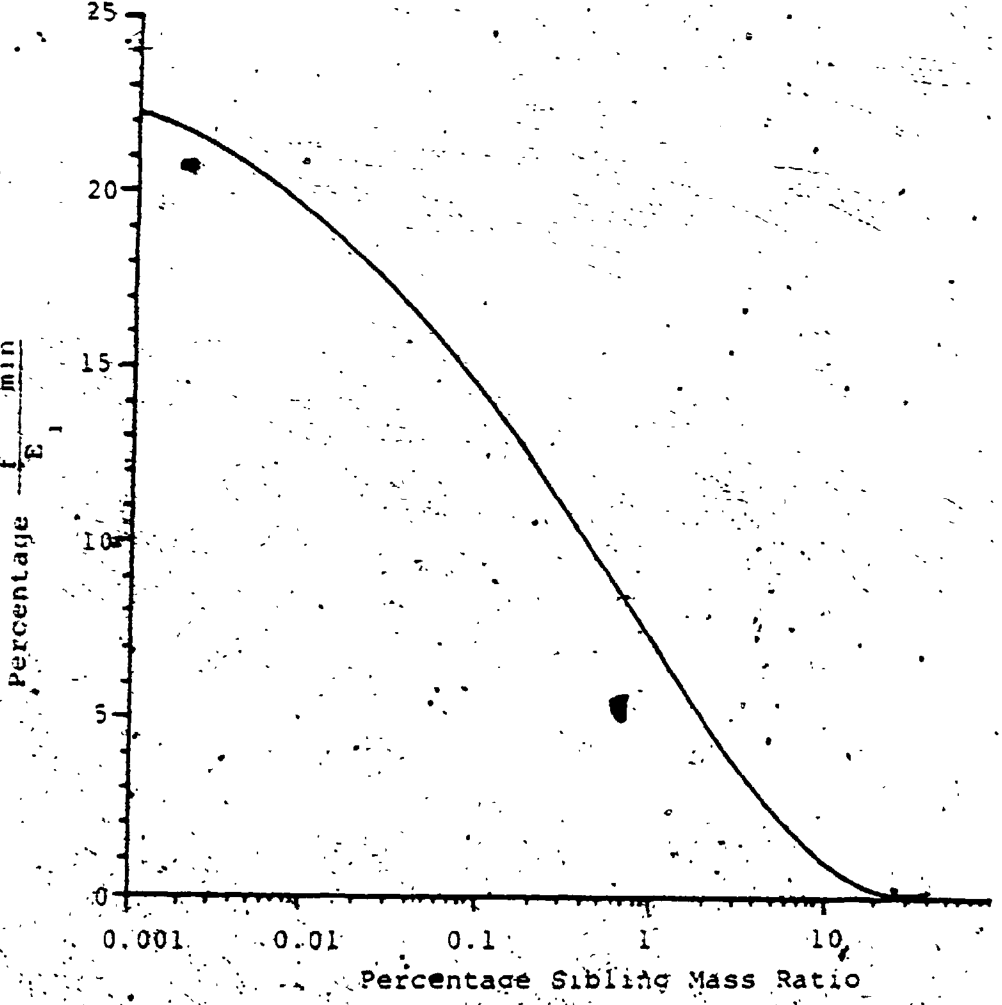

Figure 3.9 The Percentage Difference Between the Final Energy and the Minimum Energy to the Initial Energy as a Function of the Sibling Mass Ratio

CHAPTER FOUR

FORCES AFFECTING THE DROP INSTABILITY-

Review of Previous Work

4.1 Introduction

Although the Rayleigh limit is widely used to calculate the maximum charge of a drop, it is believed that the other external forces may change the charge limit dramatically. In the previous chapters, the effect of the external forces on the breakup behaviour of a charged drop was introduced. In this chapter, the most common forces acting on the drop's instability are discussed through a literature review.

4.2 Surface Tension and Drop Shape

The only reason that a liquid drop can exist at all as a mechanically stable system is that surface forces at the liquid-air interface continually try to minimize the total system energy by minimizing the interfacial area. When this effect of surface tension acts alone, the drop retains a shape characterized by a minimum surface to volume ratio, i.e. a sphere. When, however, factors other than surface energy contribute significantly to the total energy of the drop, the condition of minimum total energy may become inconsistent with a perfectly spherical shape. In the last two decades many theoretical and experimental studies have been carried out to investigate the effect of the aerodynamic forces and electrostatic forces on the drop shape [34-40]. The results show that the drop, under the effect of these forces, deforms and takes either a prolate or an oblate spheroidal shape* which is dependent on the distribution of these forces on the drop surface. The effect of each individual force on the drop shape is discussed later in this chapter.

As a consequence of the net inward attraction exerted on the surface molecules by those molecules lying deeper within the drop, the surface tension of the liquid produces an increased pressure within the drop over and above that prevailing in the air outside. This increment in pressure ΔP_s at a given point on the drop surface is expressed by the following general form [41],

---

* The prolate spheroid is a special case of the ellipsoidal shape ($\frac{X^2}{a^2} + \frac{Y^2}{b^2} + \frac{Z^2}{c^2} = 1$), where the two smallest axes are equal, i.e. $a > b = c$, while the oblate spheroid is also an ellipsoidal shape where the two larger axes are equal, i.e. $a = c > b$.

$$\Delta P_s = \gamma\,(1/R_{c1} + 1/R_{c2}) \qquad 4.1$$

where γ is the surface tension of the liquid-air interface, and R_{c1}, R_{c2} are the principal radii of surface curvature at the point in question. In the special case of a spherical drop, $R_{c1} = R_{c2} = R$, where R is the drop radius,

$$\Delta P_s\ (\text{sphere}) = 2\gamma/R \qquad 4.2$$

In the case of a deformed drop, the principal radii of curvature at a certain point on the drop surface should be calculated and Equation 4.1 should be used.

4.3 Internal Hydrostatic Pressure

This type of pressure exists within the drop due to the vertical pressure gradient in the surrounding gravitational field. For liquid drops, the difference in the hydrostatic pressure between the top and the bottom of a drop becomes quite important in controlling the drop shape. The hydrostatic pressure at any point in the drop (P_h) can be written as

$$P_h = \rho_\ell\, g h \qquad 4.3$$

where ρ_ℓ is the liquid density, g is the gravitational acceleration and h is the head of liquid above this point.

Assuming a hypothetical case in which the only external force acting on the drop is the hydrostatic force, one should expect some deformation of the drop shape. This deformation takes the form of an elongation in the direction of the gravitational field which can be approximated by a prolate spheroid [34,36]. The deformation (D), which is equal to the aspect ratio (a/b) of the semi-major to the semi-minor axes, is a function of the drop size, the liquid surface tension and its density. Clearly, in real life, other forces such as the aerodynamic forces will exist. Under such conditions, the drop may take a different shape which can be approximated by either an oblate or a prolate spheroidal shape [38-40]. The effect of different combinations of the external forces acting on the drop stability will be discussed in Chapter 6.

4.4 Electrical Charge

The stability of a charged drop in the absence of any external force was discussed in Chapter 1. Ailam and Gallily [42] concluded that since no directionality is imposed upon the problem, the equilibrium shape of the drop must remain spherical and that disintegration occurs when the charge on the drop exceeds the value given by Equation 1.1. They also revealed that there is one prolate and one oblate spheroid shape that satisfies the minimum energy for each value of $Q > Q_{R.L}$. Taylor [12] examined the effect of the drop deformation (D) on the charge limit. He approximated the drop geometry as a prolate spheroid and solved the equations of pressure equilibrium at the pole and the equator. His set of equations for the maximum charge of a deformed drop (Q_d) can be combined to form the equation :

$$Q_d = \frac{Q_{R.L}}{\sqrt{2}}\left[\frac{2-\alpha^{3/2}-\alpha^{1/2}}{1-\alpha}\right]^{1/2} \tag{4.4}$$

Where $\alpha = (1/D)^2$

The result of the maximum charge for a deformed drop with respect to the drop deformation is shown in Figure 4.1. It shows that drop deformation reduces the charge required for drop disruption. This also indicates that a spherical drop undergoing a Rayleigh instability disruption cannot achieve an equilibrium shape by deformation since less charge is needed to disrupt the distorted drop. This result proved that the shapes of minimum energy reported by Ailam and Gallily, for higher charge than the Rayleigh limit, are theoretical shapes and cannot be reached practically.

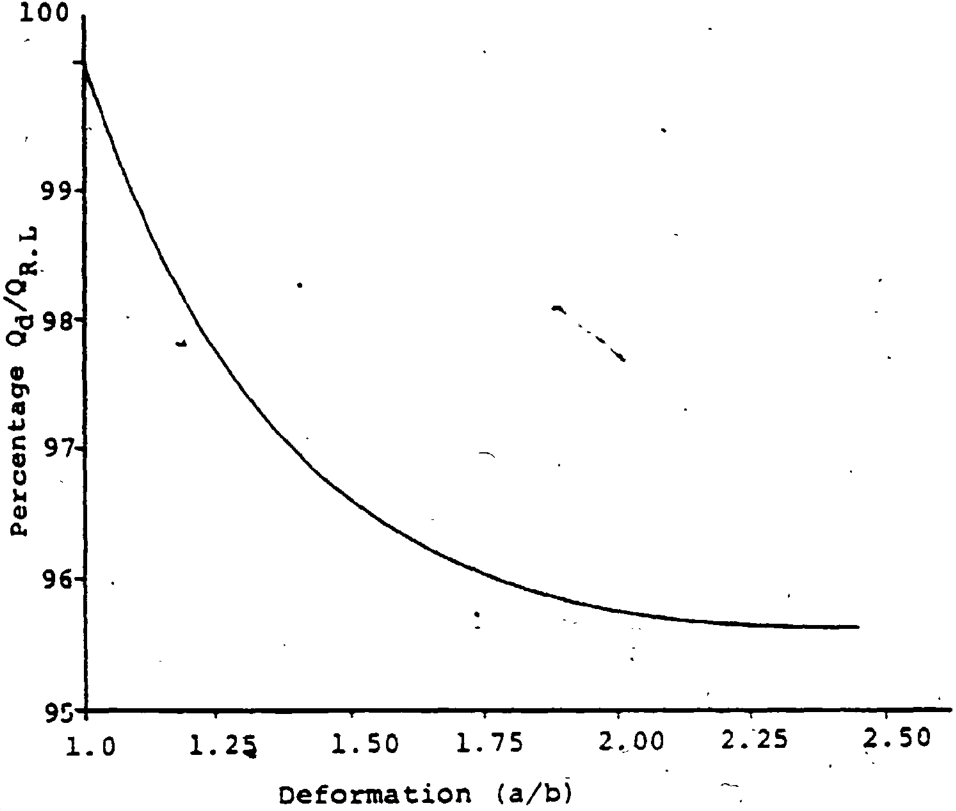

Figure 4.1 The Effect of the Drop Deformation on the Drop Charge

4.5 Electrical Field

The behaviour of water drops in a strong electric field is of interest to meteorologists because it could throw light on processes occurring in thunderclouds. Therefore, the deformation and disruption of liquid drops in an electric field has formed the subject of a number of experimental and theoretical research projects. In 1915 Zeleny [43] attempted to adapt Rayleigh's criterion for the stability of a charged drop to the poles of spheroidal drops in electric fields. Although Zeleny's criterion for the instability of such drops was shown by Taylor [12] to be incorrect, Zeleny did demonstrate in a later paper [44] that disintegration of these drops was a result of hydrodynamic instability. A very complete experimental study of the behavior of freely falling water drops in both vertical and horizontal electric fields was introduced by Macky [45]. He noted that drops in electric fields tend to elongate in the direction of the field and that the deformation of the drops increases with increasing fields. At a certain field, dependent on the drop size, the elongated drop becomes unstable and drop disruption occurs. Macky also introduced an approximate empirical relation

$$E\left(\frac{R}{\nu}\right)^{1/2} = 1.6 \qquad 4.5.a$$

relating the external field E expressed in electrostatic units, required to disintegrate a drop of undistorted radius R and surface tension ν. In MKS units this relation can be written in the form

$$E\left(\frac{R}{\nu}\right)^{1/2} = \frac{0.45}{\varepsilon^{\frac{1}{2}}} \qquad 4.5.b$$

In a theoretical and experimental study, the effect of the electric field on the elongation of both conducting and nonconducting droplets was examined by Garton and Krasucki [46]. They showed experimentally that as the field strength increased, conducting drops and also nonconducting ones, for which the permittivity of the drops exceeded twenty times the permittivity of the medium, elongated until a critical shape leading to disruption was reached. For these drops, the critical shape corresponded to a prolate spheroid of a deformation D of 1.85. For drops of permittivity ratio lower than 20 they predicted no critical shape i.e. the axial ratio increases indefinitely with an increase of the field strength.

In 1964 Taylor [12] treated the problem theoretically by assuming that the drop retained a spheroidal shape until it reached the instability point and that the equations of equilibrium between the normal stresses due to surface tension and electric field were satisfied at the pole and equator. In MKS units his equation for the drop deformation corresponds to a certain electric field and can be expressed in the form

$$E \left(\frac{R}{\nu}\right)^{\frac{1}{2}} \approx \left(\frac{2}{\varepsilon}\right)^{\frac{1}{2}} I_1 M(\alpha) \qquad 4.6$$

where

$$M(\alpha) = \alpha^{2/3} \left[2-\alpha^{3/2}-\alpha^{\frac{1}{2}}\right]^{1/2}$$

and

$$I_1 = \frac{1}{2e^3} \ln \frac{1+e}{1-e} - \frac{1}{e^2}$$

and e is the ellipticity of the spheroid $= (1-\alpha)^{\frac{1}{2}}$

The deformation of water drops of different sizes as a function of the electric field is shown in Figure 4.2. It can be seen that a critical maximum value of the electric field exists for each drop size. Taylor showed that the equilibrium configurations corresponding to points on the rising part of the curve are stable while those corresponding with values of deformation greater than 1.9 are unstable. He then concluded that the onset of instability occurs when

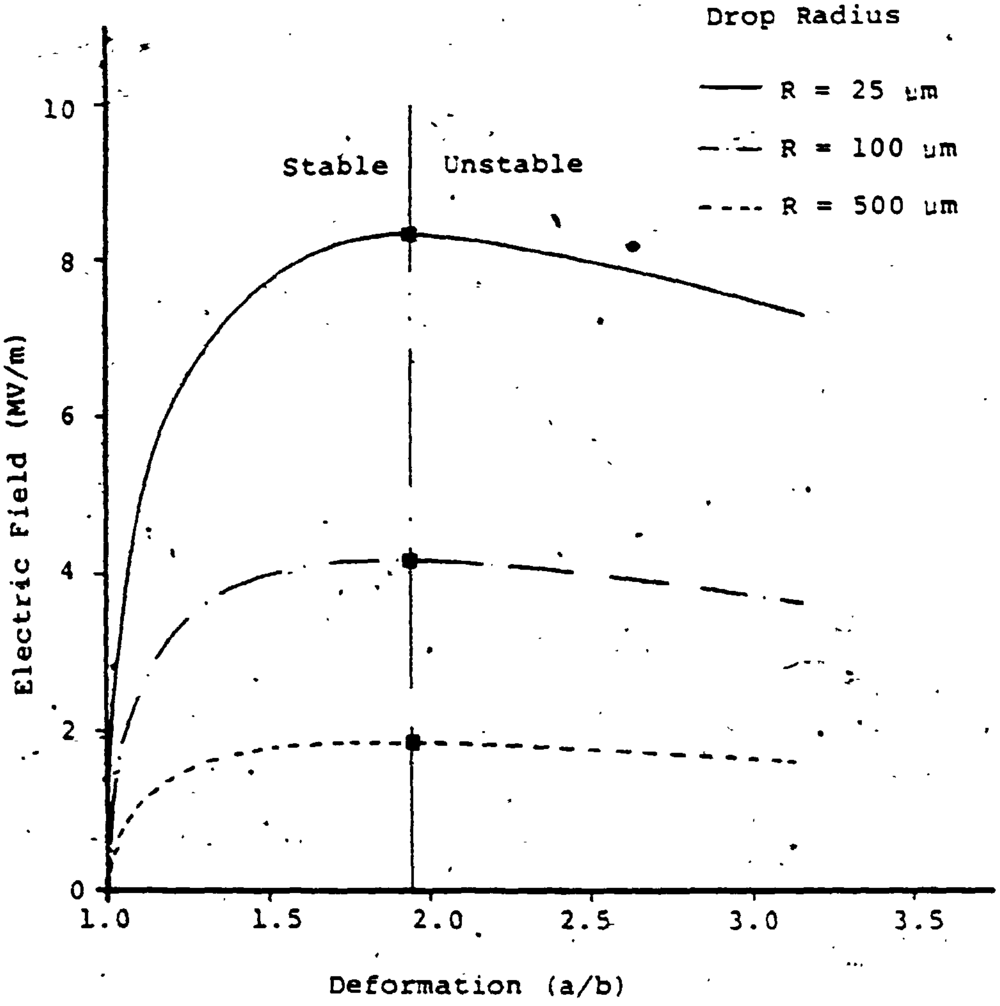

Figure 4.2 Taylor's Expression for an Uncharged Drop in a Uniform Electric Field Indicating the Maximum Drop Deformation

$$E\left(\frac{R}{\nu}\right)^{\frac{1}{2}} = 1.625 \quad \text{(e.s.u.)}$$

$$= \frac{0.458}{\varepsilon^{\frac{1}{2}}} \quad \text{(MKS)} \qquad 4.7$$

and

$$D_{max} = 1.9$$

which shows good agreement with Equation 4.5.b. This criterion for water drops was confirmed by an intensive experimental study carried out by Matthews [34].

Taylor also concluded that when the drop becomes unstable the ends develop obtuse-angled conical points from which axial jets are projected. It was shown theoretically that the conical interface between two fluids can exist only in equilibrium in an electric field when the cone has a semi-vertical angle of 49.3°. In a more recent work, Miksis [37] showed theoretically that when the dielectric constant of the liquid is larger than a certain critical value ($\varepsilon_c \simeq 20$), the drop develops two conical points at its ends for a certain field strength. For $\varepsilon < \varepsilon_c$, the drop elongates and retains its original nearly prolate spheroidal shape, without developing any conical points as the field is increased.

The behaviour of the drop past its stability limit, for a combination of forces acting against its surface tension, will not be discussed in this part of the study.

Considering that the electrical force due to charge is the most effective force acting on the drop, it is assumed that the behaviour is the same as that for a charged drop giving multi-sibling droplets as in Chapter 2. Also in the course of the next sections the drop is assumed to be conductive as this condition covers many of the electrostatic applications involving liquid drops.

4.6 Aerodynamic Force

It is well known from experimental observations that liquid drops falling at their terminal velocity (V_T) in another fluid are hydrodynamically unstable and breakup if they are larger than a certain critical size [47-48]. Using a pressure balance equation estimated from a modified aerodynamic pressure distribution around a sphere assuming potential flow, i.e. ideal flow with viscosity effect, Pruppacher and Pitter [40] predicted the shape of water drops falling at their terminal velocity in air. They reported that drops with radii < 170 µm. were very slightly deformed and could be considered spherical while drops between 170 and 500 µm. could be closely approximated by an oblate spheroid. For drops having radii greater than 500 µm. they noted that asymmetric oblate spheroids with increasingly pronounced flat bases developing concave depressions were obtained.

In order to find a criterion for instability, Pruppacher et al assumed plane parallel waves, corresponding to the hydrodynamic model of two superimposed inviscid fluids of infinite extent. In such a model, instability would occur if the wave length (λ) of the disturbance is greater than a critical value (λ_c) of 1.71 cm [49]. From this model they estimated the critical base width for breakup to equal $\lambda_c/2$ = .855 cm. i.e. the base width was just sufficient to accomodate the fundamental standing wave corresponding to λ_c. According to their model, this base width corresponded to a spherical drop radius of about 0.45 cm.

The stability analysis of their study was refined by Klett [50]. He represented the shape of the bottom surface of the drop as a composition of two-dimensional circular waves, rather than the one-dimensional plane wave used by Pruppacher et al. As the curvature of the drop surface near the edge of the base has a constraining effect on the wave motion, he regarded the effect of the drop walls on its stability as lying between two extreme cases:

1. There were no walls as was assumed by Pruppacher et al [40] but he used a different approach to calculate the critical base width [51].

2. There were rigid vertical walls such as found in the case of two superimposed fluids contained in a vertical circular tube.

His analysis showed that the largest stable base width for a falling drop should lie between 1.0 and 1.3 cm., rather than the smaller value of 0.855 cm. predicted by Pruppacher et al.

The previous result is in agreement with the empirical formula developed by Grace et al [52] to estimate the maximum stable equivalent drop diameter given in the form:

$$d_{max} = 4\left(\frac{\gamma}{g\Delta\rho}\right)^{\frac{1}{2}} \qquad 4.8$$

where $\Delta\rho$ is the absolute value of the two fluid density difference.

The aerodynamic deformation of viscous drops caused by normal pressure forces at the surface was treated theoretically by Hinze [48] in a different manner. Assuming small deformation, he showed that breakup occurred when a critical value of the Weber Number (We) was exceeded, where We is the ratio of flow field inertia force to the drop surface tension force.

$$We = \rho_{air} V_T^2 d/\nu \qquad 4.9$$

Hinze concluded that for falling drops, the critical value of the Weber Number was ≈ 22. He also developed an equation for the maximum deformation (D_{max}) of drops of initial radius (R). This equation was also dependent on the Weber Number, i.e.

$$D_{max} = RK_z We \qquad 4.10$$

where K_z is a constant dependent on the Ohnesorge Number (Z) which is the ratio of the viscous force to the square root of the drop Weber Number:

$$Z = \frac{\mu_\ell}{(\rho_\ell \nu d)^{\frac{1}{2}}} \qquad 4.11$$

where μ_ℓ is the drop viscosity and ρ_ℓ is the drop density. From his analysis, he showed that:

$$K_z = 0.085 \quad \text{for } Z < 1$$
$$= 0.047 \quad \text{for } Z > 1 \qquad 4.12$$

CHAPTER FIVE

INSTABILITY OF LIQUID DROPS SUBJECTED TO EXTERNAL FORCES

5.1 Introduction and Assumptions

The ultimate aim of a complete study dealing with drop stability would be to predict the onset of instability of liquid drops affected by the various forces reviewed in Chapter 4, i.e. surface tension, electrical, aerodynamic and gravitational forces. In addition to these forces there are internal forces due to internal circulation and translational motion as the drop changes shape. As shown by McDonald [35] and Le Clair et al. [53], there is no difference between the drag on a water drop and that of a rigid body of the same Reynolds number as long as they have the same shape. They also showed that the internal circulation plays a negligible role in affecting the drop shape. For that reason the internal circulation is neglected in the present study. For steady state conditions the translational motion can also be neglected. In this chapter, a modified Rayleigh limit equation is derived to take into account the effect of the external forces and the drop deformation on the stability limit.

Due to the fact that some of the forces deform the drop shape to a special case of ellipsoidal shape (prolate or oblate spheroids), it is assumed that the drop retains the spheroidal shape until the onset of instability. For equilibrium shape, the pressure just inside the drop surface should be the same everywhere. Following Taylor's approach [12], we assume that the equilibrium is satisfied at the pole and the equator of the drop, namely point A and B respectively in Figure 5.1.

5.2 Analysis

The pressure (P) at any point just inside the drop surface can be determined from the relation

$$P - P_\infty = \Sigma P_{ext} = \Delta P \qquad 5.1$$

where P_∞ is the ambient pressure far from the drop, and ΣP_{ext} is the contribution of all the forces to the pressure at the point under consideration. The quantity P_{ext} can be either positive or negative. In the notation used in this study, the pressure is regarded positive if it is opposing the direction of the surface tension pressure. To solve Equation 5.1 at the pole and the equator of the drop, the expressions for each pressure due to each force acting on the drop for both the prolate and the oblate spheroids

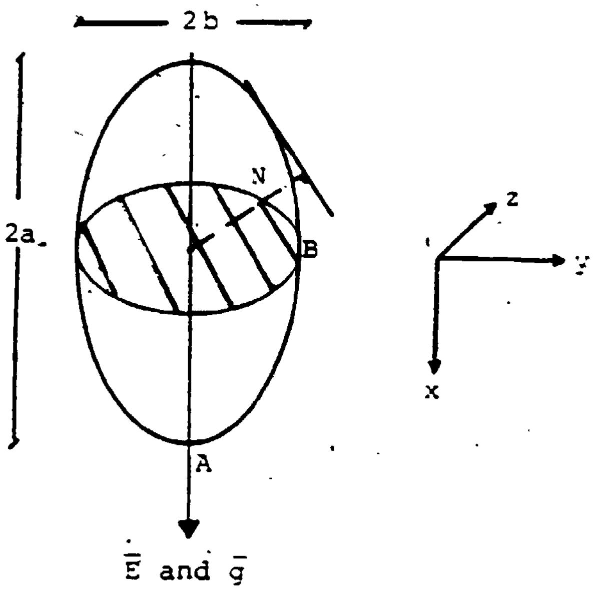

(a) Prolate Spheroid

$a > b = c$

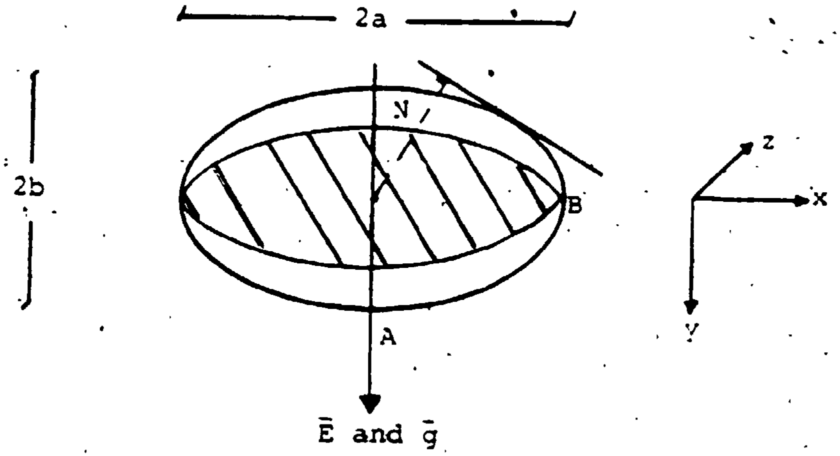

(b) Oblate Spheroid

$a = c > b$

Figure 5.1 Schematic Diagram for Drop Shape are required.

5.2.1 Surface Tension Pressure

The discontinuity of normal stress due to surface tension at any point is described by Equation 4.1. For a spheroidal shape, the analytical expressions for the principal radii of curvature can be expressed by [54]

$$R_{c1} = \frac{a^2 b^2}{N^3} \qquad 5.2.a$$

and

$$R_{c2} = \frac{c^2}{N} \qquad 5.2.b$$

where N is the perpendicular from the centre to the tangent plane at the point in question (as in Figure 5.1).

Because both the oblate and the prolate spheroids are special cases of the ellipsoidal shape, one can modify Equation 5.2.b so that for a prolate spheroid $a > b = c$; then

$$R_{c2} = \frac{b^2}{N} \qquad 5.2.c$$

while for an oblate spheroid $a = c > b$

$$R_{c2} = \frac{a^2}{N} \qquad 5.2.d$$

The surface tension pressures at points A and B respectively are:

for a prolate spheroid,

$$P_{SA} = -\frac{2a\nu}{b^2} \qquad 5.3$$

$$P_{SB} = -\nu\left(\frac{b}{a^2} + \frac{1}{b}\right)$$

while for an oblate spheroid,

$$P_{SA} = -\frac{2b\nu}{a^2} \qquad 5.4$$

$$P_{SB} = -\nu\left(\frac{a}{b^2} + \frac{1}{a}\right).$$

5.2.2 Internal Hydrostatic Pressure

From Equation 4.3 and Figure 5.1, the internal hydrostatic pressure at points A and B for both the oblate and prolate spheroids can be expressed as

$$P_{hA} = 2\ \ ga \quad \text{(prolate)} \qquad 5.5$$

$$= 2.\rho_\ell gb \quad \text{(oblate)}$$

and for both cases $P_{hB} = P_{hA}/2$.

5.2.3 Electrical Pressure

The problem involving the field of a charged conducting ellipsoid and that of an ellipsoid in a uniform electric field can be solved by the use of ellipsoidal coordinates [55-56]. For charged conducting ellipsoidal shapes, the distribution of the charge on the surface is given by

$$\sigma = \frac{QN}{4\pi\ abc} \qquad 5.6$$

where Q is the total charge on the drop. The electric field (E) can then be expressed as

$$E = \frac{\sigma}{\varepsilon} = \frac{QN}{4\pi\varepsilon\ abc} \qquad 5.7$$

The normal electric stress can then be written in the form:

$$P_{elec} = \frac{\varepsilon}{2} E^2 = \frac{Q^2 N^2}{32\pi^2 \varepsilon a^2 b^2 c^2} \qquad 5.8$$

For a prolate spheroid (c = b) and at point A, N = a. Therefore,

$$P_{elec_A} = \frac{Q^2}{32\pi^2 \varepsilon b^4}$$

and at point B, $N = b$. Therefore,

$$P_{elec_B} = \frac{Q^2}{32\pi^2 \varepsilon a^2 b^2} \qquad 5.9$$

Similarly, for an oblate spheroid $a = c$, Then Equation 5.8 gives

$$P_{elec_A} = \frac{Q^2}{32\pi^2 \varepsilon a^4}$$

and

$$P_{elec_B} = \frac{Q^2}{32\pi^2 \varepsilon a^2 b^2} \qquad 5.10$$

For an uncharged prolate spheroid in an electric field (E) parallel to the major axis in the X direction, Landau and Lifshitz [56] and Taylor [12] showed that the perturbation of the electric field along the X axis is

$$\frac{dV}{dn} = \frac{ENX}{b^2 I_1} \qquad 5.11$$

where I_1 is given by Equation 4.6. As the normal stress at any point is $\varepsilon(dV/dn)^2/2$, then for the prolate spheroid geometry given in Figure 5.1.a

$$P_{elec_A} = \frac{\varepsilon E^2 a^4}{2b^4 I_1^2}$$

and

$$P_{elec_B} = 0 \qquad 5.12$$

For an oblate spheroid where the electric field is parallel to the minor axis as in Figure 5.1.b, then

$$P_{elec_A} = \frac{\varepsilon E^2 b^4}{2a^4 I_2^2}$$

and

$$P_{elec_B} = 0 \qquad 5.13$$

where

$$I_2 = \frac{1+S^2}{S^3} (S - \tan^{-1} S)$$

and

$$S = \left(\frac{b^2}{a^2 - b^2} \right)^{-1/2}$$

If the electric field direction is perpendicular to the assumed direction, Landau and Lifshitz [56] showed that the expression for the electric pressure is the same as Equations 5.12 and 5.13 except the values of I_1 and I_2 change to $[1 - I_n]/2$ with $n = 1,2$. For any other direction of the electric field, i.e. its direction does not coincide with any of the spheroid coordinates, each of the three components of the electric field on the three coordinates should be treated separately and the superposition of the three pressures at any point could be used to calculate the total pressure.

In the case of a charged drop in an electric field, Figure 5.1, the Maxwell tensor gives the combined pressure.

For a prolate spheroid:

$$P_{elec_A} = \frac{1}{32\pi^2\varepsilon}\left(\frac{Q}{b^2} + \frac{4\pi\varepsilon a^2 E}{b^2\, I_1}\right)^2$$

and

$$P_{elec_B} = \frac{1}{32\pi^2\varepsilon}\left(\frac{Q}{ba}\right)^2 \qquad 5.14$$

while for an oblate spheroid:

$$P_{elec_A} = \frac{1}{32\pi^2\varepsilon}\left(\frac{Q}{a^2} + \frac{4\pi\varepsilon b^2 E}{a^2\, I_2}\right)^2$$

and

$$P_{elec_B} = \frac{1}{32\pi^2\varepsilon}\left(\frac{Q}{ba}\right)^2 \qquad 5.15$$

5.2.4 Aerodynamic Pressure

The study of isothermal steady laminar flow of an incompressible viscous fluid past a spheroidal drop requires the solution of the Navier-Stokes equation and the equation of continuity, subject to the prevailing boundary conditions. The Navier-Stokes equation, being non-linear, has so far proved insoluble for the problem of axisymmetric flow around oblate and prolate spheroids, except by techniques which linearize the equation of motion by approximations [57-59]. Masliyah [60] solved this equation numerically for steady incompressible flow past oblate and prolate spheroids for Reynolds numbers up to 100. The aspect ratios (b/a) of the spheroids investigated were 1, 0.9, 0.5 and 0.2. Solving for the pressure distribution and the drag coefficient, Masliyah showed that the pressure distribution of a spheroid was different than that of a sphere. From his analysis, one can approximate the aerodynamic pressure at points A and B for both prolate and oblate spheroids in the form

$$P_{aero_A} = -K_1 \rho_a V_T^2/2$$

and

$$P_{aero_B} = K_2 \rho_a V_T^2/2 \qquad 5.16$$

In Equation 5.16, ρ_a is the air density and V_T is the terminal velocity of the drop which can be calculated from Proudman and Pearson's expression given as [59]

$$V_T = \frac{QE + (4/3)\pi R^3 \rho_w g}{6\pi \mu a_e K}\left[1 + \frac{3}{16} ReK + \frac{9K^2}{160} Re^2 \ln \frac{Re}{2}\right]^{-1} \qquad 5.17$$

where a_e is the equatorial radius of the spheroid, μ is the air viscosity and

$$K = \frac{1}{(3/4)\sqrt{L^2+1}\,[L-(L^2-1)\cot^{-1}L]} \quad \text{for oblate, and}$$

$$K = \frac{1}{(3/4)\sqrt{U^2-1}\,[(U^2+1)\coth^{-1}U-U]} \quad \text{for prolate,}$$

where

$$L = \left(\frac{b^2}{a^2 - b^2} \right)^{1/2}$$

and

$$U = \left(\frac{a^2}{a^2 - b^2} \right)^{1/2} \qquad 5.18$$

In Equation 5.16, K_1 and K_2 are constants that depend on the Reynolds number, the drop shape (prolate or oblate) and the inverse of the drop deformation i.e. $1/D = (b/a)$.

For more details about the flow past spheroids, the drag calculations, differences between rigid and liquid bodies and numerical values of K_1 and K_2 see Appendix IV.

5.3 Stability Limit for a Prolate Spheroid

Solving Equation 5.1 for a prolate spheroid at points A and B gives

$$\Delta P_A = \Delta P_B$$

or

$$\rho_w g a + \frac{1}{32\pi^2\varepsilon} \left(\frac{Q}{b^2} + \frac{4\pi\varepsilon E a^2}{b^2 I_1} \right)^2 - \frac{K_1}{2} \rho_a V_T^2 - \nu \left(\frac{2a}{b^2} \right)$$

$$= \frac{1}{32\pi^2\varepsilon} \left(\frac{Q}{ba} \right)^2 + \frac{K_2}{2} \rho_a V_T^2 - \nu \left(\frac{b}{a^2} + \frac{1}{b} \right) \qquad 5.19$$

Simplifying this equation by substituting

$$\rho_w g = C_1$$

$$\frac{1}{32\pi^2 \varepsilon} = C_2$$

$$\frac{K_1 + K_2}{2} \rho_a = C_3$$

$$4\pi\varepsilon = C_4$$

Thus,

$$C_1 a + C_2 \left[\left(\frac{Q}{b^2} + \frac{E a^2 C_4}{b^2 I_1} \right)^2 - \frac{Q^2}{b^2 a^2} \right] - C_3 V_T^2 - \nu \left[\frac{2a}{b^2} - \frac{b}{a^2} - \frac{1}{b} \right] = 0 \qquad 5.20$$

Writing

$$\alpha = \frac{b^2}{a^2}$$

then

$$a = R\alpha^{-1/3} \qquad \text{and} \qquad b = R\alpha^{1/6}$$

where R is the equivalent spherical radius of the same volume. Then Equation 5.20 yields

$$C_1 R \alpha^{-1/3} + C_2 \left[\left(\frac{Q}{R^2 \alpha^{1/3}} + \frac{C_4 E}{I_1 \alpha} \right)^2 - \frac{Q^2}{R^4 \alpha^{-1/3}} \right] - C_3 V_T^2 = \frac{\nu}{R} \left[2\alpha^{-2/3} - \alpha^{5/6} - \alpha^{-1/6} \right] \qquad 5.21$$

Equation 5.21 is the general form for a prolate spheroid and can be solved numerically to check the stability of a liquid drop due to a certain combination of forces. The maximum drop deformation in such a case can also be calculated. For an uncharged drop, neglecting the hydrostatic and the aerodynamic forces, Equation 5.21 gives

$$C_2 \left(\frac{C_4 E}{\alpha I_1} \right)^2 = \frac{\nu}{R} \left[2\alpha^{-2/3} - \alpha^{5/6} - \alpha^{-1/6} \right] \qquad 5.22$$

Then

$$\left(\frac{R}{\nu} \right)^{1/2} = \left(\frac{2}{\varepsilon} \right)^{1/2} I_1 M(\alpha) \qquad 5.23$$

where

$$M^2(\alpha) = \alpha^{4/3} \left[2 - \alpha^{3/2} - \alpha^{1/2} \right]$$

Equation 5.23 is the same as that derived by Taylor [12] for an uncharged drop in a uniform electric field (Equation 4.6).

Neglecting the aerodynamic, hydrostatic and the electric field pressures, Equation 5.21 gives

$$C_2 \left[\frac{Q^2}{R^4 \alpha^{2/3}} - \frac{Q^2}{R^4 \alpha^{-1/3}} \right] = \frac{\nu}{R} \left[2\alpha^{-2/3} - \alpha^{5/6} - \alpha^{-1/6} \right] \qquad 5.24$$

Then

$$\frac{Q^2}{32\pi^2 \varepsilon \nu R^3} = \frac{2 - \alpha^{3/2} - \alpha^{1/2}}{1 - \alpha} \qquad 5.25$$

This equation is also the same as that given by Taylor [12] for the charge limit of a spheroidal drop. Using L'Hopital's rule to solve Equation 5.25 for $\alpha = 1$ leads to

$$Q^2 = 64\pi^2 \epsilon R^3 \nu$$

or

$$Q = 8\pi\sqrt{\epsilon\nu}\, R^{3/2}$$

which is the well known form of the Rayleigh stability limit for a spherical charged drop unaffected by any other external force. From the previous discussion, one can see that Equation 5.21 is the general form which defines the drop stability while the other equations (Eq. 1.1, Eq. 4.4 and Eq. 4.6) given by the previous investigators are only special cases.

5.4 Stability Limit for an Oblate Spheroid

Solving Equation 5.1 for an oblate spheroid using the same simplifications used for the prolate spheroid and writing

$$W = \frac{a^2}{b^2} = \frac{1}{\alpha},$$

then

$$a = R\, W^{1/6}$$
$$b = R\, W^{-1/3} \qquad 5.26$$

The general instability equation for the oblate spheroid reduces to

$$-C_1RW^{-1/3} + C_2\left[\left(\frac{Q}{R^2W^{1/3}} + \frac{C_4E}{WI_2}\right)^2 - \frac{Q^2}{R^4W^{-1/3}}\right] - C_3V_T^2 = \frac{\nu}{R}\left[2W^{-2/3} - W^{5/6} - W^{-1/6}\right] \tag{5.27}$$

It is clear that Equation 5.27 is in the same form as Equation 5.21, with an interchange between a and b or by defining the deformation factor (W) for an oblate spheroid equals ($1/\alpha$) of the prolate one. Using the previous definition, I_2 yields to I_1 [56] and K (oblate) yields to K (prolate) [57]. It is also easy to see that solving Equation 5.27 for a charged spherical drop unaffected by any other external force gives the Rayleigh stability equation as well.

CHAPTER SIX

NUMERICAL EVALUATION OF THE INSTABILITY OF LIQUID DROPS

6.1. Intrdduction

In the previous chapter, general equations describing the drop stability were introduced (Eq. 5.21 and Eq.5.27). These equations show that for a certain surface tension of the liquid (υ) and drop equivalent radius (R) of the same volume, many possibilities of external force combinations and drop deformations may lead to the instability condition. For known external forces acting on a charged drop and for certain surface tension, there is only one deformation which satisfies the drop equilibrium. By placing more charge on the drop surface, further deformation takes place until a new final equilibrium deformation is achieved. In some cases, the solution satisfying the stability equilibrium occurs at drop deformation (a/b) greater than 10. In such a case, the drop is considered to be unstable since breakup may be expected due to the jet action [62]. In this chapter, a technique based upon superposition is used to study the effect of each of the external forces on the drop instability. A hypothetical case of only the hydrostatic force affecting a charged drop instability is evaluated in

Section 6.2.1. This case is followed by the combination of both hydrostatic and electrical field forces in Section 6.2.2. The general case is then evaluated in Section 6.2.3.

In the present study Equations 5.21 and 5.27 are solved numerically for selected values of the drop equivalent radius, the liquid surface tension and preset external force conditions. An iteration process based on the pattern search optimization technique is used to calculate the charge of a drop, Q_d, for each value of different preset drop deformations. The results are then evaluated to determine the maximum charge value (the charge limit $Q_{s.L}$) and the corresponding maximum allowed drop deformation.

To select numerically between Eq. 5.21 and Eq 5.27, the aerodynamic pressure is compared with the sum of the electrical and the hydrostatic pressures. For the case in which the aerodynamic pressure is less, the drop is assumed to retain a prolate spheroidal shape with a deformation $D > 1$. On the other hand for an aerodynamic pressure larger than the sum of the other pressures, the drop is assumed to have an oblate spheroidal shape with $D < 1$.

6.2 Numerical Results of the Instability of Charged Drops

6.2.1 Instability Due to Hydrostatic Pressure

Consider a hypothetical condition of zero external electric field and the charged drop moving very slowly so that its terminal velocity is approximately zero. For such conditions, one can assume that the only external forces acting on the drop are the electrostatic repulsion force and the hydrostatic force. The drop will possess a certain deformation and its shape can be approximated by a prolate spheroid. Solving Equation 5.21 for a charged water drop (ν = 72.75 mN/m), of a certain equivalent spherical radius (R), the charge (Q_d) of the drop for different values of drop deformation can be calculated.

Figure 6.1 presents the effect of the hydrostatic pressure on the charge Q_d of a deformed water drop of 100 um equivalent radius. It displays the percentage ratio of the charge Q_d to the Rayleigh limit charge as a function of the drop deformation calculated by Equation 5.21. It also displays the values obtained by Taylor's expression for zero hydrostatic pressure, Eq. 4.4. Figure 6.1 shows that the hydrostatic pressure reduces the allowable charge on the drop. It also shows that the charge Q_d has a maximum value $Q_{s.L}$ equal to 99.1% of the drop Rayleigh limit which

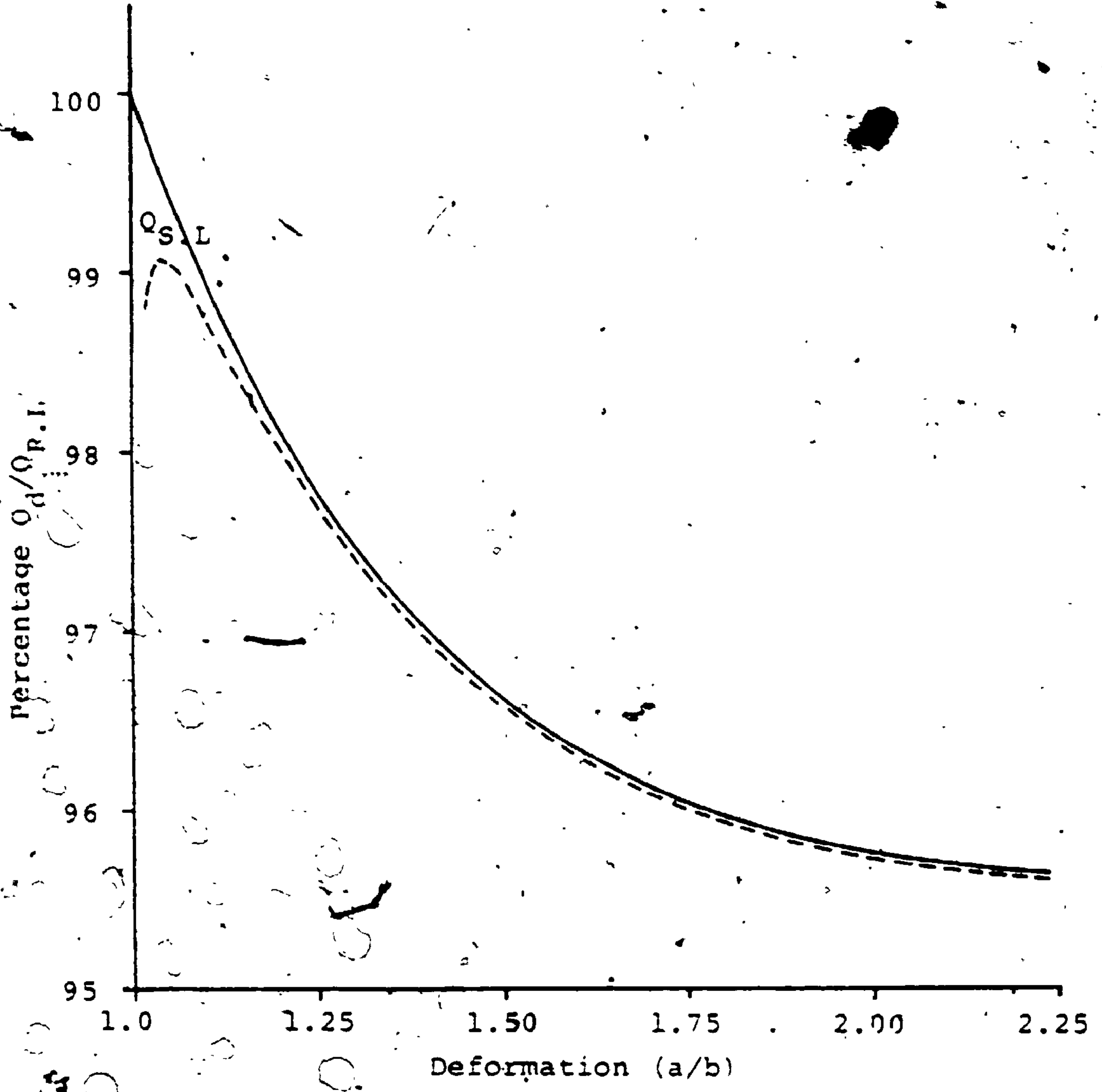

Figure 6.1 The Effect of the Drop Elongation on the Drop Charge for Equivalent Radius = 100 μm

corresponds to a deformation of about 1.04. Since less charge than this value is needed to achieve an equilibrium shape for drop deformation larger than 1.04, and since no charge sink is assumed, one can set a charge limit for this drop equal to $Q_{s.L}$. For drop charges less than this limit, the drop will retain a stable spheroidal shape with aspect ratio (deformation) less than 1.04.

Figure 6.2 presents the effect of the drop equivalent radius on the drop behaviour for very small deformations. It shows that, for each drop size and for zero electrical charge, the drop has a certain initial deformation due to the hydrostatic force. For all the values less than the initial deformation, no solution for Eq. 5.21 exists and in turn the drop will only achieve equilibrium by further deformation until the drop reaches its required initial deformation. Figure 6.2 also shows that the smaller the drop size, the closer the initial deformation to unity (i.e. spherical shape).

The variation of the maximum charge limit with the drop size is given in Figure 6.3 which presents the percentage ratio of the charge limit of a water drop to its Rayleigh limit charge as a function of the equivalent drop radius. It shows that the ratio of the charge limit to the drop Rayleigh limit decreases linearly to about 96.2% for a water

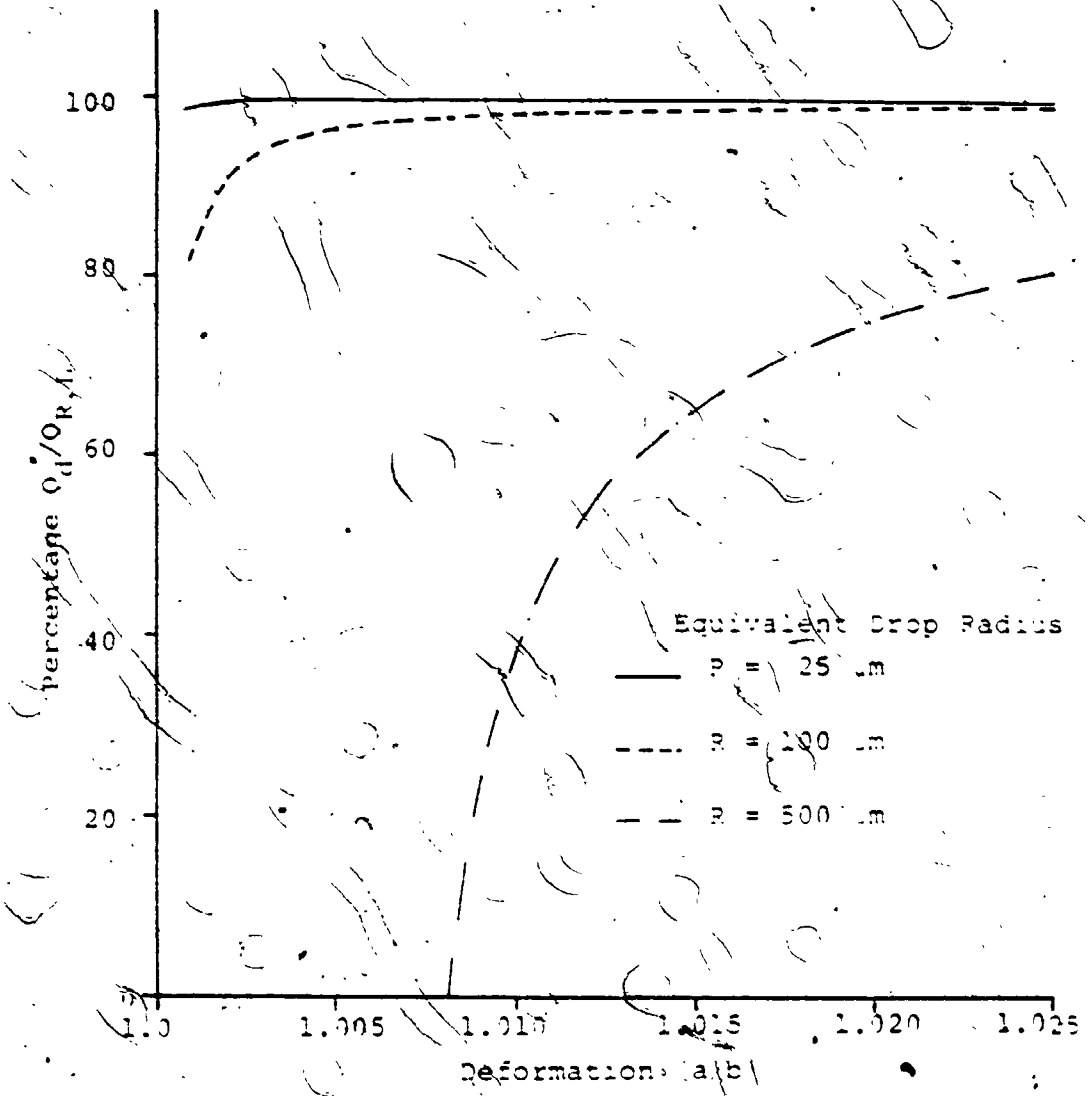

Figure 6.2 The Effect of the Drop Deformation on the Drop Charge Due to the Hydrostatic Force for Different Drop Sizes

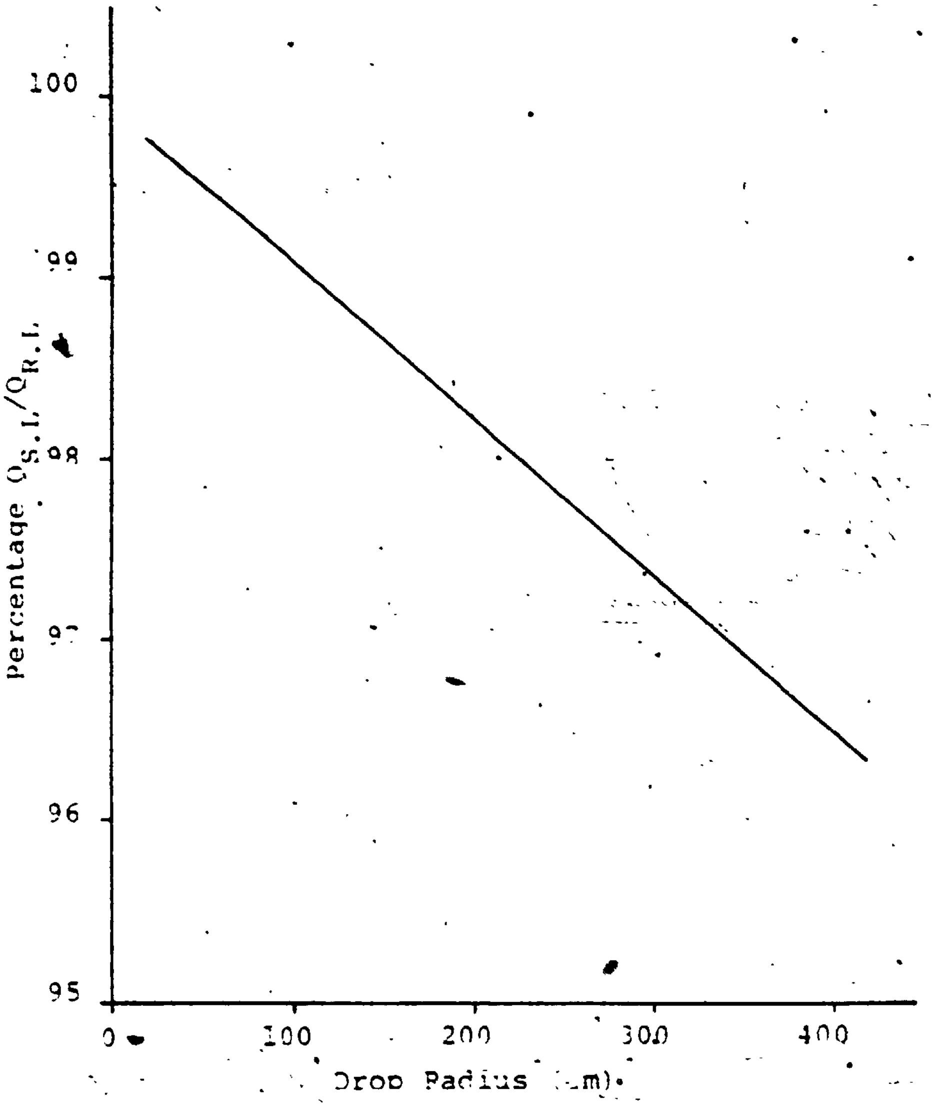

Figure 6.3 The Ratio of the Charge Limit of a Stable Drop to its Rayleigh Limit Charge as a Function of the Drop Size Due to the Hydrostatic Pressure

drop of 400 µm. For very small drops, the effect of the hydrostatic force tends to diminish and the drop charge limit becomes very close to the Rayleigh limit charge. The effect of the drop size on the maximum stable deformation corresponding to the charge limit is given in Figure 6.4. It shows that the larger the drop size, the larger the maximum drop deformation. It also shows that the increase of the maximum drop deformation is not linear with respect to the drop size. This phenomenon can be explained by investigating the pressure components affecting the drop stability. For very small drops, the hydrostatic pressure is much less than the electrical pressure which yields an almost uniform charge distribution over the drop surface. For larger drop sizes, the hydrostatic pressure becomes more significant and the pressure difference between the pole and the equator of the drop becomes more noticeable. As soon as the drop starts to deform, the electrical charge will redistribute itself so that in this case (i.e. the prolate spheroid) it will have higher density on the drop pole than the equator. This compound effect of the hydrostatic pressure and the charge distribution increases the drop deformation which satisfies the drop equilibrium.

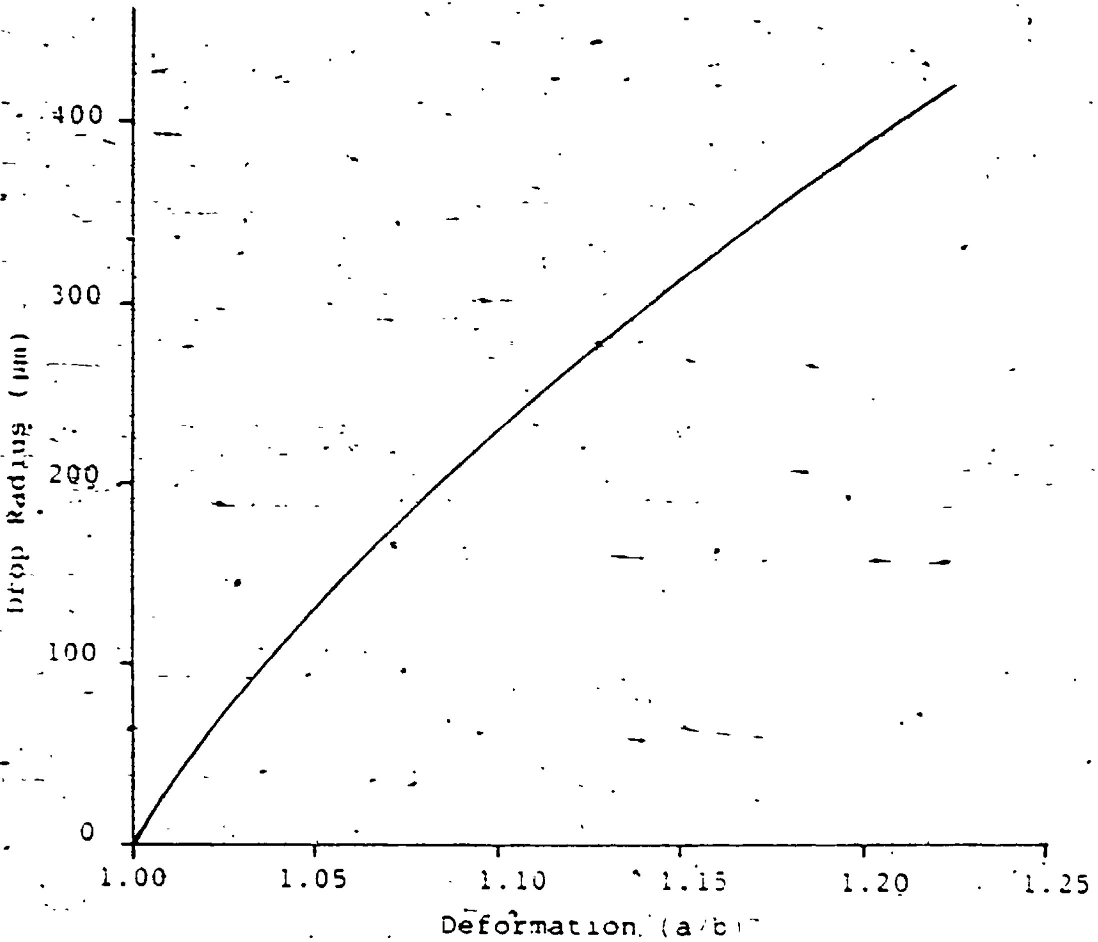

Figure 6.4 The Maximum Stable Deformation, Corresponding to the Drop Charge Limit, as a Function of Its Size Due to the Hydrostatic Pressure

6.2.2 Instability Due to Hydrostatic and Electric Field Pressures

To investigate the effect of another external force on the drop stability, a water drop of equivalent radius R is assumed to exist in a uniform electric field supporting it against the gravitational field. The terminal velocity, i.e. the aerodynamic pressure, is assumed to be very small so that it may be neglected. In turn the drop is assumed to retain a prolate spheroidal shape. It is important to note here that the electric field forces (QE) are chosen arbitrarily so that they do not correspond to the values equal to the gravitational force. However, the previous assumption of negligible terminal velocity can still be valid if one considers that the drop is moving under the effect of the difference of the electrical and the gravitational forces. This assumption can also be substantiated by assuming a high viscous external fluid.

The percentage ratio of the drop charge to its Rayleigh limit as a function of the drop deformation is shown in Figures 6.5 and 6.6 for different drop sizes and different applied electric fields. Figure 6.5 presents this characteristic for a water drop of 25 μm equivalent radius and for four different electric fields (0, 2, 4 and 6 MV/m). It shows that the drop charge decreases significantly with

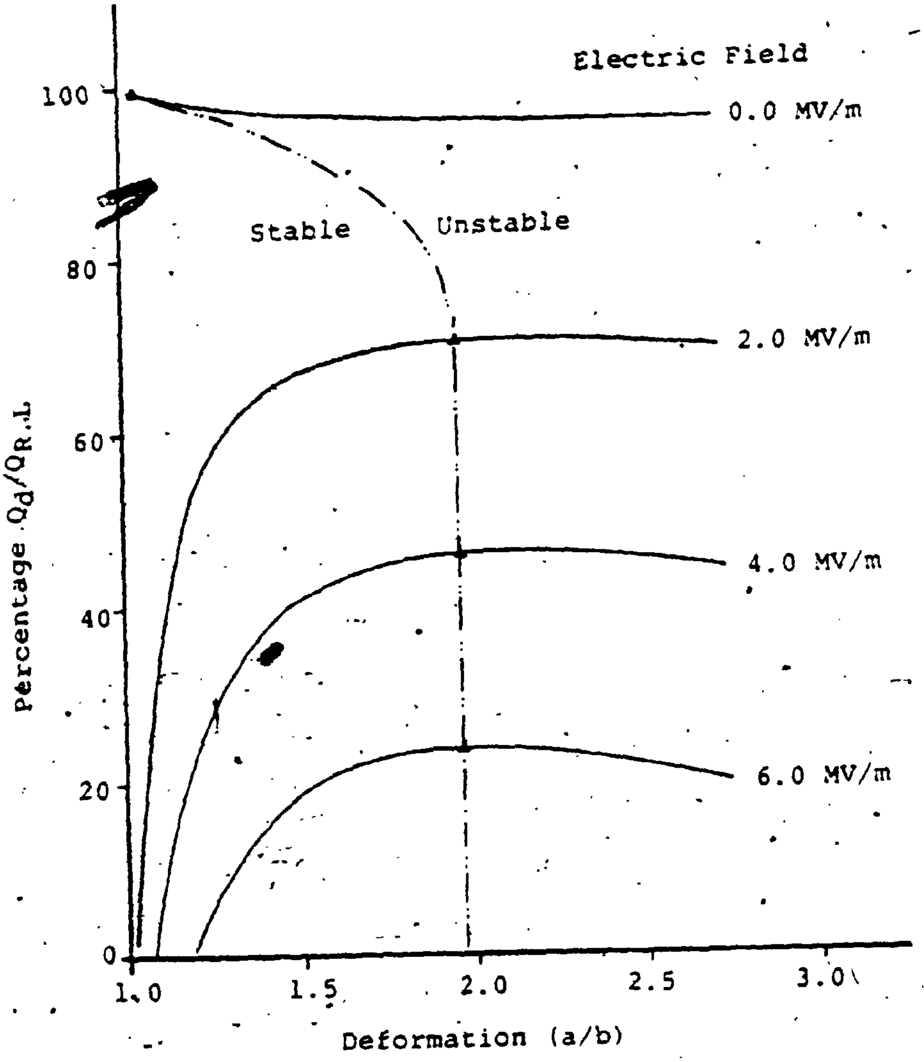

Figure 6.5 The Charge-Deformation Characteristic for Different Electric Fields and for Equivalent Drop Radius = 25 μm Due to the Hydrostatic and the Electric Field Pressures

the increase of the applied electric field. For each electric field there is an initial drop deformation below which the drop never achieves stable equilibrium. The initial deformation increases with the increase of the electric field. As the condition of zero external electric field represents the case of a hydrostatic force acting alone on the charged drop, the charge limit for 25 µm is very close to the Rayleigh limit and the drop deformation is very small. Increasing the applied electric field, the electrical pressure difference between the drop pole and its equator increases rapidly and the effect of the hydrostatic pressure on the drop shape becomes negligible. For relatively large electric fields, (about 2 MV/m), the electrical pressure becomes dominant and the maximum drop deformation tends to equal the value given by Taylor [12], (i.e. a/b = 1.9).

The same characteristics for larger drop sizes are also examined. Figure 6.6 shows the drop charge - deformation characteristic for water drops of 500 µm equivalent radius and for applied electric fields of (0, 0.5, 1, 1.5 MV/m). Comparing Figures 6.5 and 6.6, one can see that the charge of the larger drop is much more sensitive to the change of the electric field than the smaller drop, i.e. the percentage charge difference according to a change of the electric field ΔE is much larger for the large drop size.

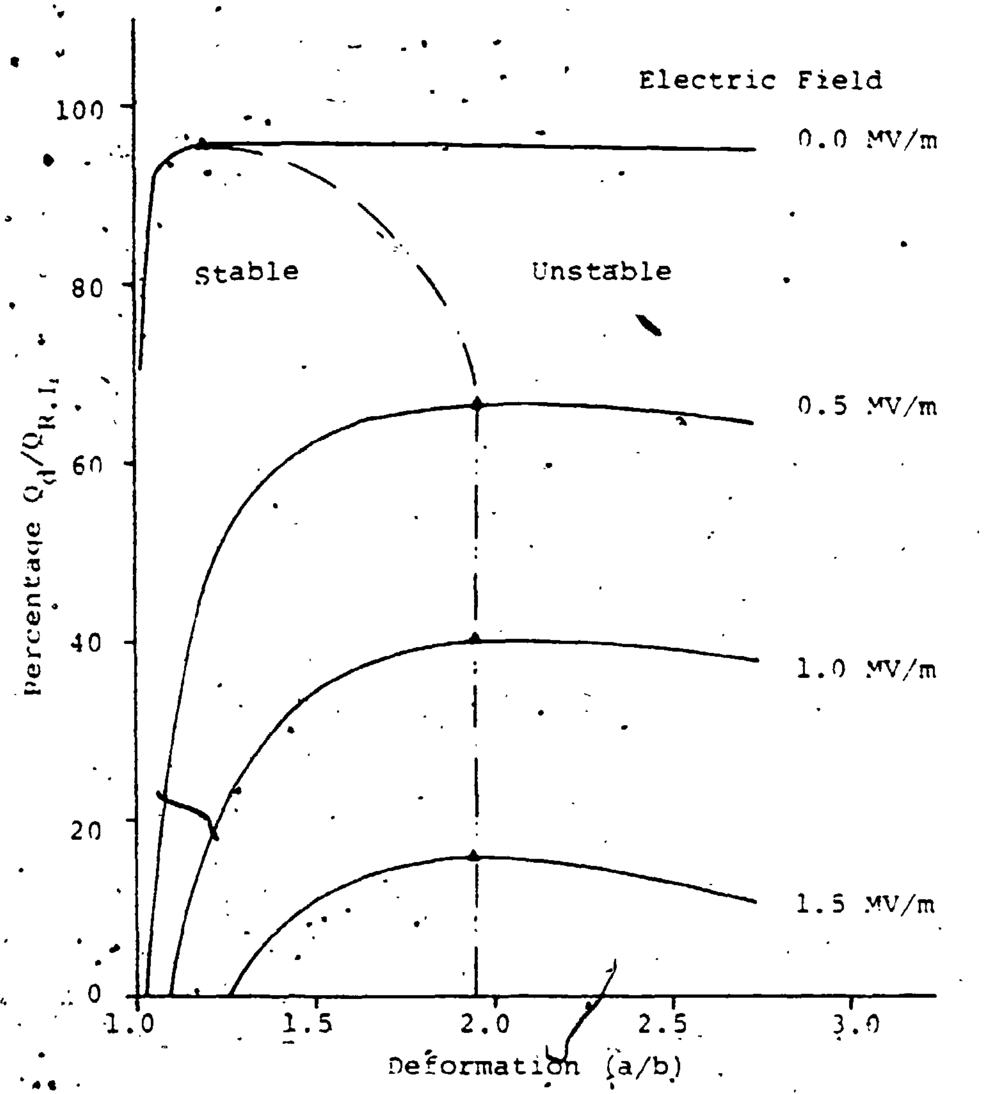

Figure 6.6 The Charge-Deformation Characteristic for Different Electric Fields and for Equivalent Drop Radius = 500 μm Due to the Hydrostatic and the Electric Field Pressures

One can also notice that by increasing the applied electric field, the initial drop deformation for the large drop increases more rapidly than that for the smaller drop. As the maximum stable deformation, as shown in Figure 6.4, is larger for large drop sizes, the contour of the maximum stable deformation starts at a larger aspect ratio for zero electric field (notice the difference of the starting point at zero electric field between Figure 6.5 and Figure 6.6). Increasing the applied electric field, the hydrostatic pressure component becomes negligible in comparison with the electrical pressure and the maximum deformation is then equal to the Taylor's maximum deformation ($a/b = 1.9$).

The effect of both the drop size and the applied electric field on the maximum charge limit of the drop are given in Figures 6.7 and 6.8. Figure 6.7 shows that the applied electric field decreases the charge limit significantly. It also shows that the effect of the electric field becomes much more important as the drop size increases. For each size, there is a certain electric field (E_{max}) at which the drop cannot carry any charge, i.e. the electric field is high enough to cause drop disruption. The analysis shows that E_{max} increases with the decrease of the drop size.

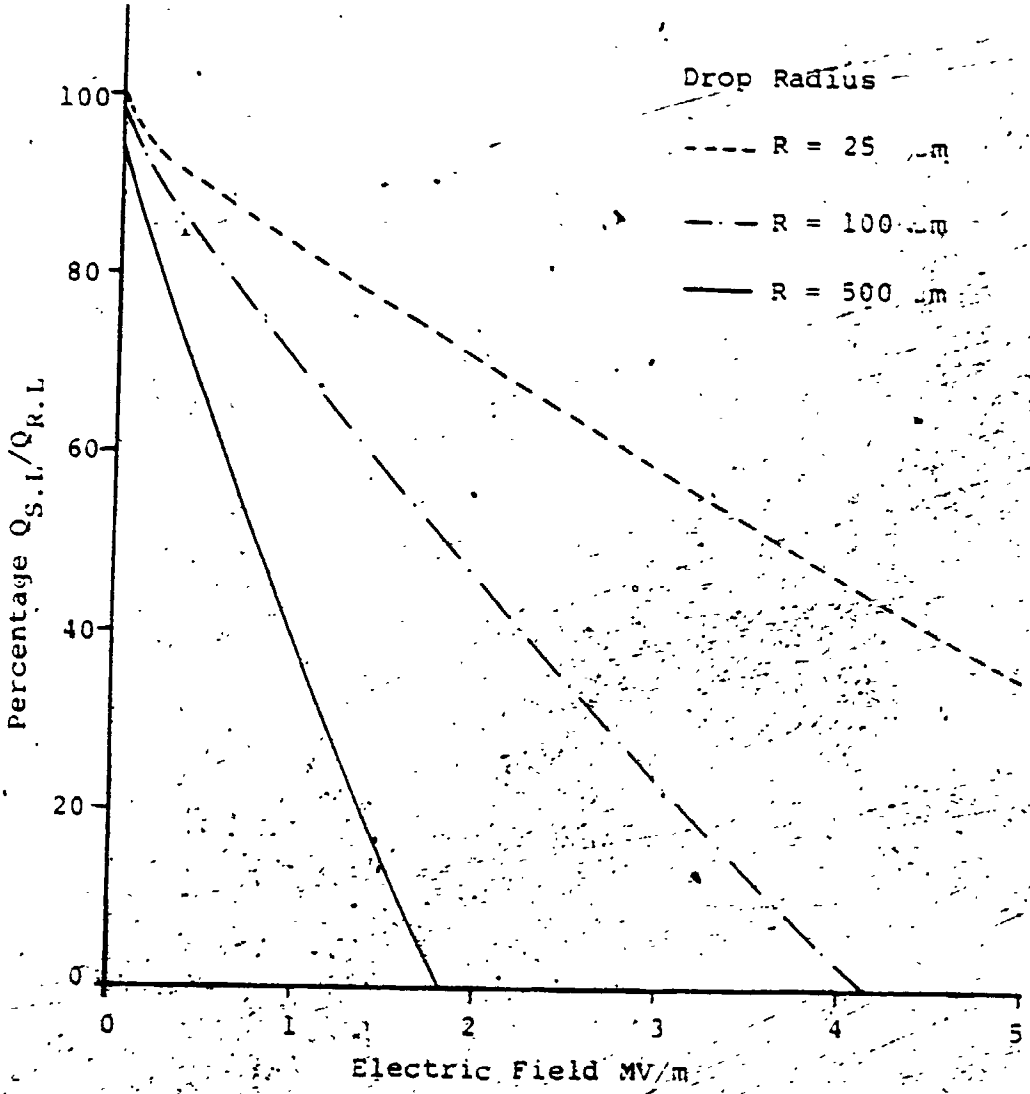

Figure 6.7 The Effect of the Electric Field on the Charge Limit of a Stable Drop for Different Drop Sizes Due to the Hydrostatic and the Electric Field Pressures.

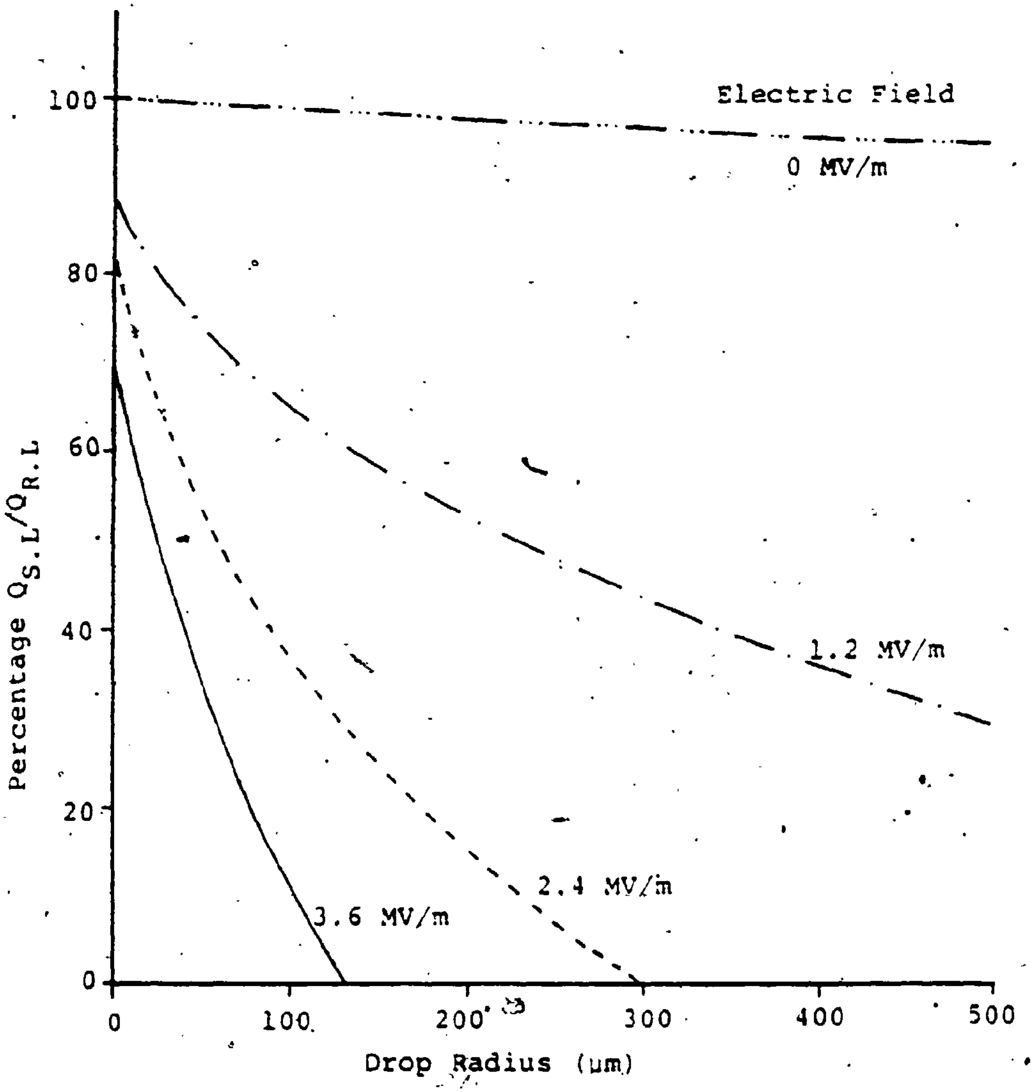

Figure 6.8 The Ratio of the Charge Limit of a Stable Drop to its Rayleigh Limit Charge as a Function of the Drop Size Due to the Hydrostatic and the Electric Field Pressures

Figure 6.8 illustrates the effect of the drop size on the charge limit of the drop. It shows that for a certain electric field, the charge limit decreases with the increase of the drop size. It also shows that this reduction becomes more noticeable with the increase of the applied electric field. For very low electric fields, $E \approx 0$, the charge limit is always very close to the drop Rayleigh limit regardless of the drop size because the only force acting on the drop besides the electric charge is the hydrostatic force. For higher electric fields, the electric pressure due to such fields becomes more dominant in determining the drop stability behaviour so that the charge limit decreases.

6.2.3 Instability Due to Hydrostatic, Electric Field and Aerodynamic Pressures

The most common practical case found in many electrostatic applications is the case of freely moving droplets in a uniform or non-uniform electric field. In this analysis, for simplicity, both the electric and the gravitational fields are considered to have the same direction. The constants K_1 and K_2 in Equation 5.16 are calculated numerically in terms of the drop deformation in three different ranges of Reynolds number. For $Re < 1$, the pressure distribution is assumed to obey the modified Stokes flow while for $1 > Re > 100$ the numerical data given by

Masliyah [60,61] are used. For higher Reynolds number, the flow is assumed to be potential flow. For more details about calculating these constants see Appendix IV.

Figures 6.9 through 6.11 illustrate the percentage ratio of the charge of a drop to its Rayleigh limit as a function of the drop deformation for different applied electric fields and different drop sizes. It is important to remember that the values of aspect ratio greater than unity represent prolate spheroids while those less than unity represent oblate spheroids. The numerical results of a 25 μm equivalent drop radius and zero electric field indicated that the aerodynamic pressure component on the drop is negligible (four orders of magnitude less than the electrical pressure) so that the charge - deformation characteristic (Figure 6.9) seems to be the same as that with hydrostatic force only. Increasing the electric field to 0.3 MV/m, the QE component of the force increases the drop velocity and the aerodynamic pressure becomes dominant (more than 6 times the other pressures) which yields a drop of an oblate spheroidal shape. By adding more charge to the drop for the same drop deformation and electric field, the difference between the aerodynamic pressure and the other pressures increases. This increase in the pressure difference acts on the drop so that further deformation takes place until a final equilibrium deformation is

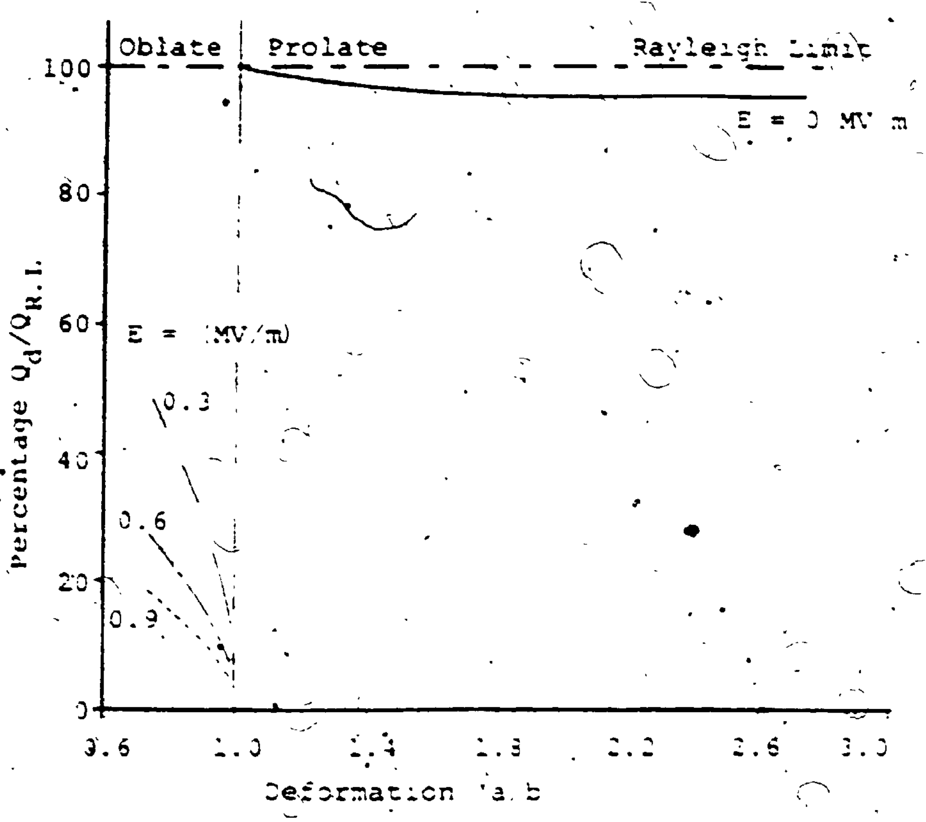

Figure 6.9 The Charge-Deformation Characteristic for Different Electric Fields and for Equivalent Drop Radius = .25 cm (General Case)

achieved. Increasing the electric field further, both the electric pressure and the aerodynamic pressure increases, but the difference between the two pressures becomes smaller. This decreases the ability of the drop to carry electrical charge and in turn, the drop requires less charge to achieve the same deformation.

Figure 6.10 illustrates the same characteristics for charged water drops of 100 μm equivalent radii. For zero external electric field, although aerodynamic pressure is less than the electric and the hydrostatic pressures, its value is not negligible. This decreases the total pressure difference (ΔP) at the drop tip (the weakest point) and in turn more charge can then be placed on the drop surface. This phenomenon leads, for very low deformation, to a predicted drop charge higher than the Rayleigh limit charge. This surprising prediction was certainly unexpected. However, for the static case, considered here, there may be some physical interpretations. These come from the following three main considerations.

1- The surface area of either a prolate or an oblate spheroid is larger than the surface area of an equivalent volume sphere so that the average surface charge density, in such cases, is less than the spherical case.

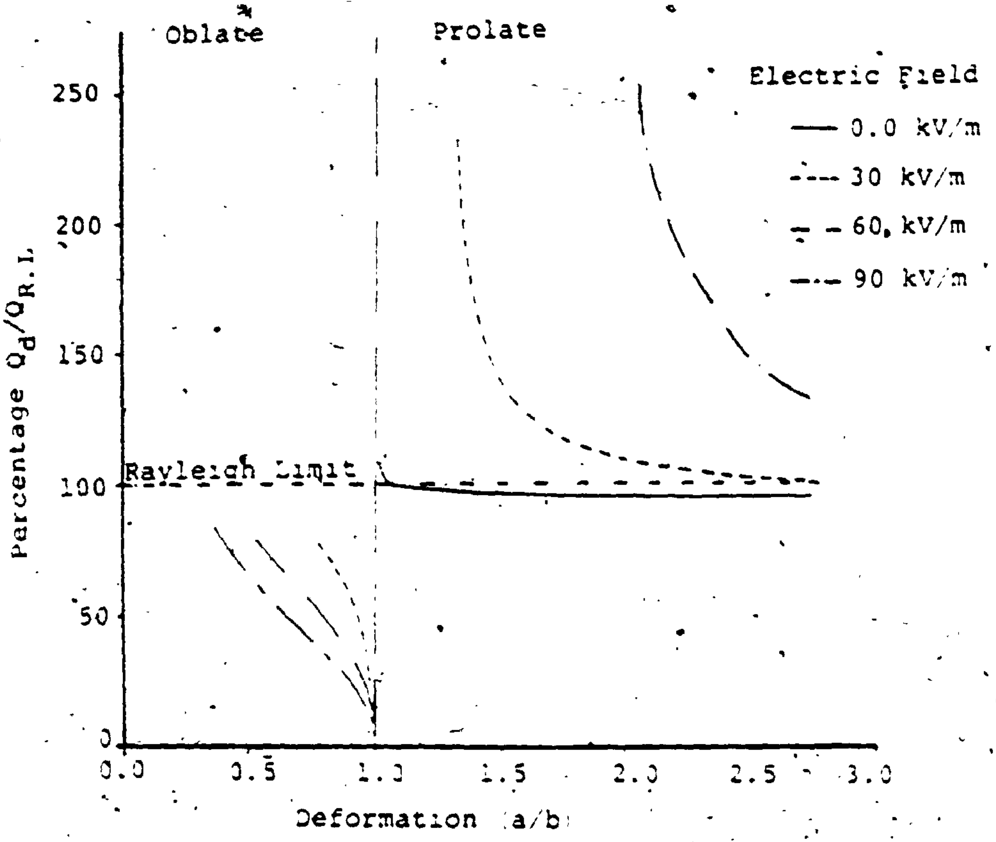

Figure 6.10 The Charge-Deformation Characteristic for Different Electric Fields and for Equivalent Drop Radius = 100 μm (General Case)

2- The radius of curvature at the drop tip is smaller than the equivalent spherical drop radius and in turn the surface tension pressure, at this point, is higher than the surface tension pressure at any point on the equivalent sphere.

3- The aerodynamic force acts in the same direction as the surface tension force at the drop tip. This decreases the effect of both the electric field and the hydrostatic pressures at this point. At the drop equator, although the surface tension pressure is less than the the surface tension pressure of an equivalent volume sphere, the electric charge density, at this point, is much less than the Rayleigh limit charge due to the uneven charge distribution over the deformed drop surface.

For a dynamic case, the previous prediction is probably unachievable. In this case, the stability equations (Eq. 5.21 and Eq. 5.27) must be modified and expressed as time dependent equations. The drop vibration, as the drop changes its shape, should also be considered.

Figure 6.10 also shows that, increasing the electric field in steps of only 30 kV/m leads to an oblate spheroid as described before. For higher deformations, the drop charge increases until a certain point at which the drop becomes unstable. At the drop instability limit, the drop is required to change its shape from an oblate to a prolate spheroid upon adding any further charge. Although the drop seems to carry charge, in the prolate side, higher than the charge limit, the transition from an oblate to a prolate spheroidal shape is considered a characteristic of instability since it is physically impossible for the drop to change its shape instantaneously without passing through any shapes of less deformation at which the drop charge causes breakup.

Figure 6.11 presents the percentage ratio of the drop charge to its Rayleigh limit as a function of the drop deformation for equivalent drop radius equal to 500 μm and for different electric fields. It shows that for zero electric charge (the QE force component = 0), the aerodynamic pressure dominates the drop shape so that the drop always takes an oblate spheroidal shape with an initial deformation of about 0.4. It also shows that changing the electric field, in the range between 0 to 90 kV/m, does not change the initial deformation of the drop since, for zero electric charge and in that range, the electric field effect on the drop shape is negligible. Increasing the drop deformation for the same electric field leads to a very sharp increase in the drop charge until it reaches a maximum

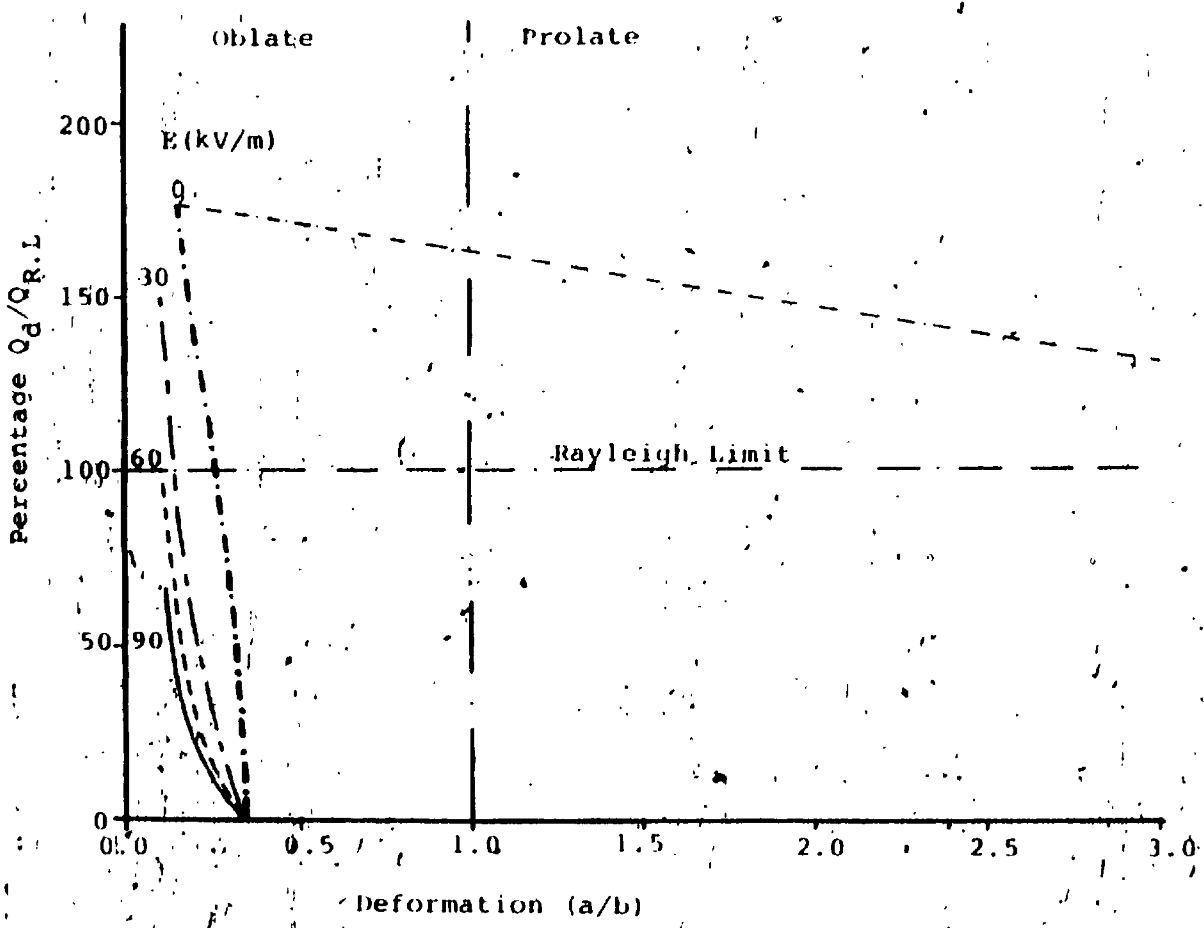

Figure 6.11 The Charge-Deformation Characteristic for Different Electric Fields and for R_o = 500 μm (General Case)

value, on the oblate side, much higher than the Rayleigh limit. It is also noticeable that increasing the electric field decreases the charge of the drop for the same deformation and decreases the slope of the curve.

From the previous evaluation of the stability equations, one can see that the external forces may have a dramatic effect on the drop charge limit and that for certain combinations of these forces, the Rayleigh limit is no longer the upper charge limit. This finding needs further study since in practice the drop has to pass through a series of different conditions before reaching its steady state. In practice, some of these conditions, such as the relatively low velocity or very high electric field around the nozzle as the drop is produced, may change the results considerably. The results of the previous evaluation also show that for small drop size (R < 50 μm) and for very low electric fields, the Rayleigh limit may be used in approximating the drop charge limit. For larger drop size or high electric fields, the Rayleigh limit is no longer valid.

CHAPTER SEVEN

THE CHARGE LIMIT OF LIQUID DROPLETS DUE TO ELECTRON AVALANCHES AND SURFACE DISRUPTION

7.1 Introduction

The objective of this chapter is to determine the maximum charge that a drop can retain under different air pressures, temperatures and relative humidities without losing its charge by corona discharge (electron avalanches) or by redistributing its charge through surface disruption. Two theoretical analyses are presented in this chapter. The first represents the case of a spherical droplet unaffected by any external force, while the second represents a drop distorted to a spheroidal shape due to the influence of preset combinations of external forces. The theoretical predictions are used to explain some experimental results previously reported in the literature.

7.2 A Review on Corona from Liquid Drops

The gas breakdown phenomenon due to the high electric field surrounding a highly stressed liquid drop falling in a uniform electric field was observed by Macky [45]. In a comparison of potentials required for surface instability inception and corona onset for water drops of about 450 µm radius at the end of an electrified capillary tube. English [30] concluded that negative corona was impossible, under his experimental conditions, due to the very low secondary emission coefficient of water. For positive drops of the same size, corona discharge appeared at pressures of 505 mm.Hg and less.

Corona onset is known to be a function of the drop radius and the gas pressure, temperature and relative humidity. Dawson [63,64] and Griffiths and Latham [65] showed that as the air pressure is reduced, the instability criterion of a water drop remains essentially unchanged whereas the corona onset field diminishes appreciably. Dawson [63] showed experimentally that for water drops of 220 µm radius or larger, positive corona was initiated when the pressure was below 650 mm.Hg. In his study, the threshold for negative corona was about 500 mm.Hg. As a result of these studies, it is now known that negative corona can also occur under suitable conditions from water surfaces, although for a given pressure, its onset electric field is higher than for positive corona. Thus negative corona occurs at lower pressures than that required for positive corona.

It is important to note here that for a drop unattached to any power supply, the gas breakdown phenomenon is different than the well known corona discharge because no continuous source of charge is available to maintain the corona process. Robertson [8] showed theoretically that a single avalanche was not enough to produce the rapid and enormous changes of the charge to mass ratio below the Rayleigh limit observed in his experiments at 95% relative humidity. He also concluded that the reason for losing the drop charge was either a series of avalanches or a large number of initiating electrons. In this study the term corona discharge is used to represent this gas breakdown condition.

7.3 Charge Loss Mechanisms

In addition to the drop breakup and the corona discharge, Robertson [8] discussed several other possible mechanisms by which a charged drop could lose its charge to the surrounding gas. Those include:

1- Photo emission due to incident light. This is a secondary mechanism and would be of interest only for negative highly charged drops of low photoelectric work function.

2- Field emission due to the intense field presented at the drop surface. Hendricks [2] concluded from a theoretical and experimental study that for octoil drops of radii 0.1 up to 10 microns, the charge to mass ratio of the oil drops were found to lie very close to the Rayleigh instability limit. He also showed that this limit was about a factor of 50 below the field emission limit predicted on the basis of Muller's work [66] on field emission. Kelly [67] predicted that at NTP, the crossover radius between field emission and Rayleigh limit is about 6 nm for molten copper droplets. For larger drop sizes, he noted that the Rayleigh limit prevails and limits the possible charge level attainable.

3- Evaporation of charged ions. Robertson noted that charge loss due to evaporating ions was negligible for highly charged evaporating drops. Iribarne and Thomson [68] showed that the evaporation of small ions from charged droplets should occur only when the drop reaches sizes of 10 nm or less. For sizes larger than that, they noted that the surface instability due to Rayleigh limit seems to be the most prevailing phenomenon.

4- Conduction due to the attraction of opposite polarity ions from the surrounding gas to the droplet surface thereby producing a discharge current. This process has a relatively long time constant at NTP but it is important to initiate the corona discharge.

From the previous discussion, surface instability and corona discharge may be considered to be the main competing processes that are able to relieve a large electric stress at a liquid drop surface. As the stress is increased, charge dissipation is the result of whichever mechanism occurs first. This study is an attempt to establish the threshold conditions controlling these two processes of charge reduction.

7.4 Analysis and Results

7.4.1 Spherical Drop

A semi-empirical formula for corona onset has been introduced by Hartmann [69] which is a recent improvement on the classic Peek's formula. This formula yields the onset gradient (E_c) in air for positive polarity cylindrical and parabolic point to plane geometries. It takes into account the effect of air humidity, temperature, pressure and the curvature radius (R) of the rod tip. It also covers a wide range of rod radii(R $\geq$ 0.1 μm). This formula can be written in the form

$$E_c = E_0\,(\delta,H)\ [1+ \frac{A_0}{R^{B_0}}\ f(R,\delta,H)\ g(R)] \qquad 7.1$$

where A_0 and B_0 are constants, H is the absolute air humidity in g/m^3, R is the tip curvature and δ is the air density factor which equals one at NTP. The functions g(R), f(R,δ,H) and E (δ,H) can be calculated using the expressions given by Hartmann [69]. Although this formula does not cover the cases of spherical and spheroidal electrodes, Berger [70] introduced mathematical functions that take into account the effects of electrode geometries. These functions are based on modifying the anode radius of curvature which represents the equivalent radius of a sphere that have the same corona onset. His results showed that the parabolic point to plane geometry had the same corona onset as that of a sphere to plane when the gap length is large enough ($d \geq 10$ R). Since in most electrostatic applications the distance between the drop and the grounded plane is very large, this formula may be used as a first approximation to calculate the onset gradient (E_c) for both spherical and spheroidal drops. In this case the tip curvature (R) in Equation 7.1 is replaced by the drop radius of curvature. Since this formula is valid only for positive corona and since to the author's knowledge, no other formula is valid for the same conditions for negative corona, all the work in this chapter will consider the positive case only.

It has been observed experimentally [71-74] that the effect of relative humidity on the corona onset field is a function of the corona polarity and the electrode radius of curvature. For positive corona, the corona onset field increases with relative humidity for large electrode radius of curvature [72-74]. For small electrode radius of curvature, a reverse effect is observed [71,75-77]. Since Hartmann took this phenomenon into account in driving his equation, one can see that for the small radii of curvature used in this study, the increase of relative humidity will enhance the corona due to the reduction of the corona onset field.

Assuming a spherical drop unaffected by any other forces, the surface charge associated with the air breakdown around the drop "corona onset" can then be calculated as

$$Q_c = E_c \cdot 4\pi\epsilon R^2 \qquad 7.2$$

For the same drop, the stability limit can also be calculated according to the Rayleigh limit ($Q_{R.L}$), i.e. the maximum charge a stable drop can retain is given by Equation 1.1.

A numerical technique was adapted to calculate Q_c and $Q_{R.L}$ for various drop radii under variable conditions of temperature, pressure, relative humidity and liquid surface tension. The percentage ratio $Q_c/Q_{R.L}$ was then calculated. It is clear that for all the values of $Q_c/Q_{R.L}$ less than 100%, the surface charge which leads to corona discharge, or set of electron avalanches, is less than that required to cause surface instability. The loss of charge under such a condition is then by electron avalanches. If the ratio $Q_c/Q_{R.L}$ is higher than 100%, the loss of charge will be by surface instability (disintegration).

Figures 7.1 and 7.2 represent the percentage ratio of $Q_c/Q_{R.L}$ for water droplets with respect to the drop radius for different relative humidity conditions and under different air temperatures. These curves show that the higher the relative humidity of the surrounding air, the more the tendency of the drop to lose its charge by electron avalanches (corona). This is because, for this range of drop radii, the higher the relative humidity, the higher the relative difference between the first ionization coefficient of the gas and the attachment coefficient. This leads to more ions per avalanche and in turn lower corona onset field. Figure 7.1 shows that under NTP and for dry air or standard relative humidity (R.H.=60%), the drop always disintegrates rather than experiencing electron avalanching. Only for saturated air and for drop radii in the range of 40 to 120 µm, do the drops lose their charge by electron

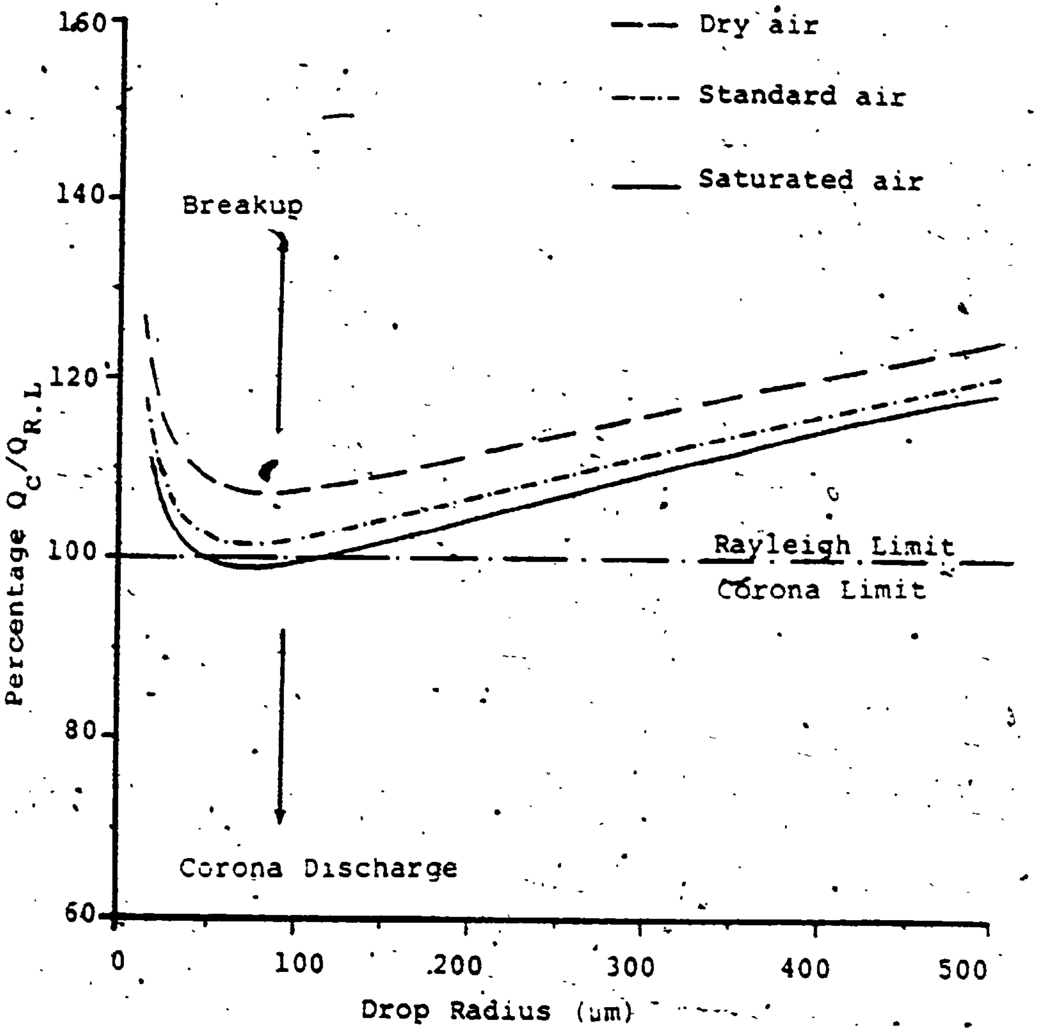

Figure 7.1 The Percentage Ratio of $Q_C/Q_{R.L}$ for Water Drops of Different Radii and Different Air Humidity at P = 760 mm.Hg and T = 20°C.

avalanches.

Figure 7.2 shows that changing the air temperature from [illegible]0 to 40°C, the drop radii, corresponding to corona discharges for saturated air, cover the range between 20 µm to 270 µm. For standard air, that range covers the drop radii of 40-140 µm. For dry air, a drop of any radius tends to disintegrate. These results may clarify why some previous investigators have concluded that corona discharge rather than the drop breakup is the reason for the rapid changes of the charge to mass ratio below the Rayleigh limit while employing high relative humidity in their experiments [8]. Owe-Berg and George [29] also showed experimentally that water drops of about 40 µm radii breakup at normal relative humidity. For saturated air, they concluded that another phenomenon rather than the drop surface instability was occuring to relieve the drop charge. They assumed the reason for that was due to an evaporation of ions from the drop surface. However, the results presented here suggest that this phenomenon was probably electron avalanching.

Figure 7.3 presents the effect of changing the air pressure for water drops on the percentage ratio $Q_c/Q_{R.L}$ as a function of the drop radius. It shows that reducing the air pressure decreases the ratio $Q_c/Q_{R.L}$ which in turn increases the range of radii at which corona discharge takes

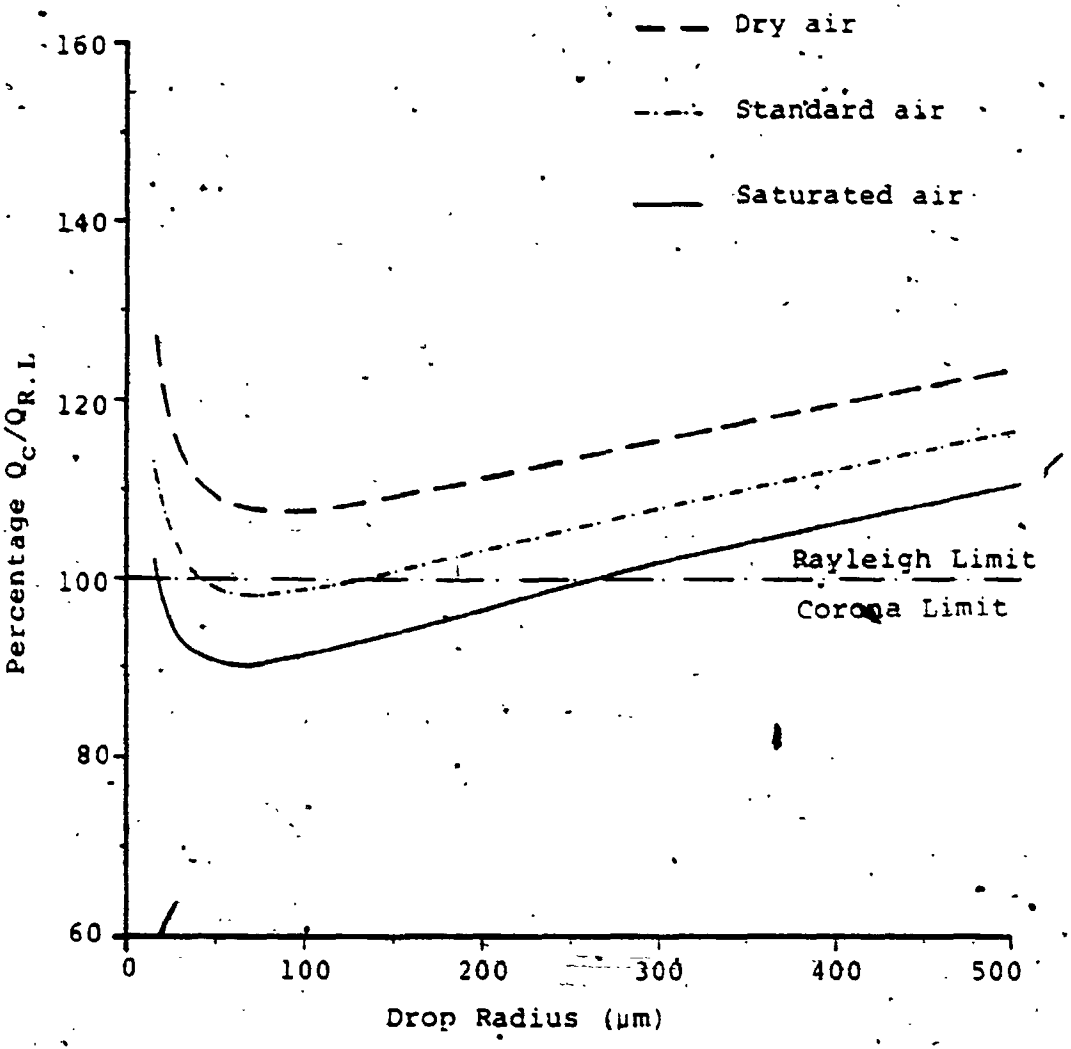

Figure 7.2 The Percentage Raio of $Q_C/Q_{R.L}$ for Water Drops of Different Radii and Different Air Humidity at P = 760 mm.Hg and T = 40°C.

place. This result is supported by the experimental results of English [30] and Dawson [63]. English showed that for positive water drops of about 450 μm radius, corona discharge appeared at pressures of about 505 mm.Hg or less. In Figure 7.3, for water drops of radii equal 450 μm, corona appears at pressures of about 550 mm.Hg or less. Remarkably, the difference between the predicted pressure and that reported by English is only 9%. For smaller drop sizes (220 um), the predicted pressure at which corona discharge is initiated closely matches the experimental observations reported by Dawson at 650 mm.Hg with percentage differences less than 2%.

Figures 7.4 and 7.5 show the influence of several factors which govern the liquid surface tension on the percentage ratio of $Q_c/Q_{R.L}$ as a function of the drop radius. Figure 7.4 shows that for NTP and for standard air humidity (60%), increasing the liquid temperature enhances the possibility of the breakup. This result can be explained due to the fact that increasing the liquid temperature decreases its surface tension and in turn reduces the Rayleigh limit of the drop while the corona limit is almost the same.

Figure 7.5 examines the effect of changing the drop liquid in changing the percentage ratio of $Q_c/Q_{R.L}$. Four

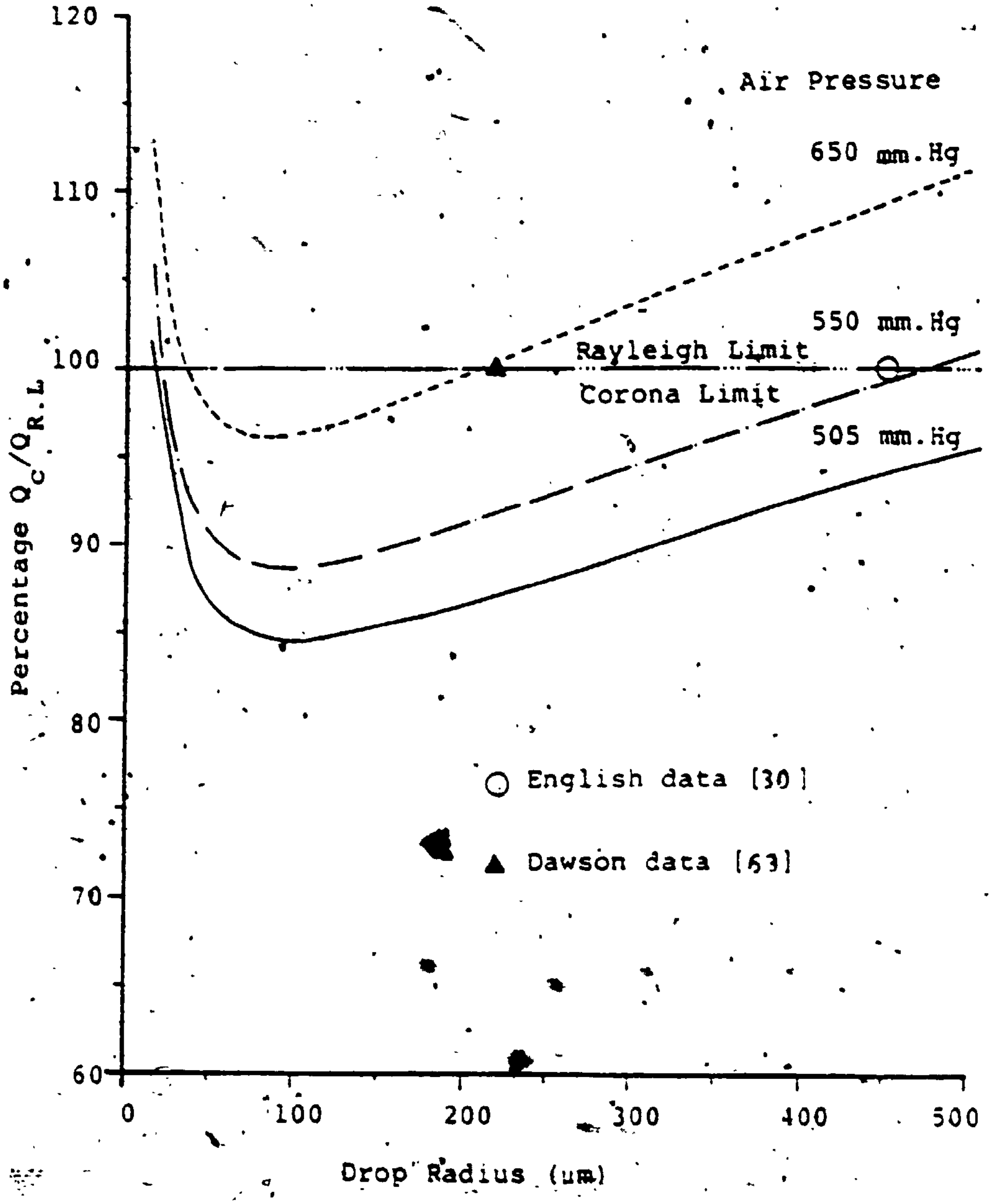

Figure 7.3 The Percentage Ratio of $Q_C/Q_{R.L}$ for Water Drops of Different Radii and Different Air Pressures at Standard Air Humidity and T = 20°C

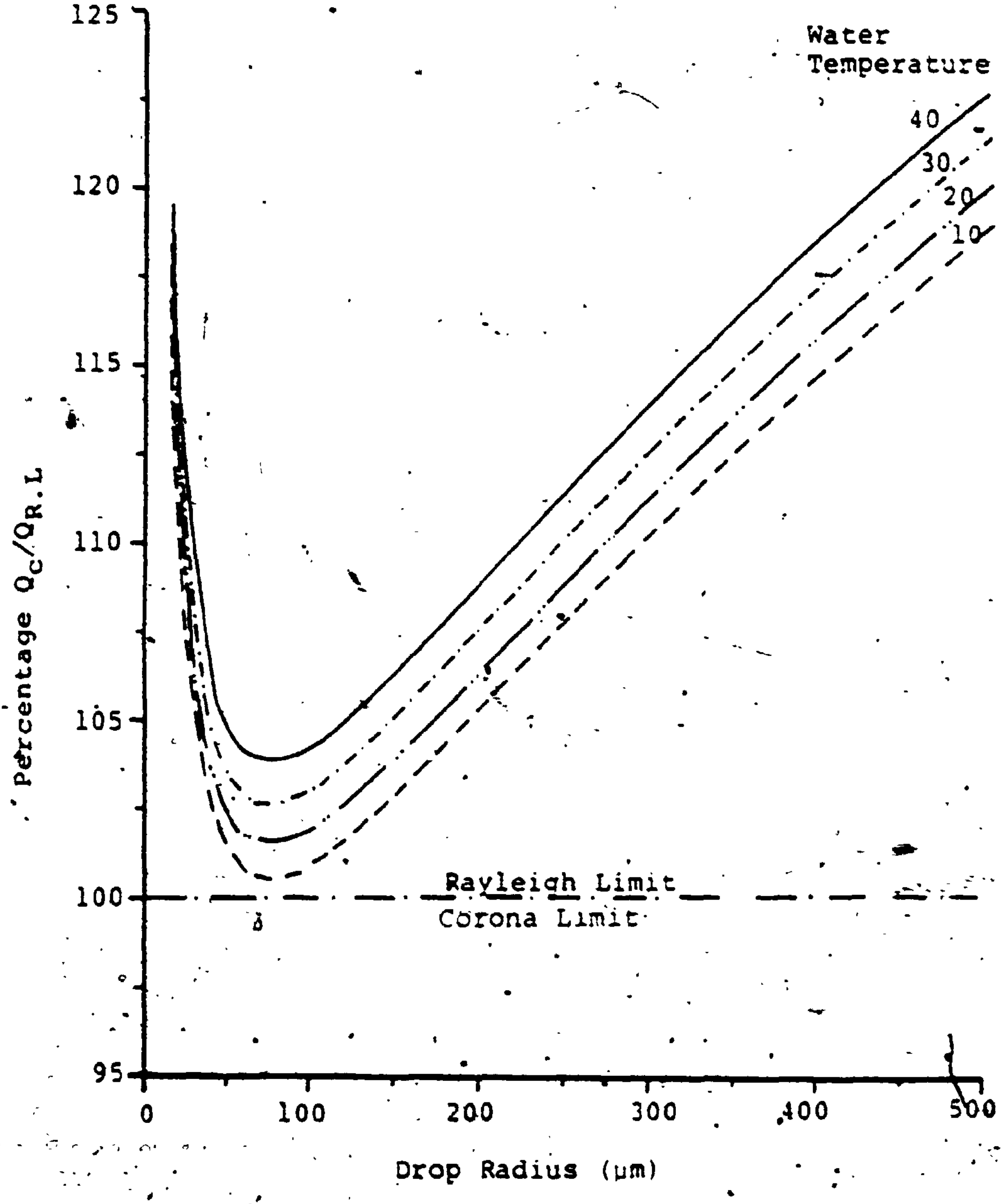

Figure 7.6 The Effect of the Water Temperature on the Percentage Ratio of $Q_C/Q_{R.L}$ as a Function of the Drop Radius for Standard Air at P = 760 mm.Hg and T = 20°C

different liquids (water, analine, n-octane, and alcohol of surface tensions 72.7, 42.9, 27.5 and 22.7 mN/m respectively) are used in this comparison. As the corona onset, Equation 7.1, is the same for any liquid due to the fact that it is not a function of the liquid surface tension, Q_c will be the same for the four liquids while the Rayleigh limit is different for each of them. One can expect that the higher the surface tension, the lower the percentage ratio of $Q_c/Q_{R.L}$. Figure 7.5 shows that, for one half the atmospheric pressure, water drops which have the highest surface tension, reach the corona onset before the surface instability for all the drop radii under consideration. It also shows that an analine drop only loses its charge by electron avalanches for any drop radius in the range between 30 and 440 µm. For liquids of relatively low surface tension, n-octane and alcohol, even for air pressures equal to 380 mm.Hg, the Rayleigh limit prevails and restricts the maximum charge level since the stability limit charge is much less than the corona onset charge.

7.4.2 Spheroidal Drops

In any actual case, the assumption of a spherical drop, on which the Rayleigh limit is based, is not valid, especially for large drops. As discussed in Chapter 5, the

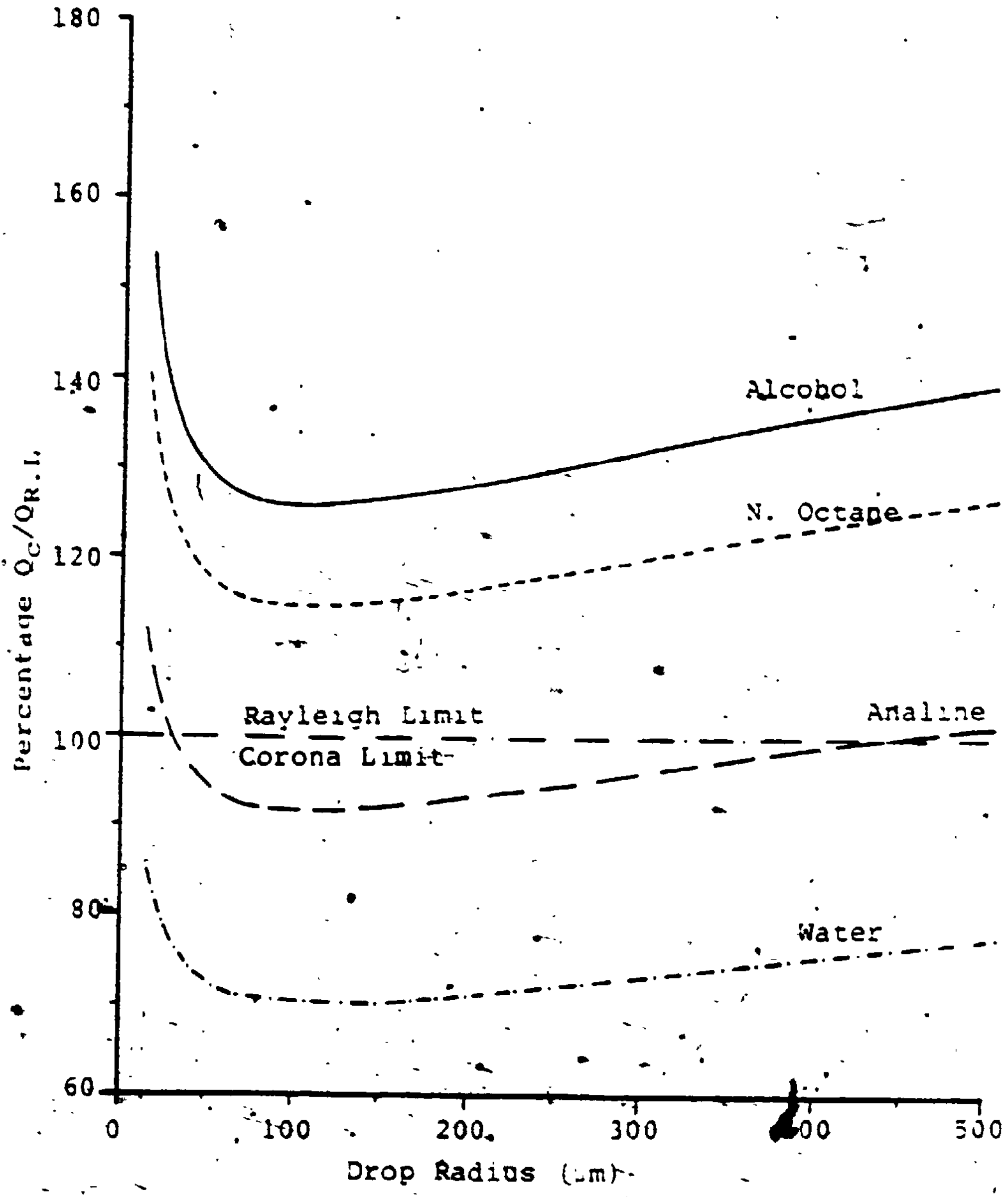

Figure 7.5 The Percentage Ratio of $Q_C/Q_{R.L}$ for Different Liquids w.r.t. Drop Radius at $P = 380$ mm.Hg, $T = 20$°C and Standard Air

effect of the external forces may change the stability limit from the value predicted by Lord Rayleigh. Following the analysis of Chapter 5, the drop is assumed to deform to either a prolate or an oblate spheroid and the maximum stability limit of the drop is then calculated using the numerical method, employing Equations 5.21 and 5.27, for selected values of the drop radius, the liquid surface tension and the external electric field.

For a spheroidal drop, the charge redistributes itself over the drop surface so that the smaller curvature of the drop acquires higher charge density which may enhance the probability of corona discharge around this area. On the other hand, smaller radii of curvature require higher electric fields to initiate the corona around the drop tip. In the present study, the smaller radius of curvature of the drop is assumed to be more susceptible to corona than the rest of the drop surface.

The smaller radius of curvature (R_c) of a prolate spheroid (point A in Figure 7.6.a) is b^2/a (Eq. 5.3). This value can be expressed in terms of the undeformed drop radius (R) to be

$$R_c = R\alpha^{2}/3 \qquad 7.3$$

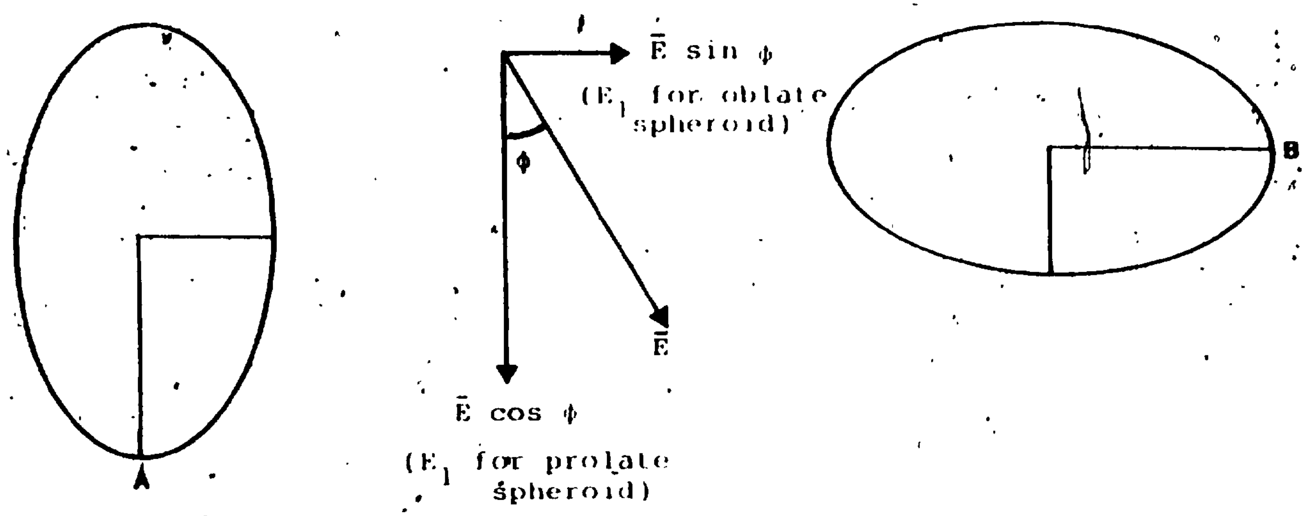

a - Prolate Spheroid

b - Oblate Spheroid

Figure 7.6 Schematic Diagram for Spheroidal Drops where $\alpha = b^2/a^2$

while for an oblate spheroid (point B in Figure 7.6.b)

$$R_c = \frac{1}{2}\left[\frac{b^2}{a} + a\right]$$

$$= \frac{2R\alpha^{5/6}}{1+\alpha} \qquad 7.4$$

Using Equation 7.1, the electric field (E_c) associated with the corona onset can be calculated. However in the case of external electric field ($\bar{E}$), E_c consists of two components, E_1 which is the external field component in the direction of the onset field ($\bar{E}\cos\phi$ for a prolate spheroid and $\bar{E}\sin\phi$ for an oblate one) and E_{cQ} which is the electric field due to the electric charge at the spheroid tip (Figure 7.6). Assuming a known magnitude and direction of the external field ($\bar{E}$), E_{cQ} can be calculated as

$$E_{cQ} = E_c - f(E_1) \text{ , } f(E_1) \text{ is calculated from Eq. 5.11} \qquad 7.5$$

In this study, the external electric field is assumed to have the same direction of the gravitational field so that $E_1 = |E|$ in the case of a prolate spheroid and $E_1 = 0$ for an oblate spheroid. The total charge on the drop (Q_c) associated with the corona onset can then be calculated as [56] for a prolate spheroid

$$Q_c = 4\pi\varepsilon R^2 \; E_{cQ}\alpha^{1/3} \qquad 7.6$$

while for an oblate spheroid

$$Q_c = 4\pi\varepsilon R^2 \; E_{cQ} \; \alpha^{1}/_{6} \qquad 7.7$$

A numerical technique was adapted to calculate the stability limit ($Q_{s.L}$), the corresponding drop aspect ratio, the tip curvature (R_c) and the onset charge (Q_c) for various drop radii. The effect of the external forces such as the gravitational force, the external electric field and the aerodynamic force are taken into account in calculating the stability limit and the drop deformation as discussed in Chapter 6. The factors affecting the corona onset charge such as air pressure, temperature and relative humidity are considered through Hartmann's equations [69]. The effect of these factors on the air density and its viscosity is also taken into account in calculating the aerodynamic forces on the drop. The percentage ratio $Q_c/Q_{s.L}$ is then evaluated. It is clear, as mentioned before, that for all values of $Q_c/Q_{s.L}$ higher than 100%, the loss of charge is due to the surface instability (disintegration).

Figures 7.7 -7.10 present the percentage ratio $Q_c/Q_{s.L}$ for values of undistorted drop radius from 10 to 360 µm and for different conditions. Since there is no common

3 3

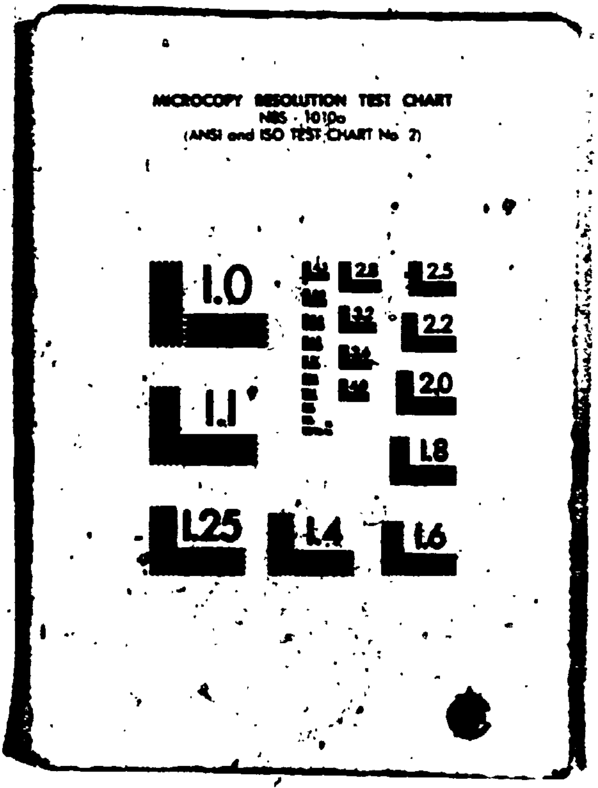
MICROCOPY RESOLUTION TEST CHART
NBS 1010a
(ANSI and ISO TEST CHART No. 2)

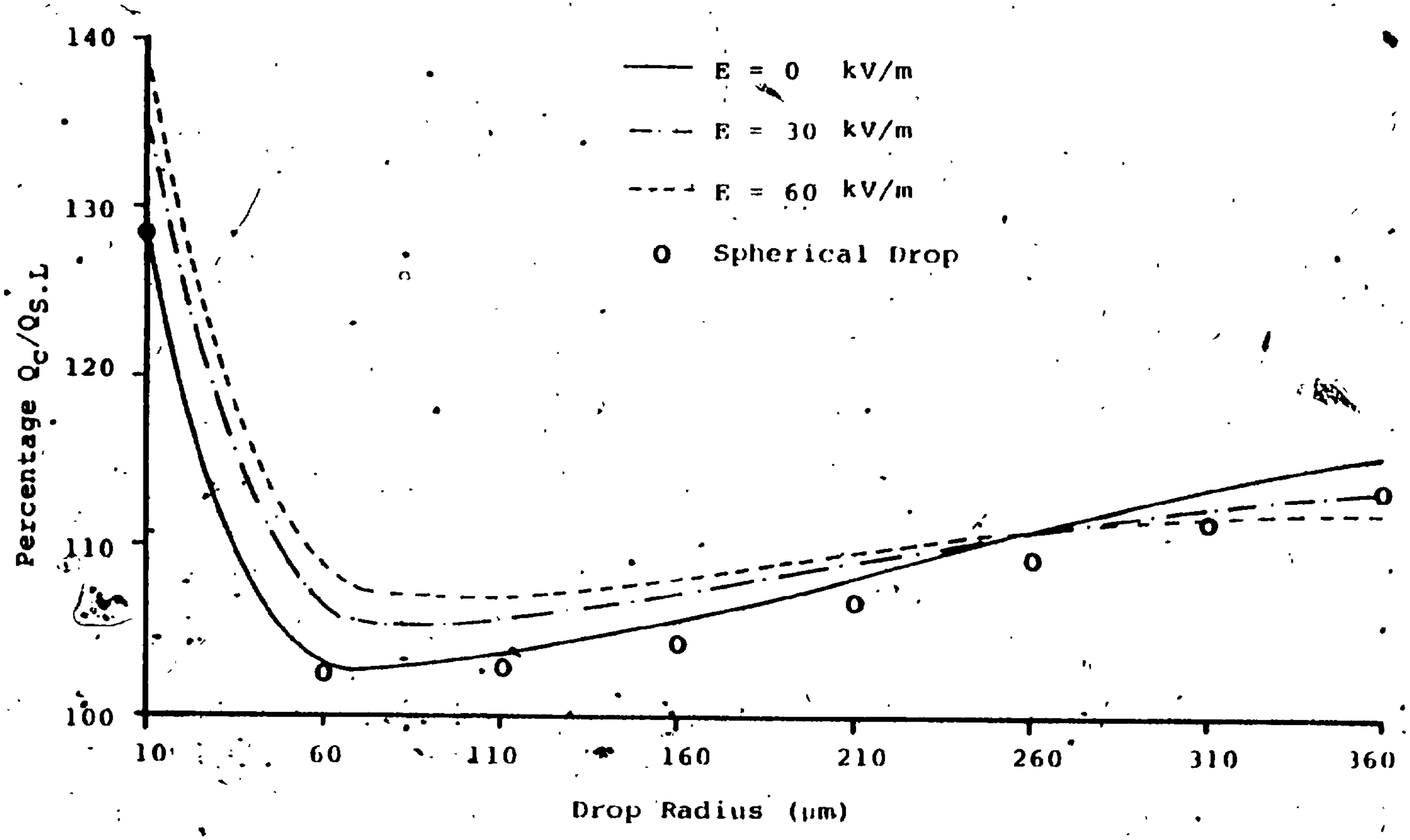

Figure 7.7 The Percentage Ratio of $Q_C/Q_{S.L}$ as a Function of the Drop Equivalent Radius for Different External Fields at P = 760 mm.Hg, T = 20°C "Zero Aerodynamic Force"

reference between the curves presented in these figures, the actual charges Q_c and $Q_{s.L}$ cannot be estimated from such figures. To calculate the actual charge limit of a drop of a certain radius and under prespecified conditions, Q_c and $Q_{s.L}$ should be calculated numerically and the smaller should be chosen to be the upper charge limit for such conditions.

Figure 7.7 presents the percentage ratio of $Q_c/Q_{s.L}$ at NTP for different external electric fields where the drop terminal velocity, i.e. the aerodynamic force, is assumed to be zero. In this case, the drop exhibits a prolate spheroidal shape (Chapter 6). Figure 7.7 also presents the case of a spherical drop unaffected by any external force. A comparison between the case of zero external electric field and the case of a spherical drop illustrates that the effect of the gravitational force increases the ratio $Q_c/Q_{s.L}$. It also shows that the difference between the two cases is negligible for small drop sizes but increases with drop radius. The numerical evaluation of the individual force components showed that increasing the electric field decreased the stability limit ($Q_{s.L}$) while the corona limit (Q_c) was almost the same so that the ratio $Q_c/Q_{s.L}$ increased. For large drop sizes, the decrease in the corona limit due to the drop deformation and the charge redistribution became more effective so that the ratio

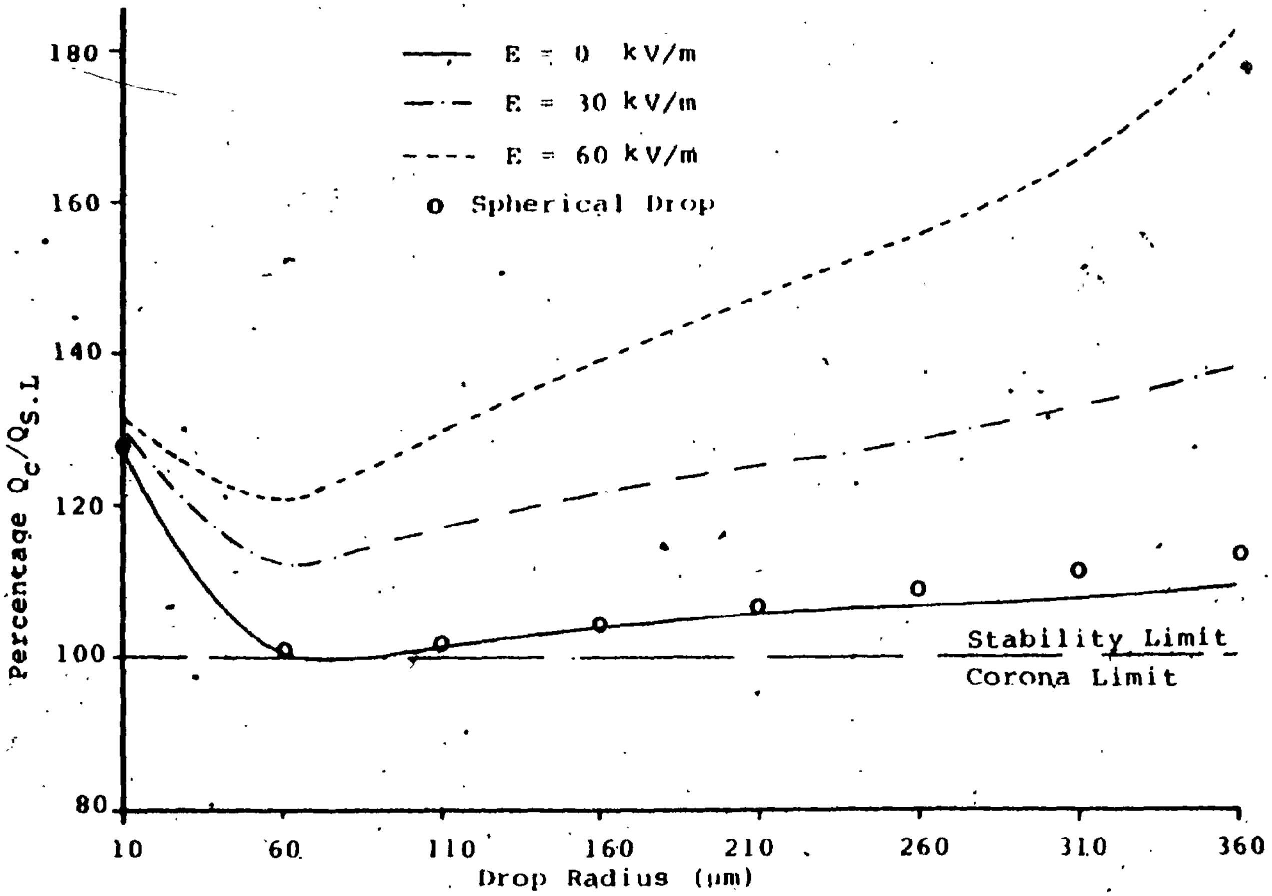

Figure 7.8 The Percentage Ratio of $Q_C/Q_{S.L}$ as a Function of the Drop Equivalent Radius for Different External Fields at P = 760 mm.Hg and T = 20°C "General Case"

$Q_c/Q_{s.L}$ decreased. Figure 7.8 presents the same conditions of Figure 7.7 with the aerodynamic force in effect. The drop in such a case may exhibit an oblate spheroidal shape (Chapter 6). It shows that increasing the external electric field increases the ratio $Q_c/Q_{s.L}$. The numerical evaluation of the individual force components showed that increasing the electric field decreased the stability limit ($Q_{s.L}$) so that the ratio $Q_c/Q_{s.L}$ increased. Comparing the case of zero external field in Figure 7.7 with that of Figure 7.8, one can recognize that the effect of the aerodynamic force alone decreases the ratio $Q_c/Q_{s.L}$. The reason for this is, in such a case, the aerodynamic force component becomes more effective in deforming the drop shape and hence decreasing the corona limit (Q_c).

The effect of the air pressure and the air temperature in changing the percentage ratio $Q_c/Q_{s.L}$ are presented in Figures 7.9 and 7.10. Figure 7.9 shows the same results demonstrated in Figure 7.3, i.e. reducing the air pressure decreases the ratio $Q_c/Q_{s.L}$ which in turn increases the radius range at which corona discharge takes place. For atmospheric pressure and for the case of an external electric field of 30 kV/m, Figure 7.10 shows that increasing the air temperature decreases the percentage ratio $Q_c/Q_{s.L}$. The reason for that is, increasing the air temperature decreases the corona onset due to the decrease in the air

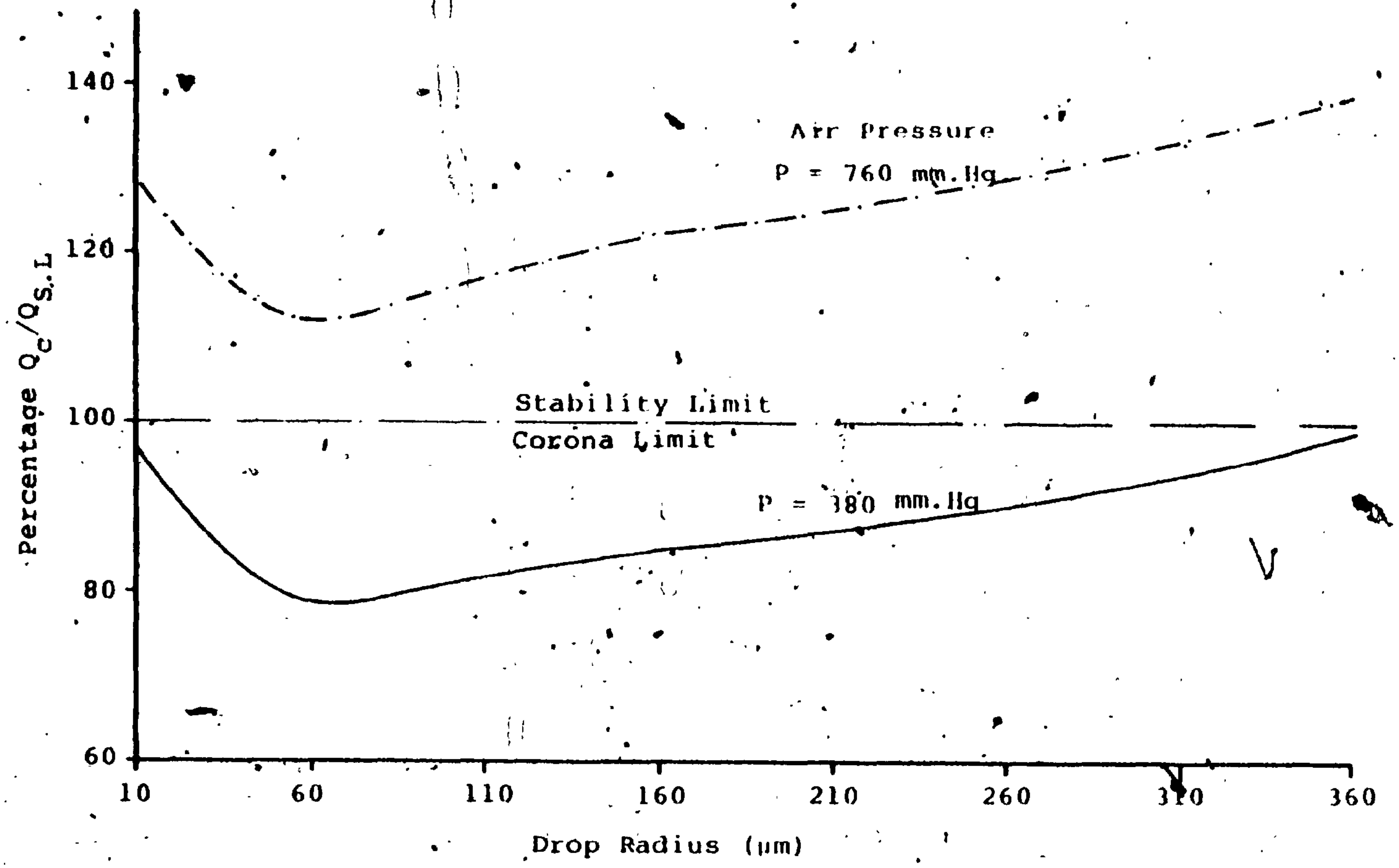

Figure 7.9 The Percentage Ratio of $Q_C/Q_{S.L}$ as a Function of the Drop Equivalent Radius for Different Air Pressures at E = 30 kV/m and T = 20°C

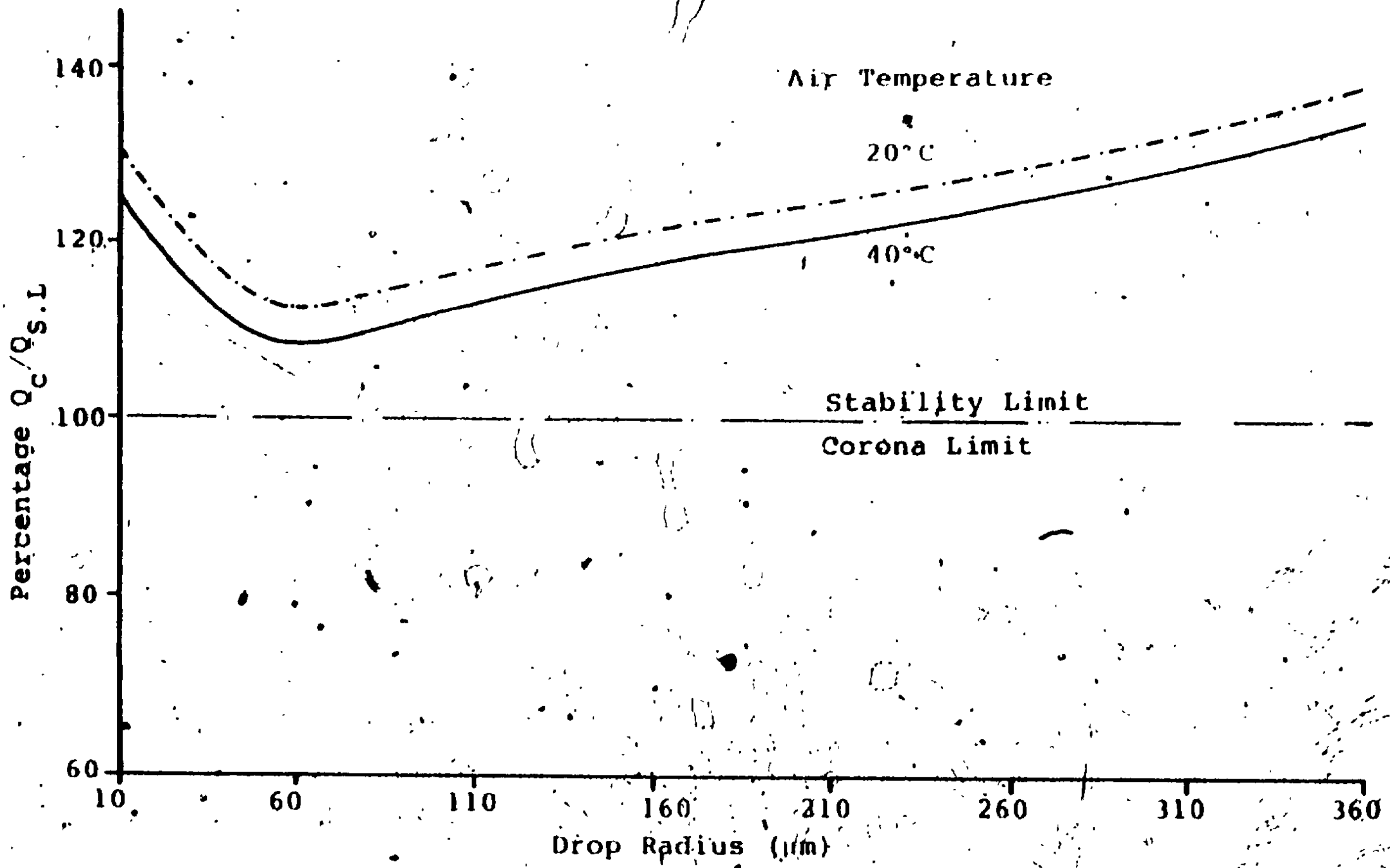

Figure 7.10 The Percentage Ratio of $Q_c/Q_{S.L}$ as a Function of the Drop Equivalent Radius for Different Air Temperatures at P = 760 mm.Hg and E = 30 kV/m

density (δ). This decrease in the corona onset seems to be more effective than the decrease in the stability limit due to the decrease of the surface tension so that the percentage ratio $Q_c/Q_{s.L}$ decreases.

7.5 Discussion

In this chapter, the instability-corona charge limit of a charged liquid drop is clarified. However, in some electrostatic applications, the maximum charge of the drop might be limited by the charging process. In Chapter 1, the methods with which liquid droplets can be charged was discussed. The maximum possible charges which can be placed on a drop using these methods are given in Eq. 1.3 - 1.5. Figures 7.11 and 7.12 present comparisons between the maximum charges on a spherical liquid drop due to different charging methods with those of the Rayleigh limit and the corona limit, obtained in this chapter, for different drop radii and for different air pressures. Figure 7.11 shows that at NTP, the Rayleigh limit restricts the maximum charge which can be placed on a drop under such conditions. It also shows that both the conduction charging and the corona charging (Pauthenier) provides much less charge than that limit and that the conduction charging presents more charge to the drop than that given by corona charging (Pauthenier) especially for large drop sizes. At one half atmospheric

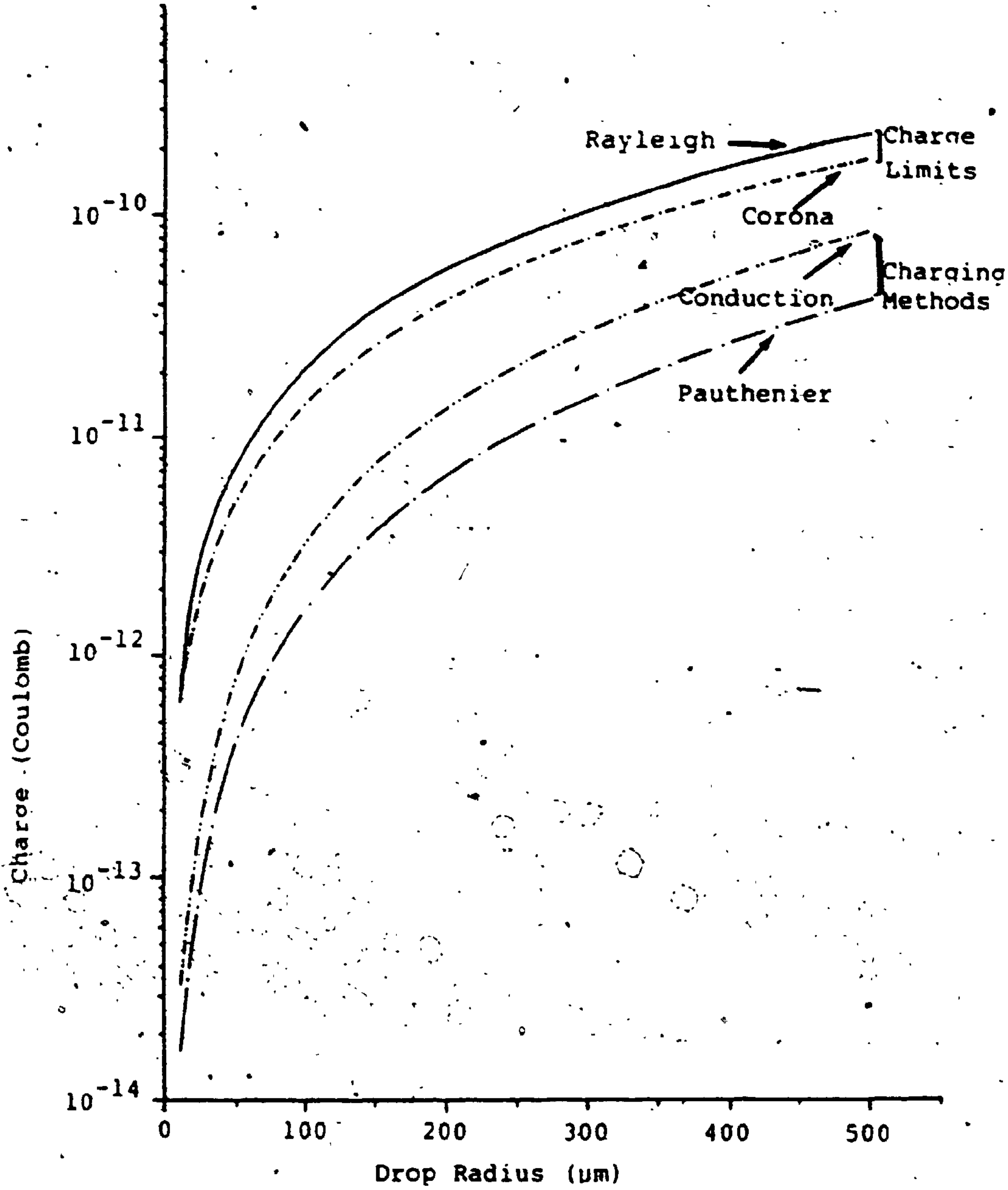

Figure 7.12 The Maximum Charge on a Spherical Drop Due to Different Charging Methods and Charge Limits at T = 20°C and P = 380 mm.Hg.

pressure, the corona limit becomes the factor in determining the maximum charge a drop can retain, Figure 7.12 shows that both the conduction charging and the corona charging are far below this limit. The previous results show that the charging methods need to be improved so that the drops can carry charges closer to their maximum limits (Rayleigh or corona limit). It is important to note here that in calculating the maximum charge which can be placed on a drop due to the conduction charging (Equation 1.5), the electric field around the drop is assumed to be uniform and limited by the breakdown strength of air (30 kV/cm). However, in the practical case, the electric field around a spherical drop is neither uniform nor limited by that value. For very small drop sizes, the electric field around the drop might reach much higher values before any noticeable corona discharge. The conduction charging, in turn, might lead to a higher charge (equivalent to the corona limit) rather than that given in Figures 7.11 and 7.12.

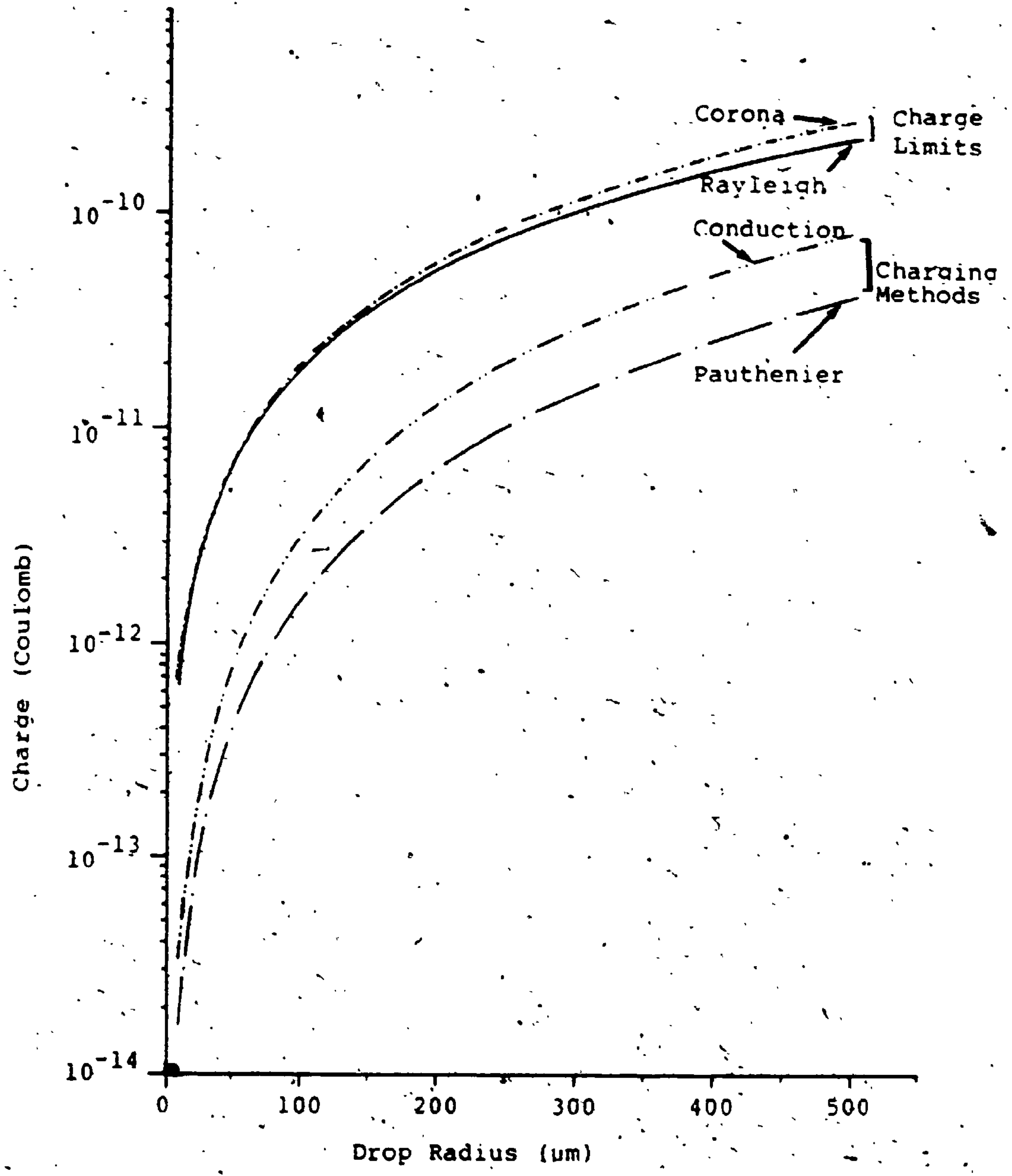

Figure 7.11 The Maximum Charge on a Spherical Drop Due to Different Charging Methods and Charge Limits at T = 20°C and P = 760 mm.Hg.

7.6 Conclusions

This part of the study summarizes an attempt to clarify the instability-corona charge limit of a charged liquid drop. The results show that this process is very complex so that one should specify all the conditions of the drop radius, the liquid surface tension and the air pressure, temperature and relative humidity in order to determine which charge limit prevails and restricts the possible charge level attainable. The results also show remarkable agreement with the experimental observations of other investigators. The theoretical predictions are also used to explain some experimental results previously reported in the literature. From the results of this chapter one can conclude that:

1- The spherical drop assumption can be used only for small drop sizes ($R \leq 50\mu m$). For large drop sizes, or for high levels of external forces, this assumption is not valid. The numerical results show that assuming a spherical drop shape under such conditions, changes the results significantly.

2- At NTP and for standard relative humidity, the stability limit, for water drops, is always less than the corona limit and hence it determines the maximum charge limit for all the drop radii under consideration (10-360 µm).

3- Decreasing the air pressure or increasing the air temperature or the relative humidity enhances the possibility of corona discharges.

In the case of a spheroidal drop, the assumption of the smaller radius of curvature of the drop as being more susceptible to corona than the rest of the drop surface, may not be valid for all the drop deformations or for all the drop radii. A further study on the onset electric field every where around the drop surface is recommended.

CHAPTER EIGHT

CONCLUSIONS AND SUGGESTIONS FOR FUTURE WORK

Based on the results and discussions presented in this thesis, the following conclusions and suggestions for future studies are presented.

8.1 Breakup Model

An analytical model was developed for a conductive spherical drop to predict the final state just after the breakup for single sibling disintegration. This model was also extended to cover the multi-sibling instability assuming tree-like secondary breakups. For a spherical drop unaffected by any external force, the model predicts a single sibling disintegration. The sibling, under such conditions, carries about 25% of the initial mass and 40% of the initial charge. These results are in good agreement with the experimental observations reported by Abbas and Latham [5]. The final minimum potential energy at the breakup, under such a condition, was also shown to be about 75% of the initial energy. The difference between the initial and the final energy is believed to be converted to kinetic energy during the breakup. Part of this energy is also believed to be dissipated by a combination of viscous resistance to the drop motion and hydrodynamic and acoustic wave generation.

In this model, the effect of the external forces was also considered through a modification of the liquid surface tension used in the Rayleigh limit equation. Since the modified surface tension was proven to be a function of the drop size, the final minimum energy might exist at a sibling mass ratio different than that calculated for a drop unaffected by any external force. The results of the breakup model show that when the minimum final energy is satisfied at any value of the sibling mass ratio greater than 11.1%, a single sibling breakup occurs. For all the values of the sibling mass ratios less than 11.1%, the sibling is unstable and divides again in a tree-like secondary breakup leading to the multi-sibling case. In this model, the number of stable siblings at any sibling mass ratio is also predicted.

The validity of this model was verified experimentally. Charged droplets of water were formed at the tip of a capillary tube raised to high potential and subjected to controlled external electric fields. The nozzle characteristics were tested to identify the different ejection modes. Under some conditions of charging potential and electric field at the nozzle tip, breakup of the ejected droplets resulted. These droplets were collected on water sensitive paper and then examined under a microscope at 80X magnification. The results of the collected number of siblings at each range of the sibling mass ratio showed good agreement with the analytical model and supported the validity of the concept of tree like secondary breakups.

In this model, it was assumed that all the droplets were spherical. This assumption is valid only for droplet radii ≤ 50 µm (Chapter 6 and Chapter 7). For larger drop sizes, the effect of the external forces on the secondary disintegration should be considered. Using the general stability equations introduced in Chapter 5 may lead to more accurate results for non-spherical droplets. This model was also restricted to conductive liquids so that the droplets just before disintegration would be at the same electrical potential. To progress further in this problem, it would be necessary to study the breakup of non-conducting liquid droplets to take into account the effect of the ion mobility on the charge distribution on the drop surface. A further experimental study that employs more accurate instrumentation is also suggested to evaluate the number of siblings for very low sibling mass ratios.

8.2 Instability of Liquid Drops Subjected to Exter[illegible] Forces

Because the Rayleigh limit is only valid for spherical droplets unaffected by any external force, general equations describing the drop stability were introduced (Eq. 5.21 and Eq. 5.27) for both prolate and oblate spheroidal shapes and for liquid drops affected by various types of forces such as gravitional, electrical and aerodynamic force. These equations were proven to be the general form of the Rayleigh limit equation and Taylor's stability equations. In developing these equations, it was assumed that the drop retained a spheroidal shape until the onset of instability. It was also assumed that the pressure equilibrium was satisfied at the pole and the equator of the drop.

The analysis of these equations showed that, for a certain surface tension of the liquid and for known external forces acting on the drop, there is only one equilibrium deformation (aspect ratio) for a given drop charge. Increasing the charge on the drop leads to an increase in its deformation. However, for more than a certain charge on the drop (the maximum charge limit), the results showed that no deformation can satisfy the equilibrium of such a drop. This charge limit was considered the stability limit of the drop and the corresponding deformation was also considered as the maximum deformation for the given combination of the external forces.

From the analytical evaluation of these stability equations, it was concluded that the Rayleigh limit can be used in approximating the drop stability limit only for small drop sizes ($\leq$ 50 μm) and for very low external electric fields. For larger drop sizes or high electric fields, the Rayleigh limit is no longer valid. For certain combinations of external forces, the evaluation of the stability equations for the static case (Eq. 5.21 and Eq. 5.27) also showed that the stability limit might be higher than the Rayleigh limit. However, this finding needs to be re-evaluated while taking the transient parameters of the dynamic case into account. These parameters should include the drop vibration as the drop changes its shape. For this case, the stability equations (5.21 and 5.27) must be modified and expressed as time dependent equations.

8.3 The Charge Limit of Liquid Droplets Due to the Electron Avalanches and Surface Disruptions

An analytical study, based on Hartmann's formula, was performed to predict the maximum charge that a liquid drop can retain without losing its charge by electron avalanches or by redistributing the charge among smaller droplets through surface disruption. The effects on both the corona onset field and the stability limit of the liquid surface tension, air temperature, pressure and relative humidity were considered. Two separate cases were investigated in this study. The first represented the case of a spherical drop unaffected by any external force, while the second corresponded to the case of a drop distorted to a spheroidal shape due to the influence of preset combinations of external forces. The results of this analysis showed that for water drops of 10-360 um radius at normal temperature, pressure and relative humidity, surface instability prevails and restricts the maximum charge limit. For lower air pressures, higher air temperatures or higher relative humidity, the possibility of corona discharges (electron avalanches) is possible. The results of this analysis also showed that the assumption of a spherical drop can be used only for smaller drop sizes ($R < 50$ um) while for large drop sizes, or for high levels of external forces, this assumption is not valid,

To further verify the results of the analysis, it is strongly recommended to conduct an experimental study on the effect of air pressure, temperature and relative humidity on the threshold separating the two charge limits. Although difficult, this could perhaps be accomplished by modifying English's set-up [30] to allow fine control of these parameters. In this experiment, capillary tubes of different cross sections are required to change the drop sizes. For accurate estimation of the drop size, a stereo-microscope of high magnification attached to a camera is also needed. This experiment also requires a corona detector that does not interrupt the electric field around the drop. This can possibly be accomplished by using a modified radio receiver that detects the corona (high frequency) signals. Such an experiment would also be most helpful in investigating the maximum charge to mass ratio of a drop under different practical and industrial conditions.

8.4 Highlights of the Main Conclusions

In summary to the previous discussion, the following main objectives were met;

1- An analytical model has been introduced to predict the end state of a disrupted conductive drop on the basis of the conditions of the initial drop just before the breakup.

2- The demarcation between the modes of single sibling and multi-sibling breakup has been clarified.

3- The Rayleigh limit equation has been modified to take into account the effect of the external forces on the drop instability for the static case.

4- Using Hartmann's formula for the corona onset, the thresholds separating the two charge limits, namely the drop breakup and the electron avalanches, have been determined.

The following conclusions were also drawn:

1- For a conductive spherical drop unaffected by any external force, the single sibling disintegration is the most probable breakup.

2- For a conductive spherical drop, the single sibling exists for all the values of sibling mass ratios greater than 11.1%. For all the values less than this, multi-sibling disintegration is favoured.

3- The multi-sibling breakup occurs in a tree-like disintegrations.

4- The Rayleigh limit equation is only valid for very small drop size ($R \leq 50$ µm) and for low external force

191

levels.

5- The external forces may have a dramatic effect on the drop charge limit and in turn, the modified stability equations (Eq. 5.21 and Eq. 5.27) should be used to estimate the maximum charge limit of the drop.

6- For the idealized static case and under certain combinations of external forces, the Rayleigh limit is no longer the upper charge limit.

7- At NTP and for standard relative humidity, the stability limit for both spherical and deformed water drops, is always less than the corona limit.

8- Decreasing the air pressure or increasing the relative humidity enhances the possibility of corona discharges.

192

APPENDIX I

RESULTS OF THE THEORETICAL MODELS FOR LOW ION MOBILITY CONDITION

In this analysis, the case of low ion mobility was considered by using the charge distribution introduced by Roth and Kelly [19] i.e. constant average surface charge density. To take into account the energy conversion and losses during the breakup, the kinetic energy term in Roth and Kelly's model was modified. This modified term was calculated by representing the charge on a distorted drop by two charge centers. The distance between these charge centers (dc) was calculated for three different cases. The first represents the case of two charge centers separated by a distance (dc) equal to the initial drop radius R_0. In the second case, (dc) was taken to be equal to the sum of the radii of the two droplets after the breakup, i.e. R_1+R_2. To calculate the distance between the charge centers in the third case, the electric force of repulsion was assumed to be balanced by the surface tension force on a disc separating the two portions of a spherical drop before the breakup. In these three cases, both the single sibling and the multi-sibling breakups were considered.

To calculate the ratio E_f/E_i, the following equations are used

$$E_i = 4\pi\nu R_0^2 + \frac{Q_0^2}{8\pi\epsilon_0 R_0}$$

where R_0 is the initial drop radius and Q_0 is calculated from the Rayleigh limit equation. The total final energy can be calculated as

$$E_f = 4\pi\nu\,(R_1^2 + n.R_2^2) + \frac{Q_1^2}{8\pi\epsilon_0 R_1} + \frac{nQ_2^2}{8\pi\epsilon_0 R_2} + KE$$

where R_1 and R_2 are the residual drop and the sibling radii respectively, (n) is the number of siblings and KE is the kinetic energy term. The values of Q_1 and Q_2 are calculated from the assumption that the surface charge density is constant, i.e.

$$\frac{Q_1}{Q_0} = \frac{\text{surface area of the residual drop}}{\text{surface area of the initial drop}}$$

and

$$\frac{Q_2}{Q_0} = \frac{\text{surface area of the sibling}}{\text{surface area of the initial drop}}$$

The kinetic energy term was calculated using the formula given by Roth and Kelly [19] by substituting the distance calculated using the catenary assumption with the distance dc calculated from the following three cases.

Case 1

The center of charge is assumed to be the same as the center of gravity of hollow portions of a sphere i.e. $dc = R_0$. This case also represents the condition of very small sibling separating from the surface of a sphere.

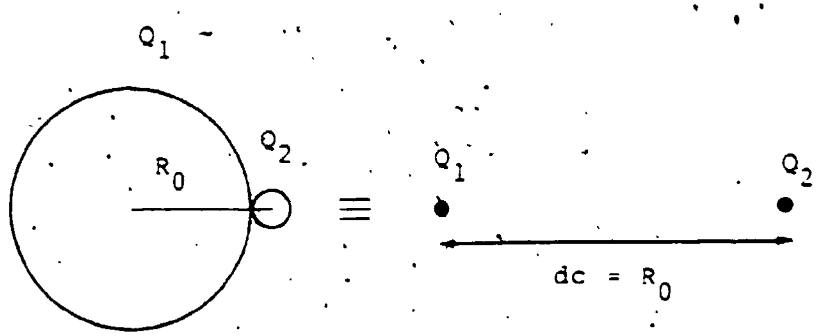

Case 2

The distance separating the two charge centers equals to the summation of the two droplets' radii.

$$dc = R_1 + R_2$$

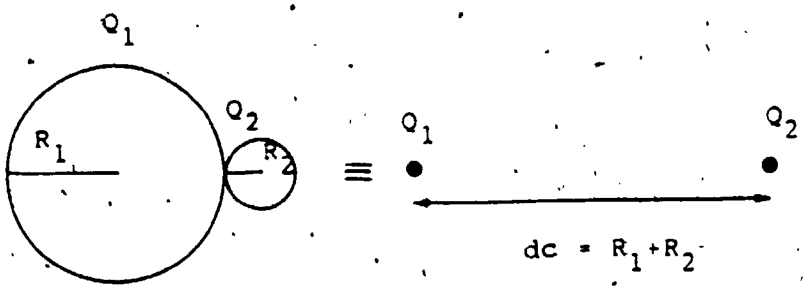

Case 3

In this case the electrical repulsion force is assumed to be balanced by the surface tension force on a disc of radius (r), where $r = R_0 \sin\theta$. The general treatment of this condition is introduced as follows;

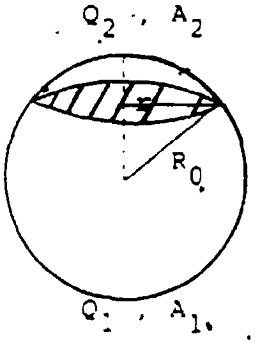

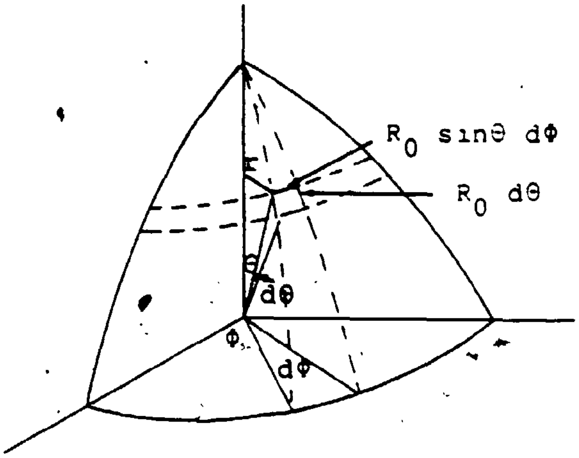

The area of a sphere (A) $= \int_0^{2\pi}\int_0^{\pi} R_0^2 \sin\theta \, d\theta \, d\phi$

$= 4\pi R_0^2$

The area of the spherical cap (A_2) $= \int_0^{2\pi}\int_0^{\Phi} R_0^2 \sin\theta \, d\theta \, d\phi$

$= 2\pi R_0^2 [1-\cos\theta]$

$Q_2/Q_0 = A_2/A = [1-\cos\theta]/2$

$Q_1/Q_0 = [1+\cos\theta]/2$

$\theta = \cos^{-1} [2Q_1/Q_0 - 1]$

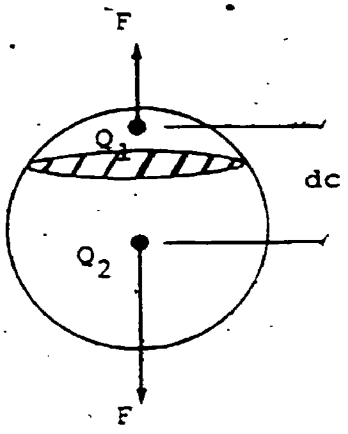

The electric force $= Q_1 \cdot Q_2 / 4\pi\varepsilon\ dc^2$.

$$= \frac{[0.25\ (1+\cos\theta)\ (1-\cos\theta)\ Q_0^2\ ]}{4\pi\varepsilon\ dc^2}$$

$$= \frac{[(1-\cos\theta)\ (1+\cos\theta)\ 64\pi^2\varepsilon\nu R_0^3\ ]}{16\pi\varepsilon\ dc^2}$$

Since this force is balanced by the surface tension force on a disc of radius $r = R_0 \sin\theta$, therefore,

the surface tension force $= 2\pi\nu\ R_0 \sin\theta$

Then equating the two forces gives

$$dc = R_0\ [2\ (1-\cos\theta)\ (1+\cos\theta)\ /\ \sin\theta]^{\frac{1}{2}}$$

Figure A.I.1 presents a sample of the results obtained from these models for the case of single sibling breakup. It shows that the total energy after the breakup is higher than the initial energy. Since no external force nor energy source is assumed, these results show that these representations of the case of low ion mobility do not satisfy the conservation of energy.

For the multi-sibling case, following Roth and Kelly's assumptions, the siblings are assumed to be identical and to be emitted simultaneously in geometrical regular patterns. The numerical results of the multi-sibling breakup showed that the percentage ratio of E_f/E_i increases as the number of sibling increases.

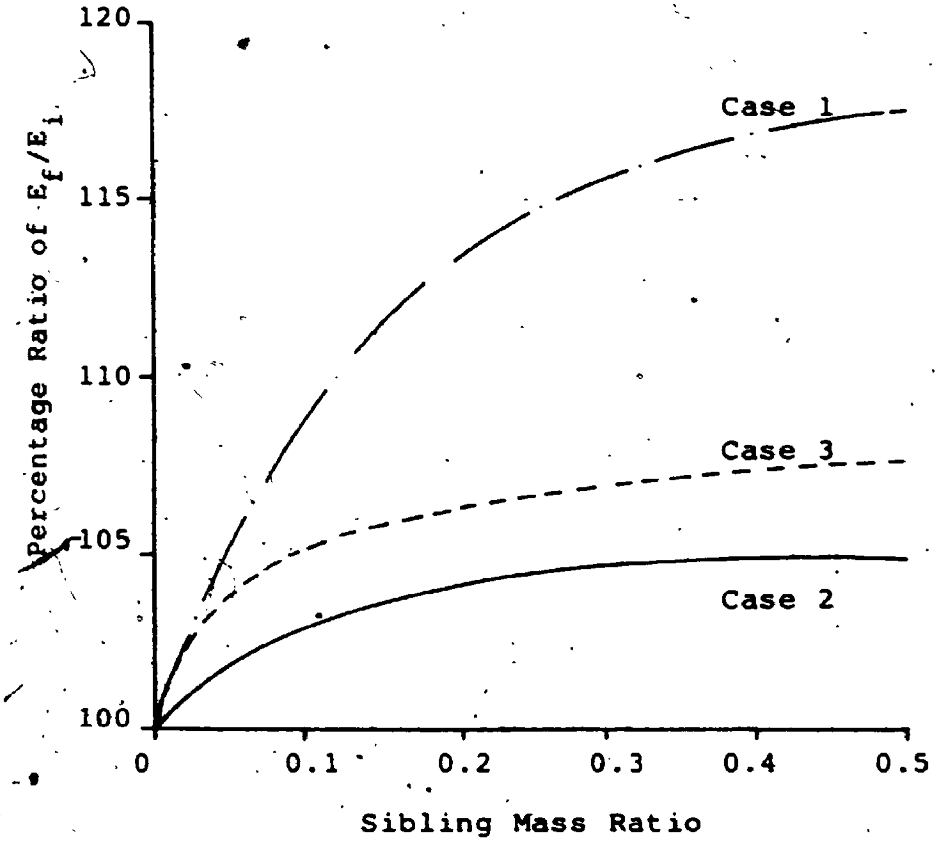

Figure A.I.1 The Percentage Ratio of the Total Final Energy to the Initial Energy as a Function of the Sibling Mass Ratio (for the Single Sibling Case)

APPENDIX II

RESULTS OF THE PRELIMINARY EXPERIMENTS

A II.1 The Characteristics of the Drops Ejected from the Nozzle Under Different Charging Voltage for Zero Ring Voltage

Charging voltage kV	Drop diameter µm	Dripping time sec	Spreading factor	Reproducibility no. of siblings	Reproducibility no. of samples
3.0	1065-1088 (1070)	33.5-36.0 (34.5)	2.46	0	60
3.1	997-1020 (1000)	30.5-33.0 (31.5)	2.36	0	60
3.2	884-907 (900)	26.5-28.5 (27)	2.23	0	60
3.3	741-768 (760)	20.5-24.1 (22)	2.36	0	60
3.4	511-530 (515)	10.5-13.5 (12.5)	2.22	0	60
3.42	340-363 (350)	6.5-7.5 (7)	2.21	0	60
3.43	218-255 (240)	3.35-3.75 (3.5)	2.23	0	32
				1	18
				2	7
				* 5	2
				* 7	1
3.44	122-169 (142)	1.6-1.9 (1.7)	2.19	0	9
				1	28
				2	18
				4	3
				5	1
				* 8	1

@@@@@@@@@@@@@@@@@@@@@@@@@@@@ SPRAY @@@@@@@@@@@@@@@@@@@@@@@@@@@@@

* Outliers

\+ Data in parentheses represent the mean values for the ranges given above.

A II.2 The Characteristics of the Drops Ejected from the Nozzle Under Different Ring Voltage for Charging Voltage = 3.42 kV

Ring voltage V	Drop diameter µm	Dripping time sec	Spreading factor	Reproducibility	
				no. of siblings	no. of samples
00	341-362 (345)	6.8-7.1 (6.9)	2.21	0	60
-50	317-330 (323)	6.5-6.8 (6.6)	2.19	0	43
				1	16
				2	1
-60	306-317 (316)	6.4-6.6 (6.47)	2.23	0	28
				1	26
				2	4
				* 5	1
				* 8	1
-70	294-317 (308)	6.2-6.4 (6.3)	2.24	0	7
				1	26
				2	19
				3	4
				4	2
				* 7	1
				* 8	1
-80	294-306 (297)	5.8-6.1 (6.0)	2.31	1	8
				2	13
				3	28
				4	7
				5	1
				* 8	2
				*12	1

@@@@@@@@@@@@@@@@@@@@@@@@@@@ SPRAY @@@@@@@@@@@@@@@@@@@@@@@@@@@@

* Outliers

\+ Data in parentheses represent the mean values for the ranges given above.

A II.3 The Characteristics of the Drops Ejected from the Nozzle Under Different Ring Voltage for Charging Voltage = 3.33 kV

Ring voltage V	Drop diameter µm	Dripping time sec	Spreading factor	Reproducibility	
				no. of siblings	no. of samples
0	750-770	21.8-22.3	2.35	0	60
	(765)	(22.3)			
-100	590-640	17.2-19.4	2.29	0	60
	(625)	(18.2)			
-200	370-415	9.8-10.7	2.24	0	59
	(400)	(10.5)		1	1
-220	325-370	8.7-9.5	2.27	0	51
	(350)	(9.2)		1	8
				2	1
-230	305-345	7.9-8.6	2.23	0	49
	(330)	(8.4)		1	8
				2	3
-240	290-325	7.1-7.6	2.28	0	53
	(310)	(7.4)		1	7
-250	270-305	5.9-6.7	2.26	0	37
	(285)	(6.4)		1	28
				2	5
-260	240-270	5.3-5.8	2.19	0	16
	(255)	(5.5)		1	32
				2	9
				3	3

TABLE AII.3 (Continue)

Ring voltage V	Drop diameter µm	Dripping time sec	Spreading factor	Reproducibility	
				no. of siblings	no. of samples
-270	205-250 (230)	4.4-4.9 (4.6)	2.26	0	12
				1	26
				2	11
				3	5
				4	4
				6	1
				* 10	1
-280	180-210 (200)	3.2-3.7 (3.5)	2.22	0	3
				1	31
				2	11
				3	6
				4	3
				5	3
				6	2
				* 12	1
-290	150-190 (175)	2.4-2.7 (2.6)	2.23	1	7
				2	9
				3	23
				4	8
				5	7
				6	4
				* 10	2

@@@@@@@@@@@@@@@@@@@@@@@@@@ SPRAY @@@@@@@@@@@@@@@@@@@@@@@@@@

* Outliers

\+ Data in parentheses represent the mean values for the ranges given above.

A II.4 The Characteristics of the Drops Ejected from the Nozzle Under Different Ring Voltage for Charging Voltage = 3.46 kV

Ring voltage V	Drop diameter µm	Dripping time sec	Spreading factor	Reproducibility	
				no. of siblings	no. of samples
@@@@@@@@@@@@@@@@@@@@@@@@@@@@@@ SPRAY @@@@@@@@@@@@@@@@@@@@@@@@@@@@@@					
310	113-136	1.5-2.3	2.23	** 6	4
	(120)	(1.8)		** 8	7
				**10	33
	(The siblings were too small to be measured)			**11	9
				**12	5
				**16	2
320	226-250	3.1-3.9	2.28	2	13
	(234)	(3.6)		3	21
				4	9
				6	7
				7	5
				8	4
				* 12	1
330	338-365	5.4-6.7	2.31	0	60
	(350)	(6.0)			
350	530-566	10.3-12.5	2.26	0	60
	(550)	(11.0)			
400	694-742	15.1-17.7	2.41	0	60
	(710)	(16.0)			

---

* Outliers

** Refused

\+ Data in parentheses represent the mean values for the ranges given above.

APPENDIX III

SAMPLE CALCULATIONS OF THE ERROR IN MEASURING THE SIBLING MASS RATIO

For a typical sample, the collected droplets were 60, 10, 18 and 4 graticule lines corresponding to diameters of 225, 37.5, 67.5, 15 µm respectively. The error in measuring their diameters based on half a division resolution = ±0.5/d and the maximum error due to the use of w.s.p. = ±(2.31-2.25)/2.25 = 0.027.

Therefore, the total error in measuring the drop radius = 0.5/d + 0.027 and in turn the error in measuring the drop volume = 3(0.5/d + 0.027)

Then

Drop diameter	60	10	18	4
R^3	27000	125	729	8
Error in drop radius	0.035	0.077	0.055	0.152
Error in R^3	0.106	0.231	0.164	0.456
Absolute error in R^3	2862	28.87	119.8	3.648

$\Sigma R_s^3 = 8 + 729 + 125 = 862$

$\Sigma R_o^3 = 862 + 27000 = 27862$

absolute error in R_s^3 = 28.87 + 119.8 + 3.648 = 152.3

absolute error in R_o^3 = 2862 + 152.3 = 3014.3

Then

the total % age error in R_s^3/R_o^3 =

(152.3/862 + 3014.3/27862) * 100 = 28.5%

APPENDIX IV

FLOW PAST A LIQUID DROP

An accurate knowledge of the terminal velocity, and the pressure distribution of a liquid drop was needed for carrying out the calculations of the maximum charge that a drop could carry. The complete physical-mathematical basis for the required characteristics of a falling drop is given by the Navier-Stokes equations of motion for the air flowing past the drop as well as the motion of the liquid inside the drop, subject to the appropriate dynamic and kinematic boundary conditions. An extensive treatment of the theory of low Reynolds number may be found in Happle and Brenner [57]. The non-linearity of the Navier-Stokes equation renders their lution very difficult and only a relatively small number of exact solutions of rather specialized character are known. However, in many cases, the flow is such that reasonable simplifying assumptions regarding its character can be made which result in a less complicated mathematical problem.

The observed flow regimes about a rigid sphere for a continuous fluid were compiled from the work of many previous investigators by Beard [39], as shown in Figure A.IV.1. The flow is seen to progress through a series of transitions from a laminar, symmetrical flow at Reynolds number = 0 to a separated turbulent boundary layer flow with a chaotic wake for Re > 400,000. The flow is apparently quite steady for Re < 300 although it is no longer

Figure A.IV.1 Flow Regimes about a Rigid Sphere in a Laminar Steady Flow.

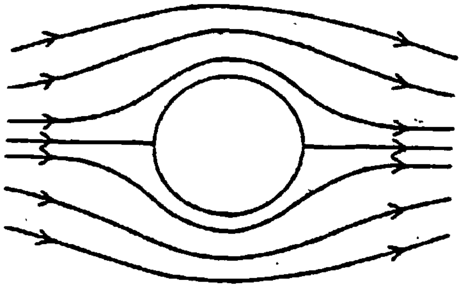

a. Stokes flow (Re = 0)

* Axial and fore-aft. symmetry

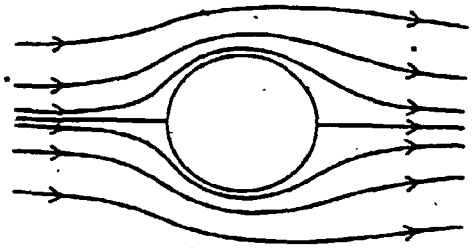

b. Low Reynolds numbers (Re < 20)

* Flow no longer has fore-aft. symmetry

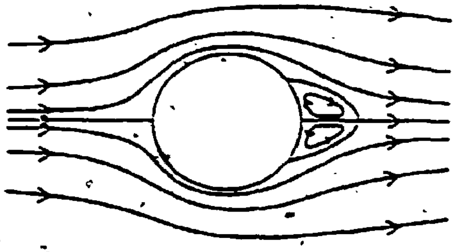

* Separated with enclosed vortex ring

c. Intermediate Reynolds numbers (20 < Re < 200)

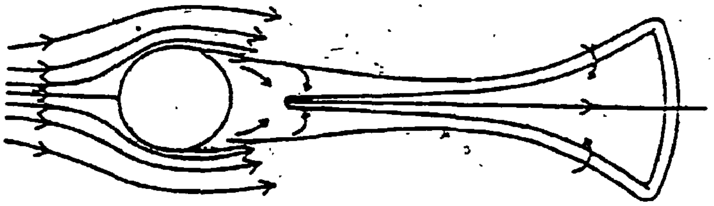

* Vortex loops are formed

d. Moderate Reynolds numbers (200 < Re < 450)

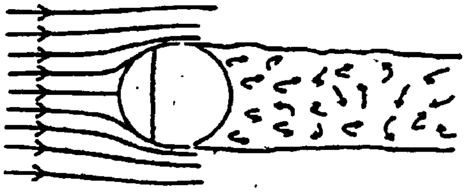

* wake becomes increasingly chaotic at large Re, until Re > 400,000, the onset of turbulent flow

e. Large Reynolds numbers (Re > 450)

axisymmetric above $Re \simeq 200$.

Although the previous flow regimes are actually defined for a sphere, and due to the lack of data about the flow past a spheroidal shape, one may consider that its flow regimes are similar to that given for a sphere with an expectation that the values of the transition Reynolds number may change.

The solution of the Navier-Stokes equations for low, intermediate and moderate Reynolds numbers for both prolate and oblate spheroids will be discussed in the following sections.

Solution for Very Low Reynolds Numbers

The oldest formulation of flow past an obstacle is the so called "Stokes flow". It is defined by the assumption that the inertial effects $\rho\bar{V}e\bar{\nabla}\bar{V}e$ (where $\bar{V}e$ is the relative flow velocity) are negligible in comparison with those of viscosity ($\mu\bar{\nabla}^2\bar{V}e$), or more precisely, the Reynolds number of the flow is very small. A general solution for a spheroid, in spheroidal coordinates, has been reviewed by Happel and Brenner [57], for Stokes flow. The drag force experienced by the spheroid is given by

$$D_f = 6\pi\mu \, V_T^2 \, a_e \, k \qquad \text{A.IV.1}$$

Where a_e is the equatorial radius of the spheroid, (a or b), and k for both oblate and prolate spheroids are given by Eq. 5.18.

Despite a misprint in their expression for k (oblate), Happel and Brenner provided an accurate tabulation of k as a function of the aspect ratio for both oblate and prolate spheroids. The surface pressure distributions for modified Stokes flow past an oblate spheroid were also given as

$$P_{\text{oblate}} = \frac{1}{2} \rho_a Ve^2 \left[1 + \frac{6 \, k(\text{oblate})}{Re} \left(\frac{L^2 + 1}{L^2 + \cos^2\theta} \right) \cos\theta \right] \qquad \text{A.IV.2}$$

and

$$P_{\text{prolate}} = \frac{1}{2} \rho_a Ve^2 \left[1 + \frac{6 \, k(\text{prolate})}{Re} \left(\frac{U^2}{U^2 - \sin^2\theta} \right) \cos\theta \right] \qquad \text{A.IV.3}$$

where Re is the Reynolds number defined as

$$Re = \frac{2\rho_a \, Ve \, a_e}{\mu} \qquad \text{A.IV.4}$$

The unity terms in the previous equations come from consideration of the inertial terms in the Navier-Stokes equations, and for strictly Stokes' flow it is absent.

The case when the inertial effects of the flow are small but not negligible was treated by Oseen [78]. He concluded that Stokes' approximation for the flow field was not uniformly valid throughout but breakdown at a large distance from the obstacle.

Breach [79] modified Eq. A.IV.1 to be used for both oblate and prolate spheroids up to Re of 2. His equation is given by:

$$D_f = 6\pi\mu V_T a_e k \left(1 + \frac{3}{16} Re\, k + \frac{9k^2}{160} Re^2 \ln \frac{Re}{2} \right) \qquad \text{A.IV.5}$$

where k has the same values given by Equation 5.18 for both prolate and oblate spheroids.

Solution for Low and Intermediate Reynolds Numbers

Numerical solution of the Navier-Stokes equation was obtained for axisymmetric flow past single oblate or prolate spheroids at Reynold numbers up to 100 by Masliyah [60-61]. The aspect ratio of spheroids varied between .999 (nearly perfect sphere) and 0.2. For low aspect ratios, the surface pressure and the drag coefficient showed a marked difference from those of a sphere. The appearance of the wake bubble behind a spheroid was also found to be a strong function of the particle shape.

In his study, the variation of the dimensionless frontal stagnation pressures $P_0 = K_I = P/(0.5\rho\ V_e^2)$ with Re for both oblate and prolate spheroids is calculated. Figures A.IV.2 and A.IV.3, show that they differ considerably from each other and from unity, K_1 for an oblate spheroid with aspect ratio = 0.2 was the closest to unity at each Re. This seems to confirm two well observed characteristics of static pitot tubes, namely that the correction factor is large for low Reynolds-numbers and that it varies considerably for different tip shapes [80]. It is important to note here that the modified Stokes solution (Eqs. A.IV.2 and A.IV.3) gives surprisingly close results to the numerical values obtained in his work (Figures A.IV.4 - A.IV.6). The only modification required for calculating the pressure distribution has to be in the velocity term which can be calculated from the drag.

Defining the drag coefficient C_D as

$$C_D = \frac{\text{drag force in the flow direction}}{\text{area normal to the flow direction x kinetic pressure}}$$

then

$$C_D = \frac{2D_f}{\rho_a\ V_T^2\ .\ \pi\ a_e^2} \qquad \text{A.IV.6}$$

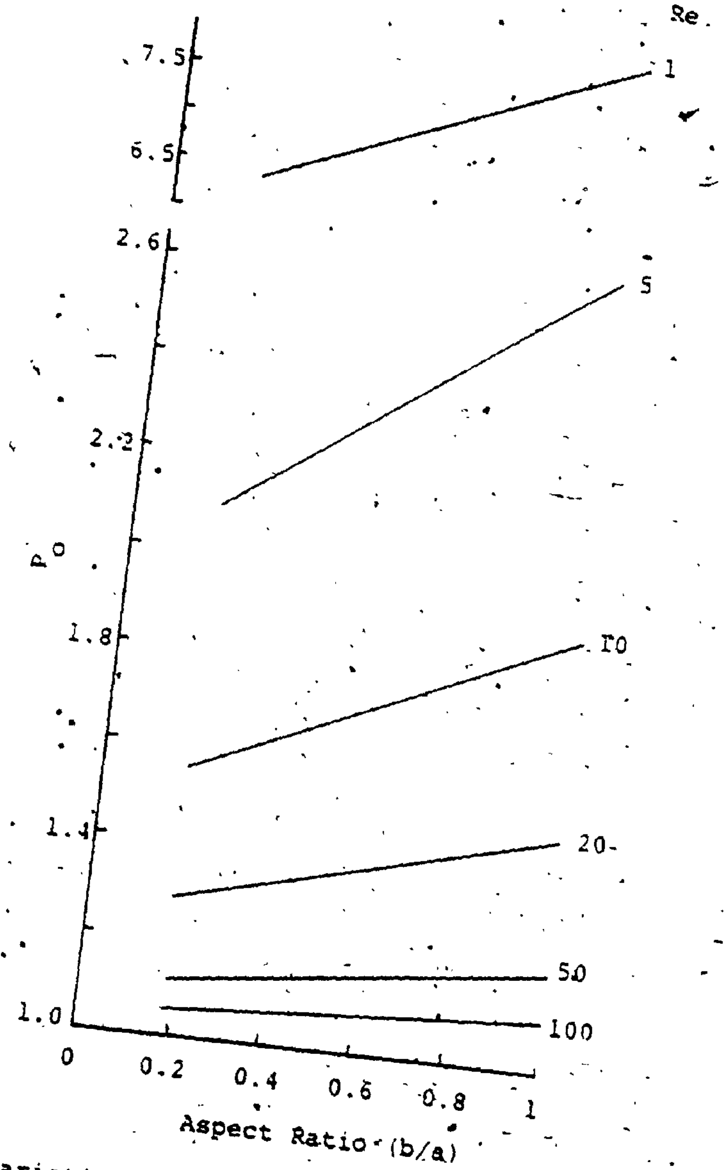

Figure A.IV.2 Variation of Frontal Stagnation Pressure with Aspect Ratio for Oblate Spheroids

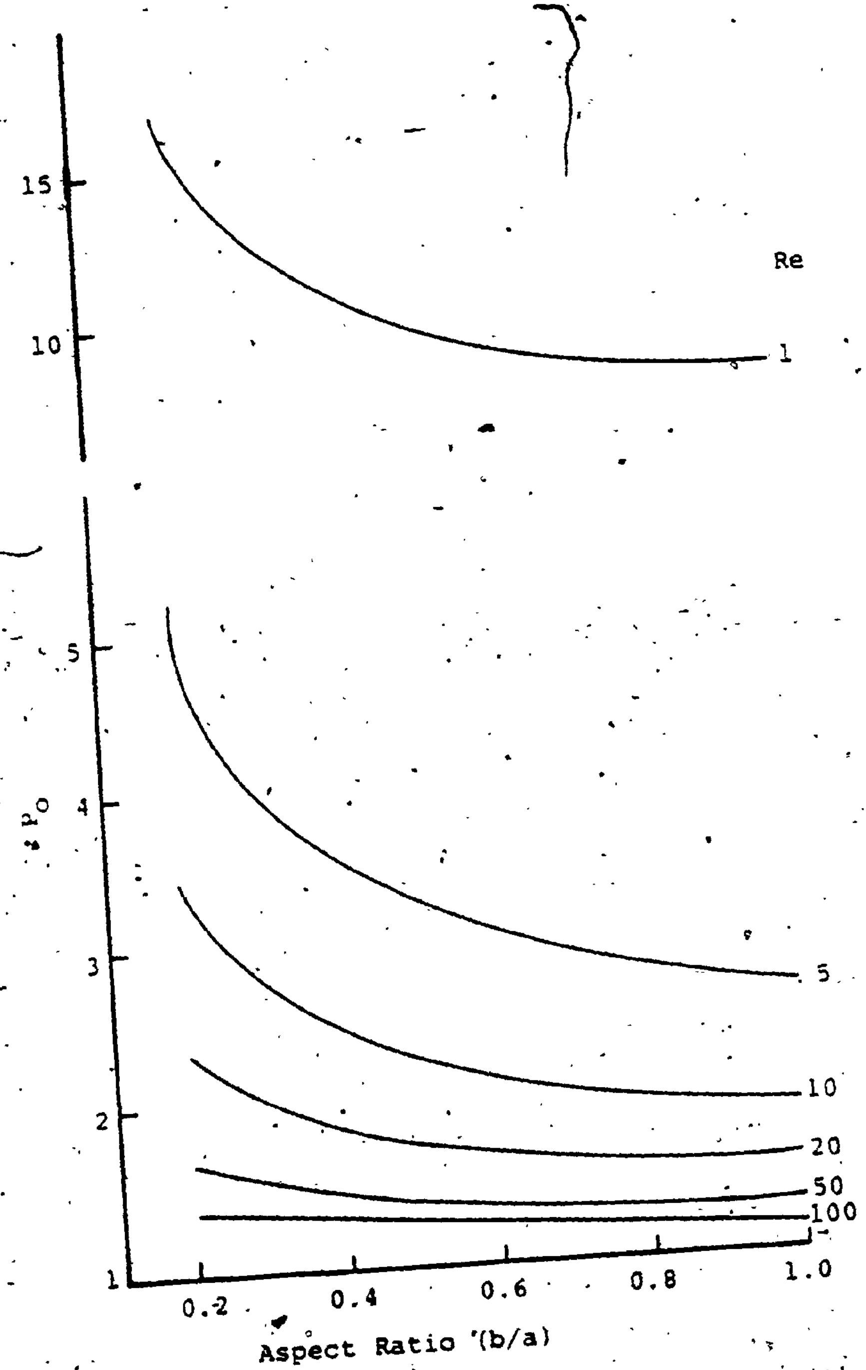

Figure A.IV.3 Variation of Frontal Stagnation Pressure with Aspect Ratio for Prolate Spheroids

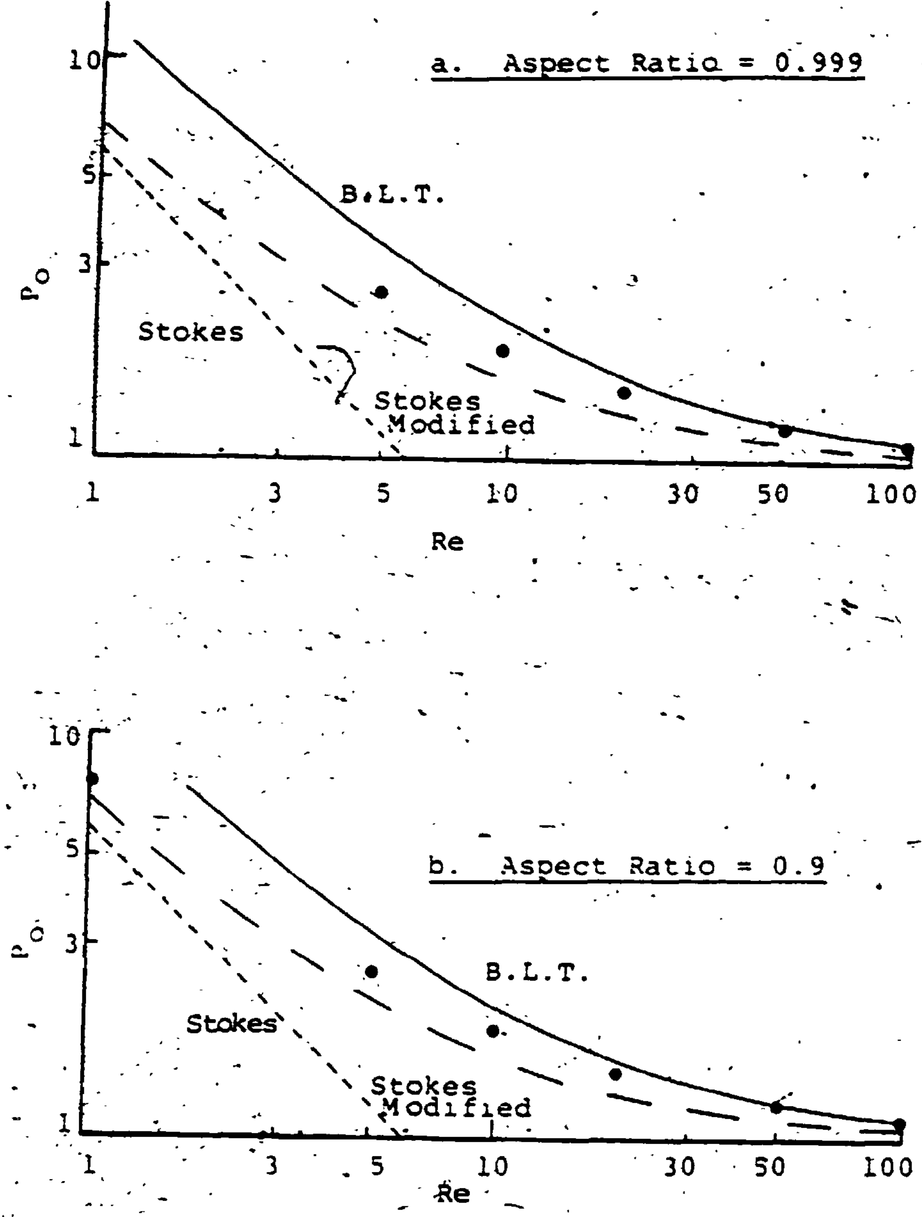

Figure A.IV.4 Variation of the Frontal Stagnation Pressure with Reynolds Number for Oblate Spheroids of High Aspect Ratio

B.L.T. Boundary Layer Theory

● Masliyah Results

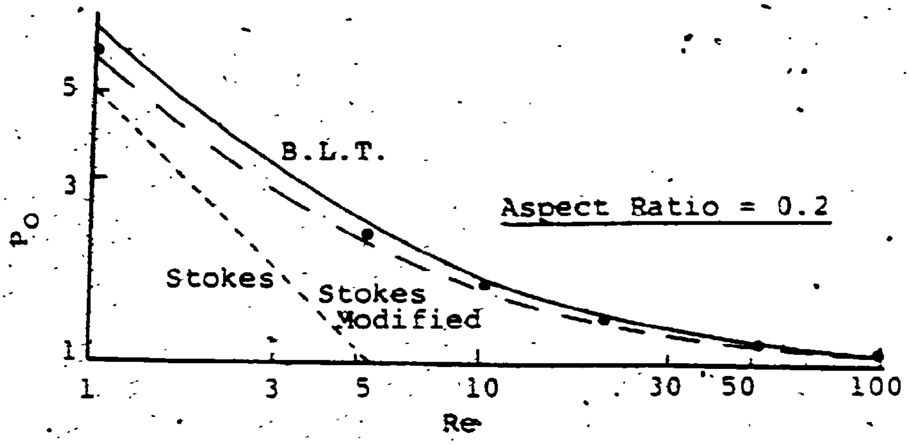

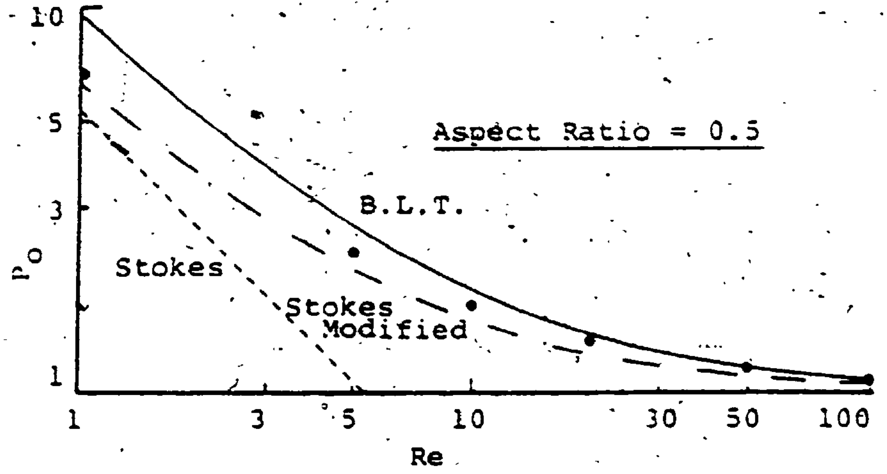

Figure A.IV.5 Variation of the Frontal Stagnation Pressure with Reynolds Number for Oblate Spheroids of Low Aspect Ratio

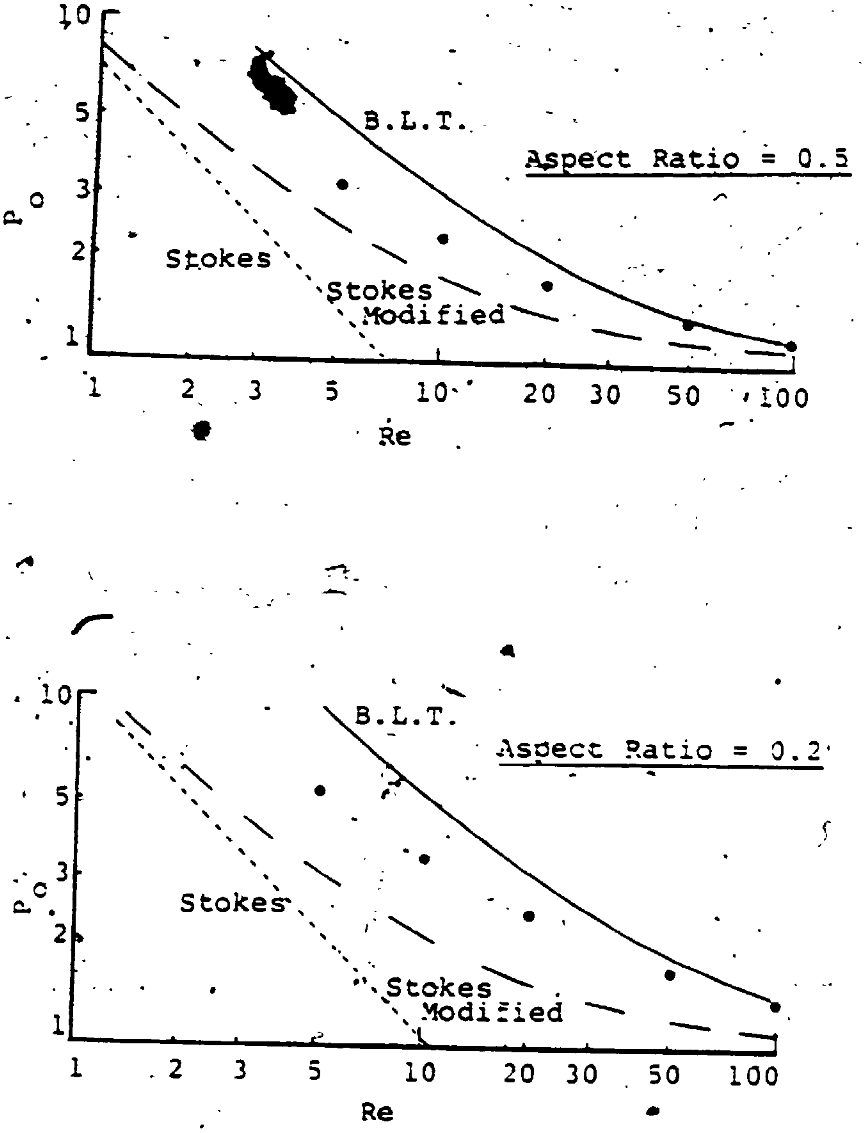

Figure A.IV.6 Variation of the Frontal Stagnation Pressure with Reynolds Number for Prolate Spheroids of Low Aspect Ratio

The variation of the drag coefficient with Reynolds number for various aspect ratios of both an oblate and a prolate spheroids as calculated by Masliyah [61] are given in Figures A.IV.7 and A.IV.8. Figure A.IV.7 shows that the effect of the aspect ratio in the drag coefficient is very small in the case of an oblate spheroid. For simplicity C_D was approximated in the present work with respect to the Reynolds number by fitting a linear relation through his results. The used formula is

$$\log C_D = 1.3 - 0.65 \log Re \qquad \text{A.IV.7}$$

where the constants are calculated from the Stokes approximation at Re = 1 and the potential flow approximation, which will be discussed in the following section, at Re = 100.

For a prolate spheroid, the effect of the aspect ratio seems to be more important. The simplified formula for the drag coefficient in this case is

$$\log C_D = H - \left[\frac{H - 0.05\,(a/b)}{2}\right] \log Re \qquad \text{A.IV.8}$$

where

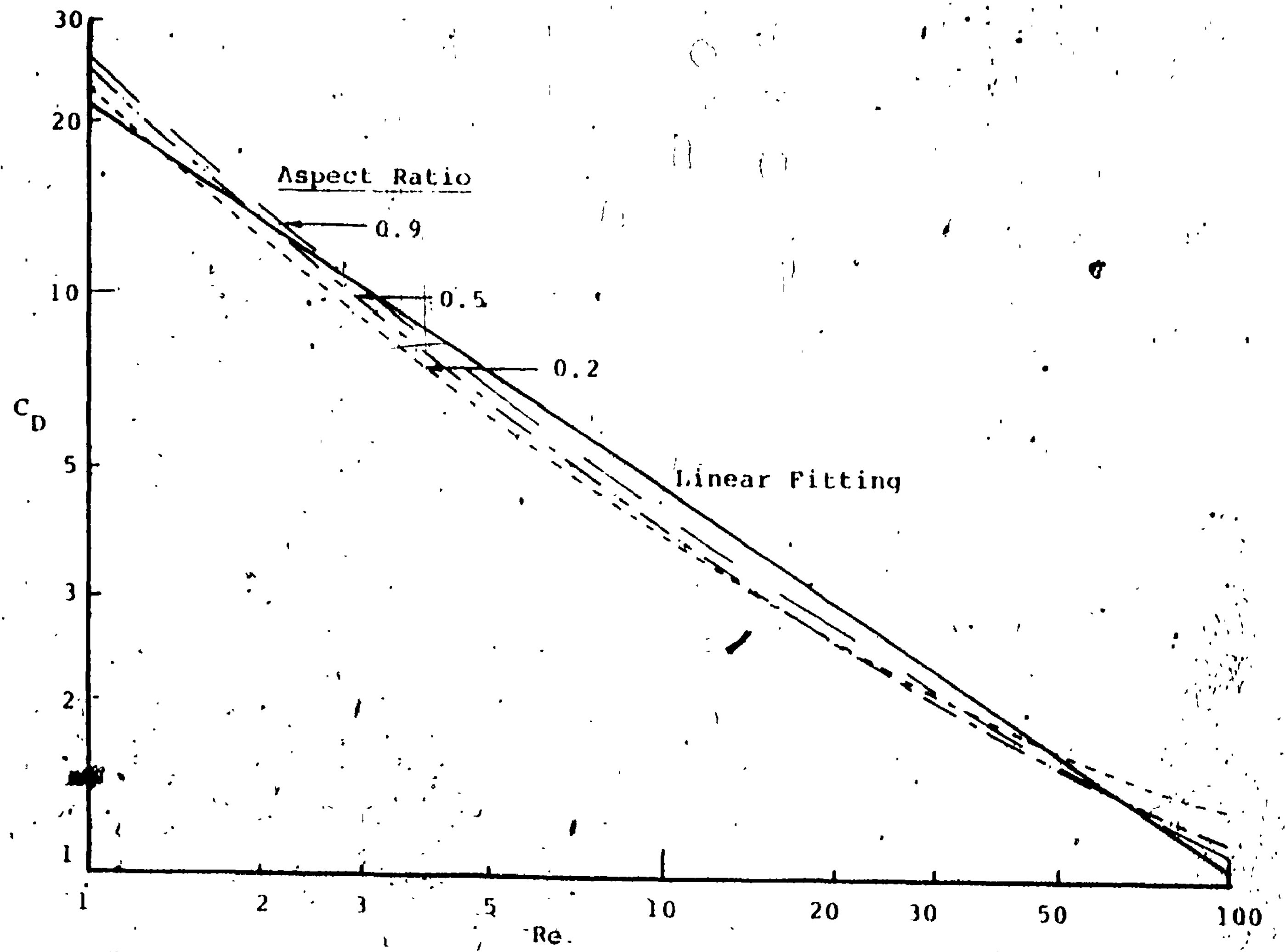

Figure A.IV.7 Variation of the Drag Coefficient with Re for Various Aspect Ratios of an Oblate Spheroid

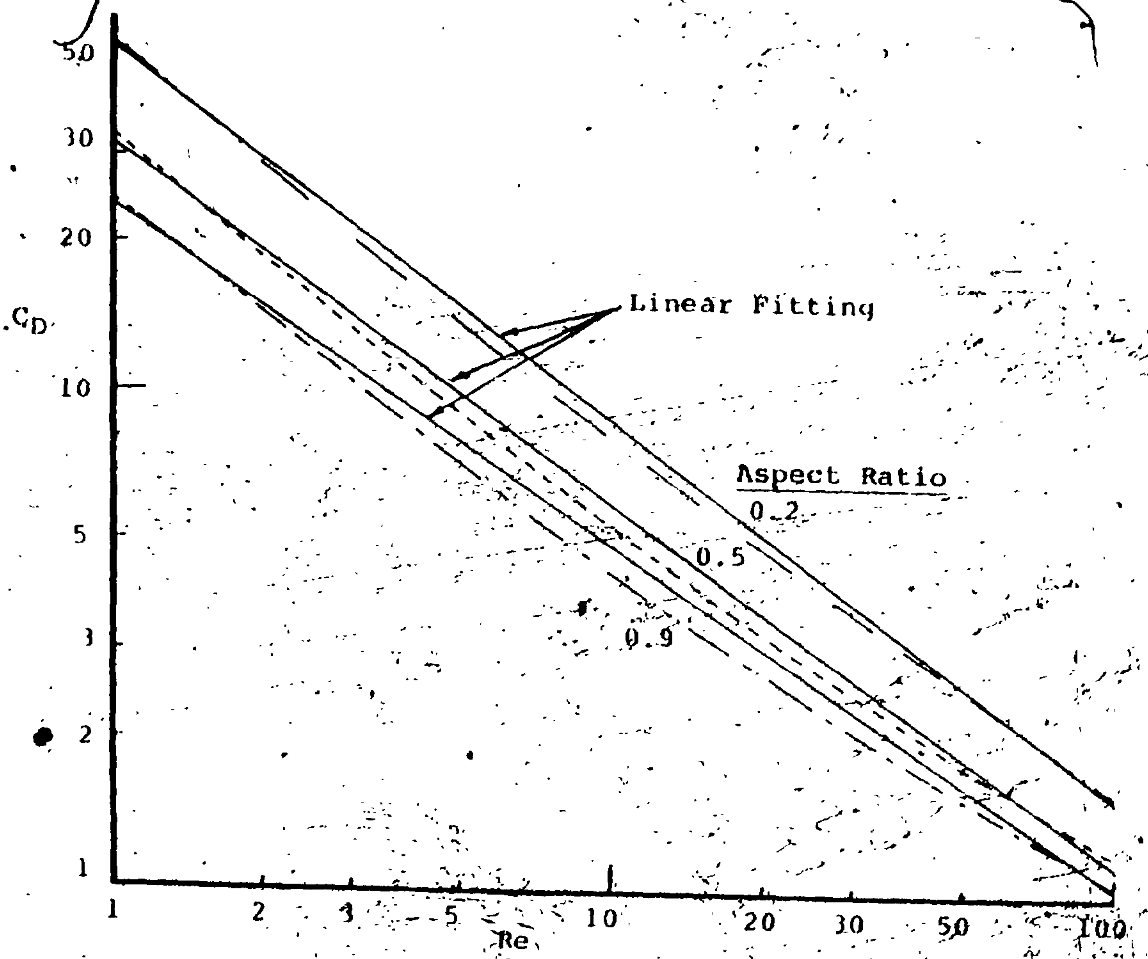

Figure A.IV.8 Variation of the Drag Coefficient with Re for Various Aspect Ratios of a Prolate Spheroid

$$H = \log(22 + 6a/b) \qquad \text{A.IV.9}$$

The approximate values calculated by Equation A.IV.7 and Equation A.IV.8 are also shown in Figures A.IV.7 and A.IV.8 respectively.

Solution for High Reynolds Numbers

At higher Reynolds numbers, Masliyah [61] used the boundary layer theory and the potential flow solution for spheroids to develop his expressions for the surface pressure distribution. For an oblate spheroid, it is given as

$$P_{\text{oblate}} = \frac{1}{2}\rho_a V_T^2 \left[1 - \frac{\sin^2\theta}{(L^2+\cos^2\theta)(L-(L^2+1)\cot^{-1}L)^2} \right]$$

A.IV.10

and for a prolate spheroid the pressure distribution becomes

$$P_{\text{prolate}} = \frac{1}{2}\rho_a V_T^2 \left[1 - \frac{\sin^2\theta}{(U^2-\cos^2\theta)(U-(U^2-1)\coth^{-1}U)^2} \right]$$

A.IV.11

Although the boundary layer theory is strictly applicable for very high Reynolds numbers, Masliyah showed that its results were very close to the numerical values for both prolate and oblate spheroids at Re ≈ 100, (Figures

A.IV.4-A.IV.6 and A.IV.9).

Internal Circulation Effect

The mode of internal circulation in liquid drops falling in a gas was discussed by McDonald [35]. He showed that when the boundary of any airflow is solid, the condition of no slip for real fluids implies that the air in contact with the boundary is at rest relative to that boundary. But when the boundary is the surface of a liquid, the shear stresses exerted by the ambient air would in turn induce some sort of internal circulation.

The problem of the internal circulations for the case of a liquid sphere moving through a dissimilar fluid for vanishingly small Reynolds number, Stokes flow, was examined theoretically by Bond [81]. His results show that the development of internal circulation does not depend on the Reynolds number but rather on the relative viscosity of the interior and the exterior fluids. Rybezynski [82] gave a solution for the magnitude of the drag force in terms of Stokes drag on a rigid sphere as

$$D_f = D_s \ (1 - \mu_{ex}/3\mu) \qquad \text{A.IV.12}$$

where the correction term is seen to be proportional to the viscosity ratio. Consequently, the assumption of a rigid

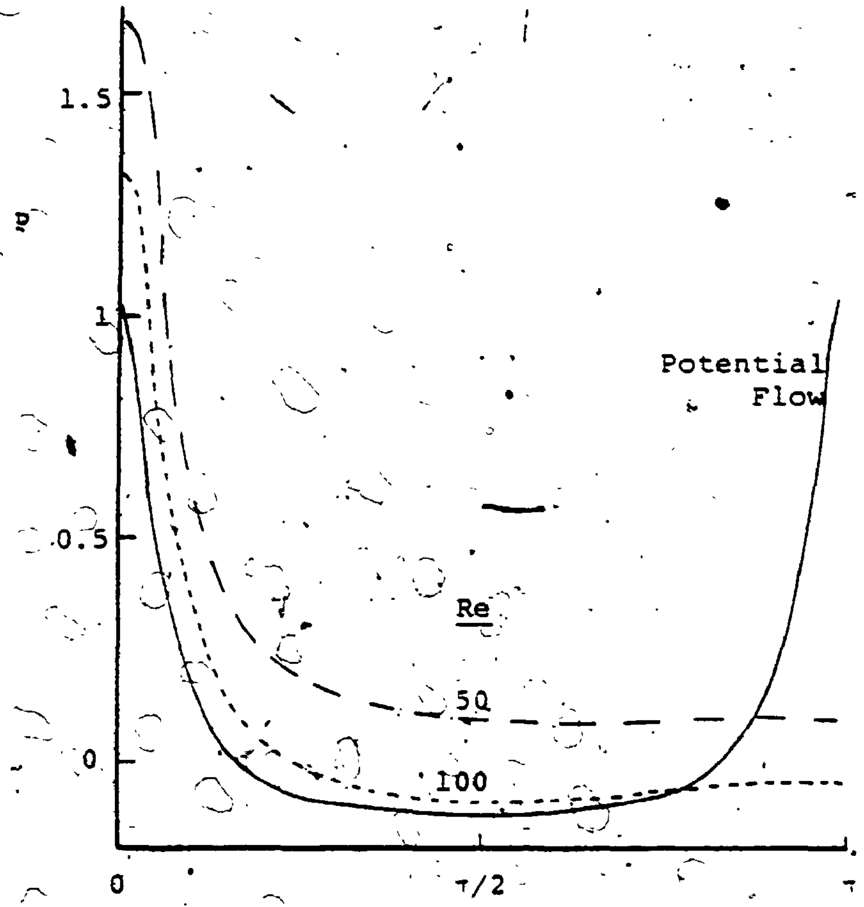

Figure A.IV.9 Surface Pressure Distribution at High Reynolds Numbers for a Prolate Spheroid with Aspect Ratio = 0.2

sphere is quite good for very small Reynolds numbers as long as $\mu_{ex}/\mu_i \ll 1$. (μ_{ex}/μ_i for water in air is 0.018).

For higher Reynolds numbers, a theoretical and experimental study of the internal circulation in water drops falling at terminal velocity was carried out by Le Clair et. al. [53]. The result of their study shows that there is no difference between the drag on a water drop and that of a rigid particle of the same Reynolds number, up to 300, as long as the particle is assumed to have the same shape. Their results were confirmed by the wind tunnel measurements of Beard and Pruppacher [83] on water drops falling at terminal velocity in air. In the present study, as the drop size is small, the Reynolds number is expected to be in the low or intermediate range and hence the effect of the internal circulation is neglected.

REFERENCES

[1] Lord Rayleigh, "On the Equilibrium of Liquid Conducting Masses Charged with Electricity", Philosophical Magazine, Vol. 14, pp. 184-186, 1882.

[2] C.D. Hendricks, "Charged Droplet Experiments", J. of Colloid Sci., Vol. 17, pp. 249-259, 1962.

[3] J.W. Schweizer and D.N. Hanson, "Stability Limit of Charged Drops", J. of Colloid and Interface Sci., Vol. 35, pp. 417-423, 1971.

[4] C.D. Hendricks and J.M. Schneider, " Stability of a Conducting Droplet under the Influence of Surface Tension and Electrostatic Forces", Am. J. Phys., Vol. 31, pp. 450-453, 1963.

[5] M.A. Abbas and J. Latham, "The Instability of Evaporating Charged Drops", J. of Fluid Mech., Vol. 30, pp. 663-670, 1967.

[6] A. Doyle, D.R. Moffett and B. Vonnegut, "Behaviour of Evaporating Electrically Charged Droplets", J. of Colloid Sci., Vol 19, pp. 136-143, 1964.

[7] J.J. Thomson, Cambridge, pp. 179, 1906. (Referred to in Ref. 8)

[8] J.A. Robertson, "Interactions Between a Highly Charged Aerosol Droplet and the Surrounding Gases", Ph.D. Thesis, University of Illinois, 1969.

[9] G.S.P. Castle, "Recent Advances in the Electrical Charging of Fine Particles", Proceedings of the 16th. Annual Meeting of the Fine Particle Society, 22-3, 1985.

[10] M.M. Pauthenier and M.M. Moreau- Hanot, " Charging of Spherical Particles in an Ionizing Field", J. de Physique et le Radium, Vol. 7, pp. 590-613, 1932.

[11] C.D. Hendricks, " Charging Macroscopic Particles", in <u>Electrostatics and Its Applications</u>, A.D. Moore, Ed. New York: Wiley, Ch. 4, 1973.

[12] G. Taylor, " Disintegration of Water Drops in an Electric Field", Proc. Roy. Soc. London A, Vol. 280, pp. 383-397, 1964.

[13] M.A. Abbas, A.K. Azad and J. Latham, "The Disintegration and Electrification of Liquid Drops Subjected to Electrical Forces", Proc. of the Second Conference on Static Electrification, pp. 69-77, 1967.

[14] S.B. Sample, B. Raghupathy and C.D. Hendricks, "Quiescent Distortion and Resonant Oscillations of a Liquid Drop in an Electric Field", Int. J. Eng. Sci., Vol. 8, pp. 97-109, 1970.

[15] S.B. Sample, C.D. Hendricks, "Potential Energy of a Deformed Conducting Sphere in an Electric Field", Int. J. Eng. Sci., Vol. 7, pp 427-435, 1969.

[16] S.A. Ryce and R.R. Wyman, "Asymmetry in the Electrostatic Dispersion of Liquids", Can. J. of Physics, Vol. 42, pp. 2185-2194, 1964.

[17] S.A. Ryce and D.A. Patriarche, "Energy Consideration in the Electrostatic Dispersion of Liquids", Can. J. of Physics, Vol. 43, pp. 2192-2199, 1965.

[18] R.J. Pfeifer and C.D. Hendricks, "Charge to Mass Relationship for Electrohydrodynamically Sprayed Liquid Droplets", Phys. of Fluids, Vol. 10, No. 10, pp. 2149-2154, 1967.

[19] D.G. Roth and A.J. Kelly, "Analysis of the Disruption of Evaporating Charged Droplets", IEEE Trans. IAS, Vol. IA-19, pp. 771-775, 1983.

[20] A.J. Kelly, Private Communication, January 1984.

[21] A. Russell, *A Treatise on the Theory of Alternating Currents*, Cambridge Univ. Press, Vol. 1, 2nd Ed., 1914.

[22] W.R. Smythe, *Static and Dynamic Electricity*, McGraw Hill, 1950.

[23] R.D. Cook, *Concepts and Applications of Finite Element Analysis*, John Wiley and Sons Inc., 1974.

[24] B. Vonnegut and R.L. Neubauer, "Production of Monodisperse Aerosol Particles by Electrical Atomization", J. Colloid Sci., Vol. 7, pp. 515-522, 1952.

[25] J. Thewlis, *Encyclopaedic Dictionary of Physics*, Vol. 2, The Macmillan Company, New York, 1962.

[26] H.B. Callen, Thermodynamics, John Wiley and Sons, 1962.

[27] A.J. Kelly, "The Electrostatic Atomization of Hydrocarbons", Proc. of the Second International Conf. of Liquid Atomization and Spray Systems, pp. 57-65, 1982.

[28] A.J. Kelly, "Coulomb Crystallization in Charged Droplet Sprays", IEEE-IAS Conf. Record, 1985 Annual Meeting, pp. 1343-1345, 1985.

[29] O. Berg and D.C. George, "Investigations of Charged Water Drops", Monthly Weather Review, Vol. 95, No. 12, pp. 884-894, 1967.

[30] W.N. English, "Corona from a Water Drop", Physical Review, Vol. 74, No. 2, pp. 179-189, 1948.

[31] A.M. Neville and J.B. Kennedy, Basic Statistical Methods for Engineers and Scientists, International Text Book Company, 1964.

[32] J. Zeleny, "The Electrical Discharge from Liquid Points and a Hydrostatic Method of Measuring the Electric Intensity at Their Surfaces", Physical Review, Vol. 3, pp. 69-78, 1914.

[33] D.P.H. Smith, "The Electrohydrodynamic Atomisation of Liquids", IEEE-IAS Conf. Proceedings, pp. 1080-1088, 1984.

[34] J.B. Matthews, "Mass Loss and Distortion of Freely Falling Water Drops in an Electric Field", J. of Geophysical Research, Vol. 72, No. 12, pp 3007-3013, 1967.

[35] J.E. McDonald, "The Shape and Aerodynamics of Large Raindrops", J. of Meteorology, Vol. 11, pp 478-494, 1954.

[36] H.R. Pruppacher, R. Rasmussen, C. Walcek and P. Wang, "A Wind Tunnel Investigation of the Shape of Uncharged Raindrops in the Presence of an External, Vertical Electric Field", Proceedings of the Second International Collequium on Drops and Bubbles, NASA, pp 239-243, 1982.

[37] M.J. Miksis, "Shape of a Drop in an Electric Field", Phys. Fluids, Vol. 24, pp 1967-1972, 1981.

[38] H.R. Pruppacher and K.V. Beard, "A Wind Tunnel Investigation of the Internal Circulation and Shape of Water Drops Falling at Terminal Velocity in Air", Quart. J.R. Met. Soc., Vol. 96, pp 247-256, 1970.

[39] K.V. Beard, "Terminal Velocity and Shape of Cloud and Precipitation Drops Aloft", J. of the Atmos. Science, Vol. 33, pp 851-864, 1976.

[40] H.R. Pruppacher and R.L. Pitter, "A Semi-Emperical Determination of the Shape of Cloud and Rain Drops", J. of the Atmos. Science, Vol. 28, pp 86-94, 1971.

[41] N.K. Adam, <u>The Physics and Chemistry of Surfaces</u>, London, Oxford Press, pp 436, 1949.

[42] G. Ailam and I. Gallily, "Stability of Electrically Charged Droplets", The Physics of Fluids, Vol. 5, pp 575-582, 1962.

[43] J. Zeleny, "On the Condition of Instability of Electrified Drops with Applications to the Electrical Discharge from Liquid Points", Proc. Cambridge Phil. Soc., Vol. 18, pp 71-83, 1915.

[44] J. Zeleny, "The Instability of Electrified Liquid Surfaces", Phys. Rev., Vol. 10, pp 1-6, 1917.

[45] W.A. Macky, "Some Investigations on the Deformation and Breaking of Water Drops in Strong Electric Field", Proc. Roy. Soc. London A, Vol. 133, pp 565-587, 1931.

[46] C.G. Garton and Z. Krasucki, "Bubbles in Insulating Liquids Stability in an Electric Field", Proc. Roy. Soc. London, A, Vol. 280, pp 211-226, 1964.

[47] E. Giffen and A. Muraszew, <u>The Atomization of Liquid Fuels</u>, Chapman and Hall Ltd., London, 1953.

[48] J.O. Hinze, "Fundamentals of the Hydrodynamic Mechanics of Splitting in Dispersion Processes", A.I.Ch.E. Journal, Vol. 1, pp 289-295, 1955.

[49] H. Lamb, <u>Hydrodynamics</u>, 6th edition, New York, Dover Publ. 1932.

[50] J.D. Klett, "On the Breakup of Water Drops in Air", J. of Atmos. Sci., Vol. 28, pp 646-647, 1971.

[51] C.S. Yih, Dynamics of Nonhomogeneous Fluids, New York, Macmillan, 1965.

[52] J.R. Grace, T. Wairegi and J. Brophy, "Breakup of Drops and Bubbles in Stagnant Media", Can. J. of Chem. Eng., Vol. 56, pp 3-8, 1978.

[53] B.P. Le Clair, A.E. Hamielec, H.R. Bruppacher and W.D. Hall, "A Theoretical and Experimental Study on the Internal Circulation in Water Drops Falling at Terminal Velocity in Air", J. Atmos. Sci., Vol. 29, pp 728-740, 1972.

[54] G. Thomas and R. Finney, Calculus and Analytical Geometry, Addison and Wesley Publishing Company, 5th ed., 1979.

[55] J. Jeans, The Mathematical Theory of Electricity and Magnetism, Cambridge University Press, London, 5th edition, 1933.

[56] L.D. Landau and E.M. Lifshitz, Electrodynamics of Continuous Media, Pergamon Press, 2nd edition, 1984.

[57] J. Happel and H. Brenner, Low Reynolds Number Hydrodynamics, Englewood Cliffs, N.J., Prentics Hall Inc., 1965.

[58] T. Aoi, "The Steady Flow of Viscous Fluid Past a Fixed Spheroidal Obstacle at Small Reynolds Number", J. Phys. Soc. of Japan, Vol. 10, pp 119-141, 1955.

[59] I. Proudman and J.R. Pearson, "Expansions at Small Reynolds Numbers for the Flow Past a Sphere and a Circular Cylinder", J. Fluid Mech., Vol. 2, pp 237-262, 1957.

[60] J. Masliyah and N. Epstein, "Numerical Study of Steady Flow Past Spheroids", J. Fluid Mech., Vol. 44, pp 493-512, 1970.

[61] J. Masliyah, "Symmetric Flow Past Orthotropic Bodies", Ph.D. Thesis, University of British Columbia, Canada, 1970.

[62] A.G. Bailey and W. Balachandran, "The Disruption of Electrically Charged Jets of Viscous Liquid", J. of Electrostatics, Vol. 10, pp 99-105, 1981.

[63] G.A. Dawson, "Pressure Dependence of Water-Drop Corona Onset and Its Atmospheric Importance", J. of Geophys. Research, Vol. 74, No. 28, pp. 6859-6868, 1969.

[64] G.A. Dawson, "Electrical Corona from Water-Drop Surfaces", J. of Geophysical Research, Vol. 75, No. 12, pp. 2153-2158, 1970.

[65] R.F. Griffiths and J. Latham, "The Emission of Corona from Falling Drops", J. of the Meteorological Society of Japan, Vol. 50, pp. 416-422, 1972.

[66] E.W. Muller, "Field Desorption", Phys. Rev. Vol. 102, pp. 618-624, 1956.

[67] A.J. Kelly, "Electrostatic Metallic Spray Theory", J. of Applied Physics, Vol. 47, pp. 5264-5271, 1976.

[68] J.V. Iribarne and B.A. Thomson, "On the Evaporation of Small Ions from Charged Droplets", J. Chem. Phys., Vol. 64, pp. 2287-2294, 1976.

[69] G. Hartmann, "Theoretical Evaluation of Peek's Low", IEEE-IAS Conf. Proceedings, pp. 1113-1117, 1980.

[70] G. Berger, "Theoretical Inception Time of the First Corona in Atmospheric Air", IEEE-IAS Conf. Proceedings, pp. 1108-1112, 1980.

[71] C.F. Gallo, "The Effect of Humidity and Temperature Variations on the Behaviour of Wire to Plane Coronas", Appl. Opt., Suppl. 3, pp. 111-119, 1969.

[72] E. Kuffel, "Electron Attachment Coefficients in Oxygen, Dry Air and Water Vapour", Proc. Phys. Soc., Vol. 74, pp. 297-308, 1959.

[73] M. Khalifa and S. Debieky, "Analysis of the Effect of Humidity on DC Corona Power loss", IEE Proc., Vol. 118, pp. 714-718, 1971.

[74] E.C. Salthouse, "Effect of Humidity on Positive Glow Corona Characteristics", IEE Gas Discharge Conf., Publ. No. 143, pp. 224-226, 1976.

[75] M. Khalifa, "Discussion Contribution", IEEE Trans. Vol. PAS-86, pp. 1144, 1967.

[76] M. Abdel-Salam, "Positive Wire-To-Plane Coronas as Influenced by Atmospheric Humidity", IEEE-IAS Conf. Proc., pp. 1098-1104, 1983.

[77] L.B. Loeb, Electrical Coronas, Univ. of California Press, L.A., 1965.

[78] C.W. Oseen, Arch. Mth. Phys., Vol. 24, pp 108-114, 1915 (referred to in Ref 53)

[79] D.R. Breach, "Slow Flow Past Ellipsoids of Revolution", J. Fluid Mech., Vol. 10, pp 306-314, 1951.

[80] R.G. Folsam and A. Arber, Am. Soc. Mech. Eng., Vol. 78, 1956 (referred to in Ref 53)

[81] W.N. Bond, "Bubbles and Drops and Stokes Law", Phil. Mag., Ser. 7, Vol. 4, pp 889-898, 1927.

[82] W. Rybezynski, Bull Acad. Caracovic, Ser. A., pp 40, 1911 (referred to in Ref. 31)

[83] K. Beard and H. Pruppacher, "A Determination of the Terminal Velocity and Drag of Small Water Drops by Means of a Wind Tunnel", J. Atm. Sci., Vol. 26, pp 1066-1072, 1969.